



**Politecnico  
di Torino**

**Department of Environment, Land and Infrastructure Engineering  
Collegio di Ingegneria per l'Ambiente e il Territorio**

**Master of Science in Mining Engineering**

**Master's degree Thesis**

*Performance analysis of a dimension stone exploitation  
with chain saw cutting machines:  
the "Penna dei Corvi" quarry case study*

**Supervisor**

Prof. Ing. Marilena Cardu

**Candidate**

Alfio Di Giovanni

**Co-supervisors**

Ing. Carmine Todaro

Ing. Stefano Bianchini

Geol. Brunello Forfori

15 October 2021



## Abstract

Dimension stone exploitation is one of the most important activities in the field of raw materials in Italy. In particular, the Tuscany region is famous worldwide for its marble.

This study arises from the need of investigating the behaviour of a chain saw cutting machine used to cut the marble at the “*Penna dei Corvi*” quarry in the municipality of Vagli Sotto (LU), where the quarrymen met severe advancement problems of the machine due to the interaction of the chain saw machine's tools with the rock.

A series of laboratory analyses were then performed to investigate and understand the excavated material's behaviour, characteristics, and properties to solve the problem of zero productivity found on that site. The analysis was drawn up through the study of thin sections via a petrographic analysis, the evaluation of local microhardness, the determination of the abrasiveness of the excavated material through the CERCHAR abrasivity test, and with a test campaign for the study of the metal wear in conditioned material. Moreover, chemical analyses were carried out in order to understand the structure and the composition of the chain saw's tools employed for the cutting operations.



## Ringraziamenti

Vorrei dedicare, a conclusione di questo lavoro di tesi, qualche riga a tutti coloro che ho avuto modo di conoscere e che mi sono stati vicini in questo importante percorso di crescita personale e professionale.

Desidero esprimere la mia gratitudine nei confronti della prof.ssa Ing. Marilena Cardu, relatrice di questa tesi, per l'immensa disponibilità e cortesia dimostratemi, per tutto l'assistenza fornita durante la stesura e per gli indispensabili consigli ed insegnamenti.

Ci tengo particolarmente a ringraziare l'Ing. Carmine Todaro, per il supporto offertomi nella realizzazione delle attività in laboratorio, per i preziosi suggerimenti ricevuti e per la sua grande disponibilità.

Un sentito grazie va anche all'Ing. Stefano Bianchini e al Geol. Brunello Forfori per la loro affabilità e cortesia, per l'aiuto e il materiale fornitomi per la realizzazione di questo lavoro.

Ringrazio l'Ing. Simone Saltarin ed l'Ing. Andrea Carigi per il loro indispensabile appoggio ricevuto durante le realizzazioni delle prove di laboratorio.

Vorrei ringraziare i Prof. Sara Ferraris e Graziano Ubertalli per l'infinita gentilezza e per la realizzazione delle analisi microscopiche sugli utensili. Grazie anche ai Prof. Paola Marini e Claudio De Regibus per il loro tempo dedicatomi.

Grazie anche alla *Luana Marmi S.r.l.* nella figura di Emilio Buonasera e dei cavatori Marchino, Marco, Mattia ed Ezio, per avermi dato la possibilità di prendere parte ai lavori in cava.

Voglio ringraziare la mia famiglia, in particolare i miei genitori, per il loro aiuto, sostegno morale ed economico, e per l'affetto che non mi hanno fatto mai mancare durante tutti questi anni.

Ed infine, il mio ringraziamento va alla mia Alessia. Grazie per tutto l'aiuto. Grazie per tutto il sostegno. Grazie per il supporto. Grazie che mi sopporti ogni giorno, non deve essere facile... Grazie per essere sempre orgoglioso di me. Grazie.

Grazie di cuore a tutti



# Contents

Abstract	1
Figures Index	7
Tables Index	9
Graphs Index	9
Introduction	13
1. Geological setting	15
1.1. Deposits characteristics	16
1.2. Hydrographic and hydrogeological characteristics	19
1.3. Structural survey	19
1.4. Structural characteristics of the site	20
1.5. Exploitation plan	22
2. Chain saw cutting machine	23
2.1. Cutting theory	30
2.1.1. Ultra-simplified model of the action of a drag tool	30
2.1.1.1. Cutting force	31
2.1.1.2. Contact force	32
2.1.2. Nishimatsu model	33
2.1.3. Comments on the examined models	35
3. PCD SEM-EDS analysis	37
3.1. Results	38
4. Laboratory analysis	44
4.1. Petrographic analysis	44
4.2. Vickers microhardness test	48
4.2.1. Results	51
4.3. CERCHAR abrasivity test	70

4.3.1. Results	72
4.4. DRX analysis	83
4.4.1. Results	84
4.5. Wear test	86
4.5.1. Conditioning with water	90
4.5.2. Conditioning with chemical agents	93
5. Conclusion	96
Bibliography	98



## Figures Index

Figure 1.1 - Geographical location of the "Penna dei Corvi" quarry (Mapcarta)	15
Figure 1.2 - Aerial photography of the quarry by drone	15
Figure 1.3 - Open pit quarry, Cipollino marble	16
Figure 1.4 - Underground exploitation entrance for the extraction of the grey-white marble	17
Figure 1.5 - Grey-white marble with flint nodules	18
Figure 1.6 - Particular wear of a toolholder after cutting the grey-white marble core	18
Figure 1.7 - Stereonet representation	20
Figure 1.8 - Geological Strength Index for jointed rocks (Hoek and Marinos, 2000)	21
Figure 2.1 - CSM-962 chain saw machine, front view	24
Figure 2.2 - CSM-962 chain saw machine, back view	24
Figure 2.3 - Preparatory work of the chain saw cutting machine	26
Figure 2.4 - Fantini chain saw machine	26
Figure 2.5 - Cutting blade	28
Figure 2.6 - Serie of toolholders and PCD	29
Figure 2.7 - Zoom of the toolholder (left), cutting chain front view (right)	29
Figure 2.8 - PCD tools. The first tool is new, the others are damaged and unusable	29
Figure 2.9 - Cutting cycle (Mancini and Cardu, 2001)	31
Figure 2.10 - Cutting force diagram	32
Figure 2.11 - Contact force diagram	33
Figure 2.12 - Nishimatsu model: forces and stress scheme (Nishimatsu, 1972)	33
Figure 3.1 - Sample 1, new tool	38
Figure 3.2 - SEM analysis: new sample, area 1	38
Figure 3.3 - SEM analysis: new sample, area 2	38
Figure 3.4 - Sample 2, chipped PCD tool	40
Figure 3.5 - SEM analysis: chipped sample	40
Figure 3.6 - Zoom on the chipped zone	40
Figure 3.7 - EDS analysis: chipped sample	41
Figure 3.8 - Sample 3, completely worn PCD tool	42
Figure 3.9 - SEM analysis: detached sample, area 1	42
Figure 3.10 - SEM analysis: detached sample, area 2	42
Figure 3.11 - EDS analysis: completely worn sample	43

Figure 4.1 - Thin section S.S._01	44
Figure 4.2 - Thin section S.S._02	45
Figure 4.3 - Thin section S.S._03	46
Figure 4.4 - Thin section S.S._04	47
Figure 4.5 - Leitz Wetzlar Durimet	49
Figure 4.6 - Schematic of indentation (Smallman & Ngan, 2014)	49
Figure 4.7 - Specimen 1	53
Figure 4.8 - Specimen 2	55
Figure 4.9 - Specimen 3	57
Figure 4.10 - Specimen 4	59
Figure 4.11 - Specimen L_01	61
Figure 4.12 - Specimen L_02	63
Figure 4.13 - Specimen L_03	65
Figure 4.14 - Specimen L_04	67
Figure 4.15 - Testing device setup according to West apparatus (Rostami et al., 2013)	71
Figure 4.16 - Flat wear measuring (Rostami et al., 2005)	72
Figure 4.17 - Specimen A before and after the scratches	74
Figure 4.18 - Specimen B before and after the scratches	79
Figure 4.19 - XRD - Rigaku SmartLab SE	83
Figure 4.20 - Test 1 spectral data	84
Figure 4.21 - Test 2 spectral data	85
Figure 4.22 - Cake graph expressing the results obtained by the test	85
Figure 4.23 - Scheme of the test (Oñate Salazar et al., 2018)	86
Figure 4.24 - Cross section and pictures of the test device (Oñate Salazar et al., 2018)	87
Figure 4.25 - Representative sample of the material	88
Figure 4.26 - Granulometric curve of the crushed marble	89
Figure 4.27 – Weight lost – Water content graph: wear bell curve	91
Figure 4.28 - Weight lost – Water content graph: wear bell curve and conditioned test	94
Figure 4.29 - Weight lost – Water content graph: Conditioning test	95

## Tables Index

Table 1.1 - Representative plan of the systems in "Penna dei Corvi" quarry (Forfori, 2020)	19
Table 1.2 - RMR classification (Forfori, 2020)	21
Table 2.1 - Technical data of the CSM-962	25
Table 2.2 - Technical data of the Fantini GU 70-R-XC	27
Table 3.1 - EDS analysis results: new sample, area 1	39
Table 3.2 - EDS analysis results: new sample, area 2	39
Table 3.3 - EDS analysis results: chipped sample	41
Table 4.1 - Microhardness measurements specimen 1	52
Table 4.2 - Microhardness measurements specimen 2	54
Table 4.3 - Microhardness measurements specimen 3	56
Table 4.4 - Microhardness measurements specimen 4	58
Table 4.5 - Microhardness measurements specimen L_01	60
Table 4.6 - Microhardness measurements specimen L_02	62
Table 4.7 - Microhardness measurements specimen L_03	64
Table 4.8 - Microhardness measurements specimen L_04	66
Table 4.9 - Specimen A, $CAI_{(64.5)} [0^\circ]$	73
Table 4.10 - Specimen A, $CAI_{(64.5)} [90^\circ]$	73
Table 4.11 - $CAI_{(64.5)}$ average Specimen A	71
Table 4.12 - $CAI_{(55)}$ Specimen A	73
Table 4.13 - $CAI_{(64.5)}$ average Specimen A	72
Table 4.14 - $CAI_{(55)}$ average Specimen A	74
Table 4.15 - $CAI_{(55)}$ classification	74
Table 4.16 - Specimen A, Test 1	75
Table 4.17 - Specimen A, Test 2	75
Table 4.18 - Specimen A, Test 3	75
Table 4.19 - Specimen A, Test 4	75
Table 4.20 - Specimen A, Test 5	76
Table 4.21 - Specimen A, Test 6	76
Table 4.22 - Specimen A, Test 7	76
Table 4.23 - Specimen A, Test 8	76
Table 4.24 - Specimen A, Test 9	77

Table 4.25 - Specimen A, Test 10	77
Table 4.26 - Specimen B, CAI <sub>(64.5)</sub> [0°]	78
Table 4.27 - Specimen B, CAI <sub>(64.5)</sub> [90°]	78
Table 4.28 - CAI <sub>(64.5)</sub> average Specimen B	76
Table 4.29 - CAI <sub>(55)</sub> Specimen B	78
Table 4.30 - CAI <sub>(64.5)</sub> average Specimen B	77
Table 4.31 - CAI <sub>(55)</sub> average Specimen B	79
Table 4.32 - CAI <sub>(55)</sub> classification	79
Table 4.33 - Specimen B, Test 1	80
Table 4.34 - Specimen B, Test 2	80
Table 4.35 - Specimen B, Test 3	80
Table 4.36 - Specimen B, Test 4	80
Table 4.37 - Specimen B, Test 5	81
Table 4.38 - Specimen B, Test 6	81
Table 4.39 - Specimen B, Test 7	81
Table 4.40 - Specimen B, Test 8	81
Table 4.41 - Specimen B, Test 9	82
Table 4.42 - Specimen B, Test 10	82
Table 4.43 - Grain size distribution of the sample analyzed	89
Table 4.44 - Test with 1% of water content in weight	90
Table 4.45 - Test with 2% of water content in weight	90
Table 4.46 - Test with 3% of water content in weight	91
Table 4.47 - Test with 5% of water content in weight	91
Table 4.48 - Test with 7% of water content in weight	91
Table 4.49 - Test with 9% of water content in weight	91
Table 4.50 – Product A, test with 4% of solution content in weight	93
Table 4.51 - Product B, test with 4% of solution content in weight	93
Table 4.52 - Product B, test with 9% of solution content in weight	94

## Graphs Index

Graph 4.1 - Distribution of the hardness values specimen 1	53
Graph 4.2 - Distribution of the hardness values specimen 2	55
Graph 4.3 - Distribution of the hardness values specimen 3	57
Graph 4.4 - Distribution of the hardness values specimen 4	59
Graph 4.5 - Distribution of the hardness values specimen L_01	61
Graph 4.6 - Distribution of the hardness values specimen L_02	63
Graph 4.7 - Distribution of the hardness values specimen L_03	65
Graph 4.8 - Distribution of the hardness values specimen L_04	67



## Introduction

The world of dimension stones, particularly the marble market, is expected to grow, reaching a production value of 64 billion \$ in 2023. Italy, and especially the Apuo District, is firmly in the top ten of quality marble-producing countries (Mordor Intelligence, 2021).

This thesis aims to investigate the performance of a chain saw cutting machine used to exploit the marble at the “Penna dei Corvi” quarry, located in the municipality of Vagli Sotto (LU), in the Tuscany region, where severe problems of machine advancement occur due to the problematic rock-tools interaction. For this reason, a series of laboratory tests to characterize and study the physical and mechanical characteristics of the marble have been carried out.

The tests were conducted on two different types of marble. A study was carried out on the green-red Cipollino marble extracted in an open-pit quarry and, in parallel to this, the same analysis was performed on a white-grey marble, abundant in quartz, coming from the underground excavation. Due to difficulties in cutting, encountered a few meters after opening the entrance to the underground, the excavation is at present stopped. For this reason, it became necessary to investigate and perform analyses both on the material and the chain saw’s tools, in order to characterize them and overcome the problem.

This work is divided into 5 chapters: in the first chapter, a description of the extraction site's and operational processes are provided. Then, the marble deposit was examined in terms of hydrographic and hydrogeological characteristics. The structural analysis of the site has been proposed according to Bieniawski’s (1989) method, and a brief description of the exploitation plan is presented.

In chapter 2, the two chain saw cutting machines, one for the open-pit exploitation and the other for underground excavation, were described in detail, and a presentation of the cutting theory is proposed.

Special attention is devoted to the chain of the machines, since the tools installed are made of polycrystalline diamond. For these specific tools, in chapter 3, a in-depth analysis was performed thanks to the Scanning Electron Microscopy (SEM) - Energy Dispersive X-ray Spectrometry (EDS).

Chapter 4 shows and discusses the different laboratory tests realized to classify the marble. They firstly consist in the petrographic analyses of the thin sections of the two marbles; moreover, a

study related to the microhardness of the marbles is proposed, to compare the results achieved with the microhardness of the tools. The CERCHAR abrasivity test, valid for the characterization of the marble in terms of rock abrasivity, was performed in both marbles. An additional survey with the X-ray diffractometer was carried out for the white-grey marble. This analysis is able to evaluate the different compositions of the marble and, in particular, to estimate the percentages of calcite, quartz, and other minerals present as impurities. A study campaign on the wear test completes the material characterization analysis. These tests were aimed to reproduce the interaction between the tools and the material to be excavated, varying the water content or conditioning the material by adding two different chemical additives able to reduce the wear of the tools.

Finally, Chapter 5 presents the conclusions which summarize the main results obtained.



## 1. Geological setting

The marble quarry "Penna dei Corvi" is located in Tuscany, in the basin of Fontana Baisa, in the municipality of Vagli Sotto (LU); Figure 1.1 shows the geographical location of the quarry. The mining quarry area develops, throughout the project, between the altitudes of 920 and 800 m a.s.l.

The site of interest, the Fontana Baisa basin, is in the middle eastern sector of the Apuan chain, to the east of the ridges that connect Monte Fiocca to Monte Sumbra. Towards the north there are instead the Monte Fiocca, Monte Croce, and Colle Pelliccia. The quarry has an overall development along the N-S axis, widening towards the west in the northern part (Forfori, 2020).

Figure 1.2 shows an aerial photography of the quarry by drone.

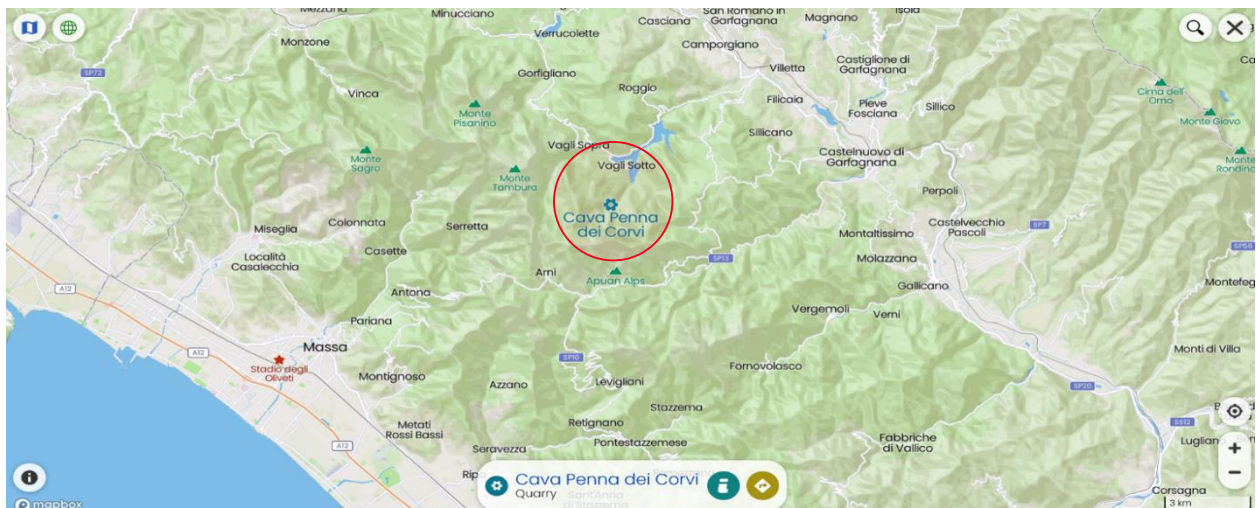


Figure 1.1 - Geographical location of the "Penna dei Corvi" quarry (Mapcarta)

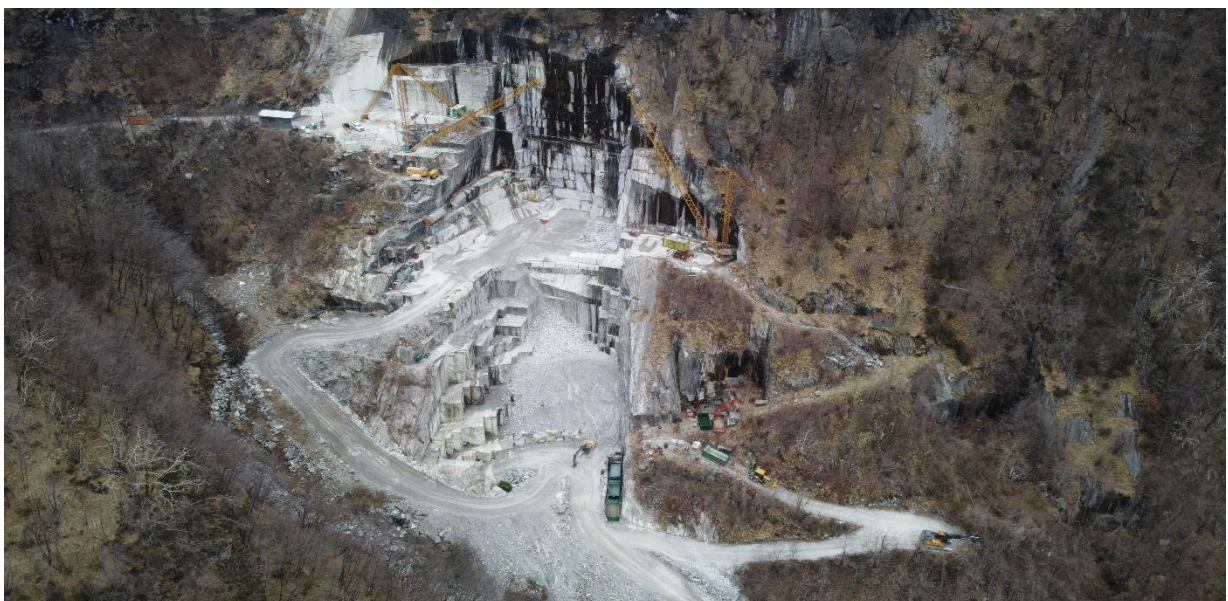


Figure 1.2 - Aerial photography of the quarry by drone

## 1.1. Deposits characteristics

In the basin, the material of most significant interest is represented by the group of "Cipollini", Figure 1.3; in the southern portion of the quarry, the grey-white marbles emerge, Figure 1.4.

"Cipollini di Vagli", in the sense of the term as an ornamental stone and not in the geological meaning, represents a green and red-purple calcareous and chalky phyllite known by the name of Verde and Rosso Luana. The Cipollino field that extends over the basin is characterized by a more significant presence of green levels in the left orographic area of the Fosso di Biteto. In contrast, in the left orographic area of the Fosso Maccava, the resource appears with alternation of both green and red levels. Characteristic of the material is the presence of a dense alternation, intensely folded of phyllite and calcareous schist levels, crossed by veins of quartz. This pattern gives rise to at least five different sub-varieties within the Cipollini (CGT, 2007).

Generally, the material is compact, with limited noticeable fracturing, generally dipping towards SE and inclined between 40° and 60°. These fine-grained clastic sediment levels often interest it and emerge following the exploitation (Forfori, 2020).



*Figure 1.3 - Open pit quarry, Cipollino marble*



*Figure 1.4 - Underground exploitation entrance for the extraction of the grey-white marble*

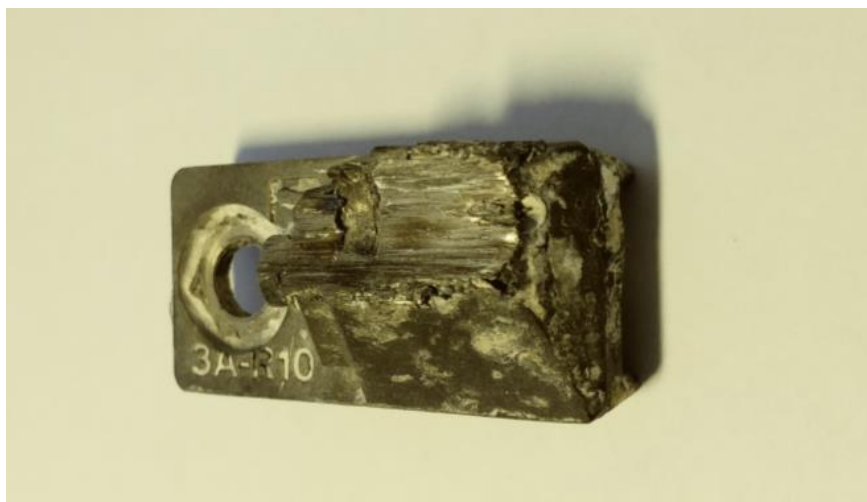
In the upper part of the quarry, at 869 m a.s.l., in the area where the gallery's construction was planned, there is the presence of grey-white and ivory marble with flint nodules, Figure 1.5.

In this area, with the first works to start the underground exploitation in 2018, a "sheath fold" with a flinty marble core in entrochi, with a trend of about 350°, immersion at NW of about 10°, characterized by boudinage, emerged. This structure, initially, seemed to close quickly, while in a short space, 3 advances in the tunnel for a total of about 9 m, the core opened into a boudinage, and the structure progressed towards to the interior of the cluster (Forfori, 2020).



*Figure 1.5 - Grey-white marble with flint nodules*

The core of this structure proved impossible to be cut, given the rapid wear of both the drilling and cutting tools, consuming the polycrystalline diamond (PCD) tools and the toolholders. In Figure 1.6 is proposed a photo of the toolholder after cutting the grey-white marble nucleus; as it is possible to notice, the PCD tool is detached from its position and the toolholder is damaged and useless.



*Figure 1.6 - Particular wear of a toolholder after cutting the grey-white marble core*

## 1.2. Hydrographic and hydrogeological characteristics

The quarry is on the orographic left of the Fosso Maccava, to which the Fosso di Biteto joins a little further downstream. The stream retains the name of Fosso Maccava and flows into the artificial lake of Vagli Sotto; it has a seasonal nature: it is activated in correspondence with meteoric events or due to snow melting. The watercourse Fosso di Biteto, instead, has a perennial character. These watercourses flow in a talweg with narrow and engraved valleys, characterized by vertical walls, signifying a pluvial-fluvial morphology. From the hydrogeological point of view, the area reflects the permeability and the structure of the formations (Schede Rete Natura 2000, 2017).

## 1.3. Structural survey

The quarry has a good structural condition; the geomechanical survey was essentially carried out on the area currently being excavated. The ranges and average plans relating to the central discontinuity systems that characterize the site are given in Table 1.1.

Table 1.1 - Representative plan of the systems in "Penna dei Corvi" quarry (Forfori, 2020)

System	K'1	K'2	K'3
Ranges Dip	27 – 66	25 – 55	63 – 90 71-90
Ranges Dip direction	116 – 160	45 – 84	32-58 196 - 221
Representative Plane	138 – 48	64 – 48	210 – 82

Description of the main systems of the site:

- K'1: represents the most crucial system from the geomechanical point of view. It is characterized by roughness values (JRC) in the range 4-6, 6-8, and 8-10; spacing ascribable to class 2-6m and > 6m; the discontinuities are of the persistent type.
- K'2: it is characterized by JRC values included in the range 4-6, 6-8, and 10-12; spacing ascribable to class 2-6m and > 6m; persistent type fractures.
- K'3: they have spacings in the range of classes 2-6m and > 6m, JRC values included in the range 6-8. the type of discontinuity is 50% sub-persistent and 50% persistent.

A stereonet representation of the joints is shown in Figure 1.7.

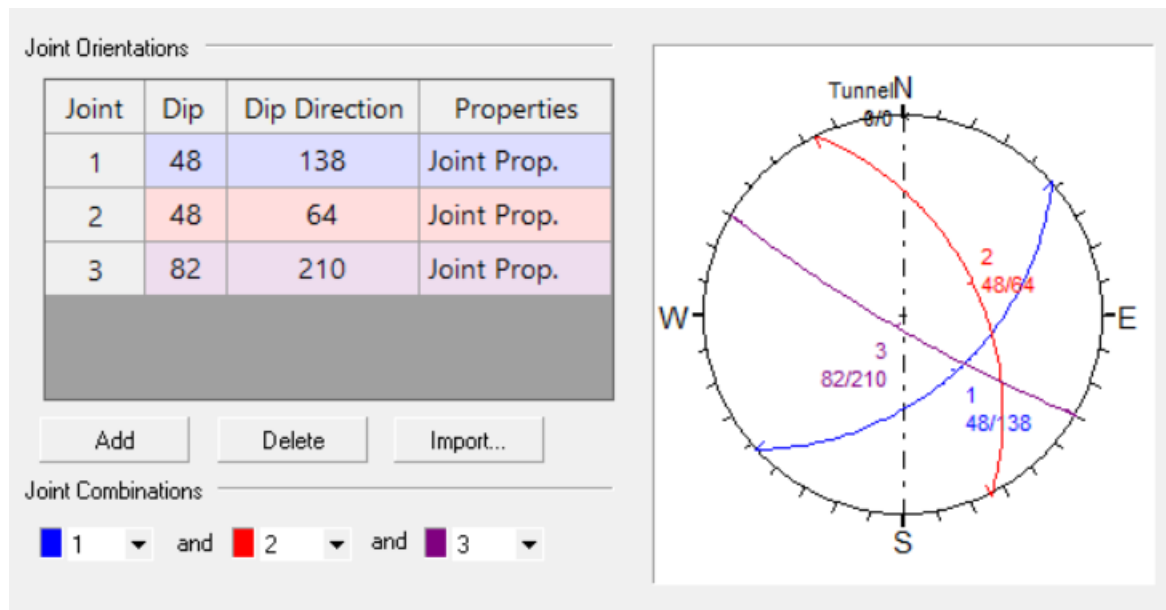


Figure 1.7 - Stereonet representation

#### 1.4. Structural characteristics of the site

The production area is characterized by a limited number of discontinuities with an average spacing above 1 m, a condition that allows the site to be exploited to produce blocks of ornamental stone.

According to Bieniawski (1989) and to the Geological Strength Index (GSI) belonging to Hoek & Brown (1997), a geomechanical classification of the site was carried out.

To determine RQD lack of experimental data relating to coring, the correlation that uses the number of joints,  $J_V$ , with the expression modified by Palmström (1995) has been employed:

$$RQD [\%] = 110 - 2.5 * J_V$$

$$J_V = \frac{1}{S_1} + \frac{1}{S_2} + \dots + \frac{1}{S_n}$$

Where  $S_1$ ,  $S_2$  and  $S_n$  are the average spacings for the joint set (Palmström, 1974).

The Rock Mass Rating (RMR) was calculated according to the classification system proposed by Bieniawski (1989). Table 1.2 presents the index achieved.

Table 1.2 - RMR classification (Forfori, 2020)

Parameter	Value	RMR index
Uniaxial compressive strength of intact rock material	500 kg/cm <sup>2</sup>	5
Rock Quality Designation (RQD)	95 – 100 %	20
Spacing of discontinuities	Medium > 200 cm	20
Condition of discontinuities	10 – 20 m; 1 – 5 mm; Rough; Soft filling < 5 mm; Unweathered	15
Groundwater conditions	10 - 25 litres/min; 0.1 – 0.2; Wet	7
<b>RMR'<sub>89</sub></b>		<b>67</b>
Discontinuities orientation rating		-5
<b>RMR</b>	<b>Class n. II - Good</b>	<b>62</b>

The GSI value is obtained starting from the RMR'<sub>89</sub> (Bieniawski, 1989) value using the expression proposed by Hoek et al. (1995):

$$GSI = RMR'_{89} - 5 = 67 - 5 = 62$$

This value corresponds to rock with discontinuity conditions "Good" and a "Blocky" structure, as Figure 1.8 shows.

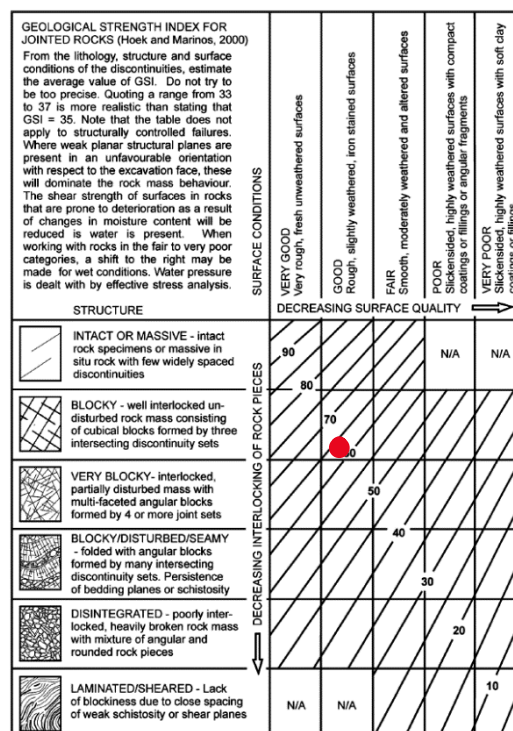


Figure 1.8 - Geological Strength Index for jointed rocks (Hoek and Marinos, 2000)

## 1.5. Exploitation plan

The open-pit quarry develops between 920 and 800 m a.s.l. The exploitation takes place by descending benches having a height from 3 m to 6 m. The average dimensions of a block extracted are 6 m in length, 3.4 m in width, and 3m in height.

Currently, the exploitation is organized with mechanical equipment, and the explosives are only occasionally used for reclamation operations.

The hauling of the machinery and of the blocks produced occurs using two 25-t derricks placed respectively on the western and eastern side of the site since there is no direct internal road network connecting the upper to the lower worksite.

The faces under exploitation are:

Lower worksite (829 m – 823 m a.s.l.)

- Oriented N 3° approximately vertical exposed to E (93°/89°)
- Oriented N 3° approximately vertical exposed to W (273°/89°)
- Oriented N 93° approximately vertical exposed to N (03°/89°)

Upper worksite (875.5 m - 869.5 m a.s.l.)

- Oriented N 36° approximately vertical exposed to SE (126°/89°)
- Oriented N 126° approximately vertical exposed to NE (36°/89°)
- Oriented N 126° approximately vertical exposed to SW (216°/89°)

At present, due to the problems relating to the quartz nodule, the works on the upper worksite were blocked. Also, the entrance, previously authorized for starting the underground exploitation, is abandoned. A new entrance is being moved 16 m away.



## 2. Chain saw cutting machine

In the quarry two different chain saw machines are used, due to different configurations of the work. In the portion of the open-pit quarry, the chain saw machine CSM-962/AN-PCD, type A-53/0, designed by Benetti Macchine is employed, instead for the underground excavation the Fantini GU70-R-XC chain saw machine is used.

The chain saw machine CSM-962/AN-PCD, type A-53/0, Figure 2.1 and Figure 2.2, is designed to make vertical cuts up to a maximum depth of 5 m and horizontal cuts up to a maximum depth of 4.5 m in marble, limestone, and similar stone.

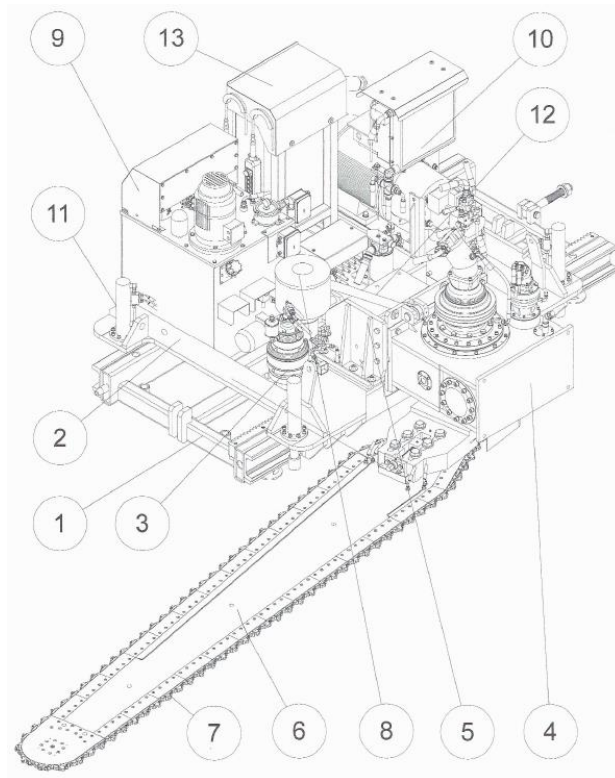
The cut is carried out employing a chain equipped with polycrystalline diamond tools (PCD), which runs on an arm equipped with special side guides.

The chain saw machine consists of the following main groups:

- Track equipped with rack
- Trolley (including arm holder head, cutting arm, greasing system, hydraulic system, translation unit, and electrical panel)

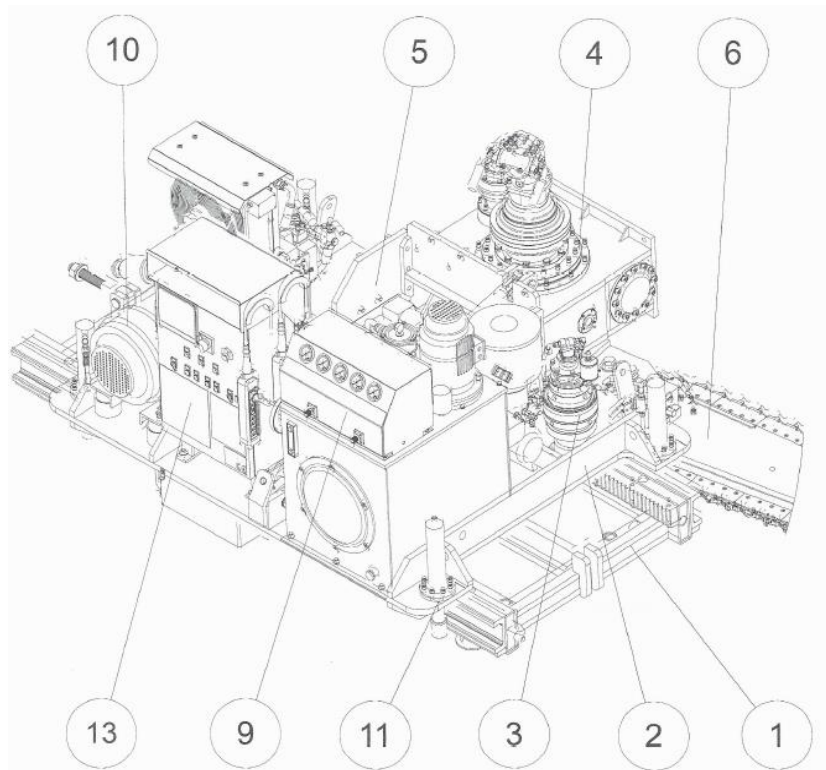
Hydraulic transmissions, with continuous speed adjustment, control all the movements of the machine. The instrumentation for controlling the working pressures on the various hydraulic circuits and the translation and rotation speed regulators are located on the control console.

The track must previously be levelled and fixed to the ground through suitable metal tools to prevent the movement of the track itself due to the machine's pressure during cutting operation.



**Figure 2.1 - CSM-962 chain saw machine, front view**

**1 Track, 2 Trolley, 3 Translation group, 4 Blade holder operating head, 5 Hinge group for positioning the operating head, 6 Cutting blade, 7 Chain, 8 Chain greasing system, 9 Hydraulic power unit, 10 Chains motor pump, 11 Trolley levelling cylinders, 12 Operating head overturning cylinder, 13 Electrical panel**



**Figure 2.2 - CSM-962 chain saw machine, back view**

**1 Track, 2 Trolley, 3 Translation group, 4 Blade holder operating head, 5 Hinge group for positioning the operating head, 6 Cutting blade, 9 Hydraulic power unit, 10 Chain's motor pump, 11 trolley levelling cylinders, 13 Electrical panel**

The technical characteristics of the machine are shown in Table 2.1.

*Table 2.1 - Technical data of the CSM-962*

TECHNICAL DATA OF THE MACHINE		
Electric motor chain	kW	45
Electric motor for hydraulic drives	kW	7.50
Electric motor for chain greasing system	kW	0.37
Hydraulic tank capacity	m <sup>3</sup>	0.30
Grease tank capacity	kg	25
Machine positioning speed	m/min	0.65
Machine speed in cutting phase	cm/min	0 ÷ 13
Speed of the chain	m/s	0 ÷ 1.20
Cutting width	mm	42
Length of the blade	m	3.50
Rotation of the blade	°	360
Machine weight with 3 m rail and 3.50 m cutting blade	kg	7000
3 m rail weight	kg	900
Dimensions of the machine with rail without cutting blade	m	1.86 x 3.09 x 1.60
3 m rail size	m	1.30 x 3.00 x 0.28

The sliding track of the machine is made of various elements that are modular and interchangeable, have a length of 3 m, and on one side of the tracks, there is a rack for the engagement of the pinion mounted on the machine.

Figure 2.3 shows the positioning and preparatory work of the chain saw cutting machine for the cut at the foot of the benches. In particular, the overturning of the cutting blade and its positioning in the cutting area is shown.



*Figure 2.3 - Preparatory work of the chain saw cutting machine*

For the underground excavation, the Fantini GU 70-R-XC chain saw machine, Figure 2.4, is designed and used to open a tunnel or to create a new opening in pre-existing tunnels. The machine is able to make vertical cuts up to a maximum length of 5 m and horizontal cuts up to a maximum depth of 3.50 m. This machine is equipped with tracks to easily reach also tricky environments.



*Figure 2.4 - Fantini chain saw machine*

The technical characteristics of the machine are shown in Table 2.2.

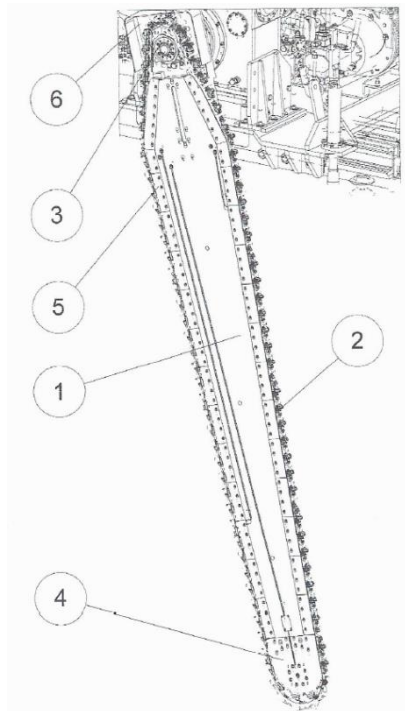
Table 2.2 - Technical data of the Fantini GU 70-R-XC

TECHNICAL DATA OF THE MACHINE		
Electric supply	V	400
Total power installed	kW	56
Hydraulic tank capacity	l	450
Grease tank capacity	m <sup>3</sup>	0.30
Machine positioning speed	m/min	0.65
Machine speed in cutting phase	cm/min	0 ÷ 10
Speed of the chain	m/s	0 ÷ 1.20
Cutting width	mm	42
Length of the blade	m	3.50
Arm rotation	°	360
Dimensions of the machine	m	9.50 x 4.30 x 5.55

For both machines, the cut is performed by the cutting blade equipped with guides, in which a metal mono-link chain, 74 mm pitch, cutting width 42mm, runs equipped with polycrystalline diamond plate tools, produced by the company LANDS Superabrasives. The tool has a diameter of 8 mm, a diamond layer thickness of  $2.0 \pm 0.3$  mm, a Tungsten Carbide (WC) thickness of  $6.0 \pm 0.3$  mm, a total height of 8.1 mm. The zone of the WC is directly welded on the toolholder.

Chain lubrication is achieved by injecting grease under pressure through injectors placed inside the cutting blade itself. The machine is equipped with a "blade holder operating head", which transmits the rotation motion to the blade, transferring the movement to the cutting chain, and able of positioning, through its overturning, the cutting chain in the vertical and horizontal working position.

The cutting blade, Figure 2.5, consists of a one-piece body made of special steel equipped with mechanically fixed internal and external guides.



*Figure 2.5 - Cutting blade*  
1 Cutting blade, 2 Cutting chain, 3 Motor sprocket of the cutting chain,  
4 Cutting blade head, 5 External guides, 6 Chainwheel safety guard

The machine uses a mono-link cutting chain 74 mm pitch, cutting width 42 mm, consisting of external and internal links connected by pins locked through special hooks. Polycrystalline diamond tools, 8 mm diameter, are mechanically fixed on the bit holders. Seven sets of tools are installed on the cutting chain, for a total of 84 tools. Each series comprises twelve different toolholders so numbered: 1 2 3 4 5 6B 6A 7B 7A 8B 8A 8. The numbers of each toolholder correspond to a different cutting configuration; the width of the cut progressively increases with the numbering of the tool holder up to the design that occurs in the toolholder 8, where two PCD tools are installed at the ends of the mesh to guarantee the established cutting width. Figure 2.6 shows the sequence of toolholders and PCD tools. Figure 2.7, instead, provide a zoom and a front view of the cutting chain.

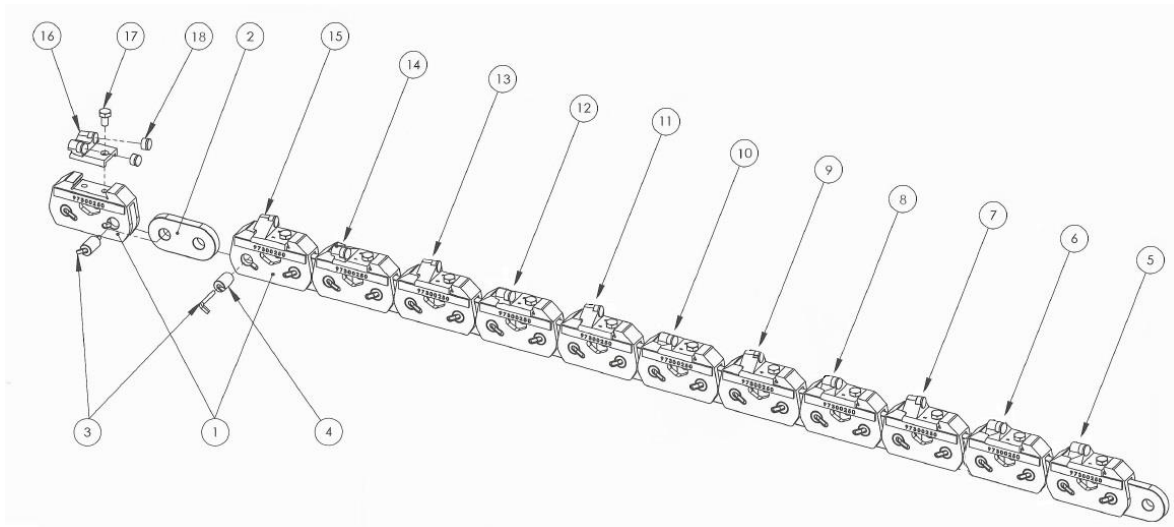


Figure 2.6 - Serie of toolholders and PCD

1 Outer mesh, 2 Inner mesh, 3 L-shaped pin for cutting chain, 4 Pin, 5 Toolholder 1, 6 Toolholder 2, 7 Toolholder 3, 8 Toolholder 4, 9 Toolholder 5, 10 Toolholder 6B, 11 Toolholder 6A, 12 Toolholder 7B, 13 Toolholder 7A, 14 Toolholder 8B, 15 Toolholder 8A, 16 Toolholder 8, 17 Screw, 18 PCD tool.

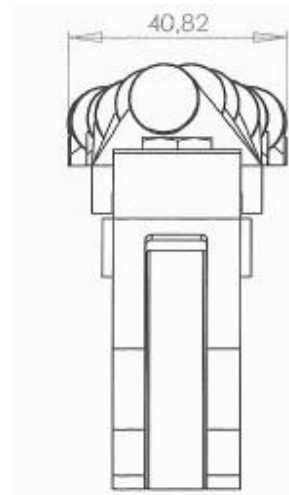


Figure 2.7 - Zoom of the toolholder (left), cutting chain front view (right)

The core of this structure, abundant in quartz, proved impossible to cut, given the rapid wear of the cutting tools, consuming the PCD tools in a short time, and also their support structure. Figure 2.8 shows a visual assessment of the PCD tools.



Figure 2.8 - PCD tools. The first tool is new, the others are damaged and unusable

## 2.1. Cutting theory

Between marble and tools take place, during the cut, a process of mutual destruction, which is desired on the rock side but is suffered on the tool side: the shape and the composition of the tools are established in order to minimize these destructive effects. Therefore, the tool must be hard enough not to suffer local abrasions by the rock and be tough, i.e., not to fragment when the load is suddenly applied.

In this section are present two theories of the action of the tools on the rock. Probably it does not exist in this field the possibility of establishing a theory with general validity since every rock has a different behaviour than the other. However, it may be helpful to examine some proposed models regarding the theorization of the elementary mechanism of the detachment of the rock by the tools.

### 2.1.1. Ultra-simplified model of the action of a drag tool

It is a model that allows predicting quite well the forces to be applied to the tools to perform the cut. This model is employed in the case of drag tools used with a small pass compared to the width of the cut, with linear cutting edge and zero angles of attack or close to zero (neutral tool).

The cutting force and the force normal to the cutting direction are considered separately. It is assumed that the tools are rigidly guided in the cutting path, the cut occurs by the detachment of flat chips, i.e., with flat separation surfaces (Mancini and Cardu, 2001).

The rock is supposed to be characterized:

- from a plasticization pressure  $p$ , a pressure which gives rise to the plastic failure of the rock
- from a pure shear strength  $\tau$
- from an internal friction angle  $\varphi$ , and from an internal friction coefficient  $c = \tan \varphi$

The cut takes place by successive detachments of chips: it is, therefore, on a small scale, a cyclical phenomenon. Three consecutive phases of a cycle are outlined below in Figure 2.9.



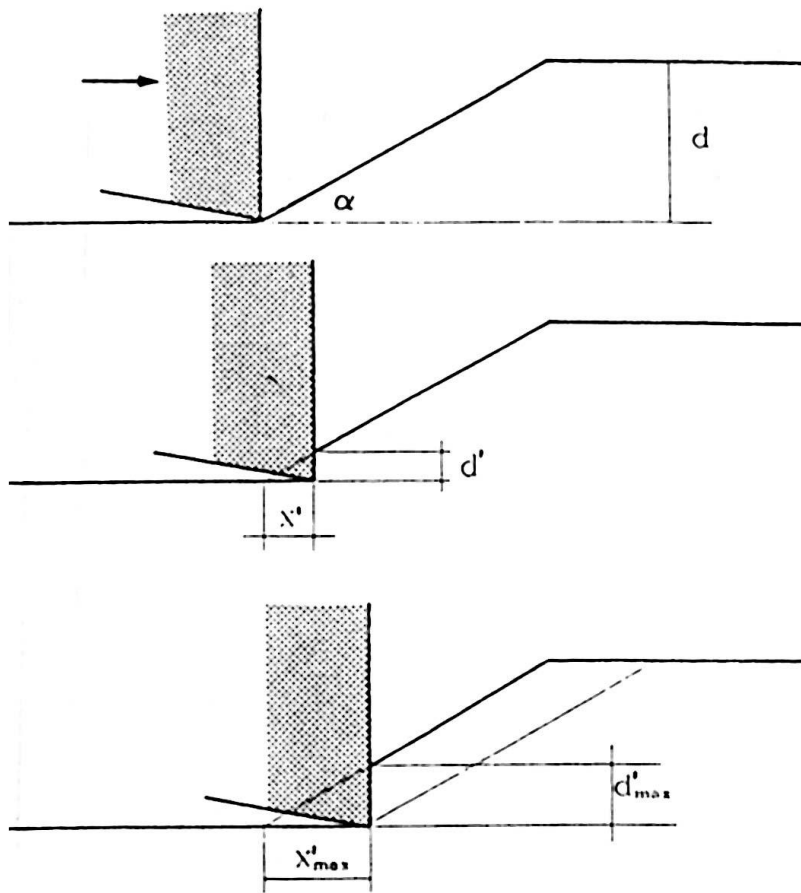


Figure 2.9 - Cutting cycle (Mancini and Cardu, 2001)

#### 2.1.1.1. Cutting force

Among all the potential detachment surfaces, it can be shown that the one that requires the minimum value of the cutting force  $F_t$  to reach failure is the inclined surface of  $\alpha = 0.5 \arctan(1/c)$  with respect to the direction of the cutting force. The chips, therefore, detach themselves according to a plane inclined of  $\alpha$  with respect to the direction in which the tools advance. So, the shear force necessary to obtain the chips' detachment can be calculated by knowing the pass  $d$ , and the two geomechanical characteristics,  $\tau$  and  $c$ .

$$F_{max} = \frac{d * \tau}{[\sin \alpha * (\cos \alpha - c * \sin \alpha)]}$$

The force that the tool can transmit to the rock is not constant during the cycle: it is given by the product of the contact surface between the tool and the rock multiplied by the pressure of plasticization, before defined.

With reference to the unit of length of the cutting edge:

$$F_t = p * d'$$

where  $d'$  is the contact surface.

Assuming that a cycle begins immediately after the detachment of a fragment, if the previously detached scrap was flat, with the detachment surface inclined by  $\alpha$  with respect to the direction of the cutting motion, the support surface, and therefore the force, increase proportionally with the increase of the path  $x$  according to:

$$F_t = p * d' = p * x * \tan \alpha$$

Therefore, the force  $F_t$  increase until it reaches the value  $F_{max}$ , necessary to obtain the detachment of a subsequent fragment. This happens when the tool has completed the  $x_{max}$  path. Once the detachment occurs, the force  $F_t$  is equal to zero and, if the movement of the tool continues, another cycle begins. If the tool's speed is constant, the cutting force has a sawtooth trend over time, varying rhythmically from 0 to  $F_{max}$ , a typical tendency is shown in Figure 2.10.

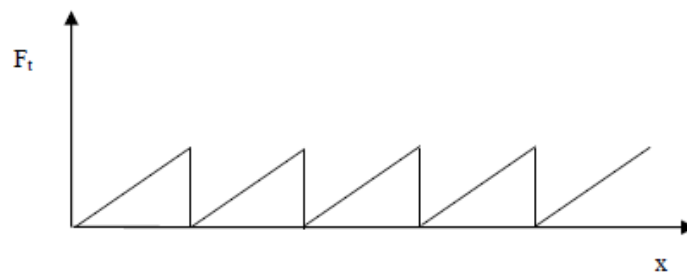


Figure 2.10 - Cutting force diagram

#### 2.1.1.2. Contact force

To oblige the tool to follow the desired cutting trajectory, it is also necessary to provide a contact force  $F_a$ , normal to the cutting force. Without this force, the tool would be pushed out of the groove it is creating. According to the model being examined, the contact force is given by the product of the shear force by the friction coefficient  $C$ :

$$F_a = F_t * C$$

This model describes, in terms of mechanical resistance, the phenomenology for simple cases, such as simulating the cut of the chain saw cutting machine in inhomogeneous rocks at the cut scale.

Also in this case, the force/advancement diagram, Figure 2.11, is still sawtooth, but the teeth have different heights along the cutting path because  $F_{max}$  changes at each cycle.

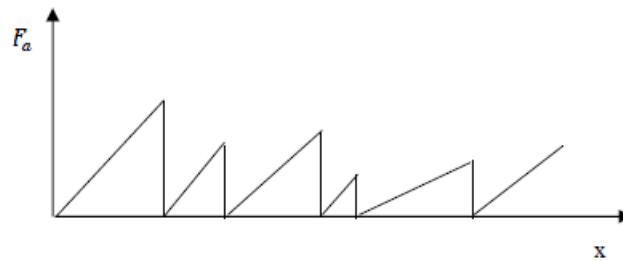


Figure 2.11 - Contact force diagram

### 2.1.2. Nishimatsu model

It is a considerably more elaborate model and formally applicable to positive, neutral, or negative drag tools. In this model the tool is characterized by an angle of attack  $\alpha$ , the rock by the envelope of Mohr's circles, and the interaction between the two by a friction angle  $\phi$  (Nishimatsu, 1972).

Nishimatsu (1972) considers the force necessary to detach the chips after the penetration of the tool, in which it recognizes different phases. Assuming that the resulting state stress is variable according to the distance of the point considered from the cutting edge, he admits that in the same plane, the direction of the resulting stress is constant and, therefore, is constant also the ratio between the tangential and normal stresses.

The scheme of the forces and the stresses are shown in the Figure 2.12:

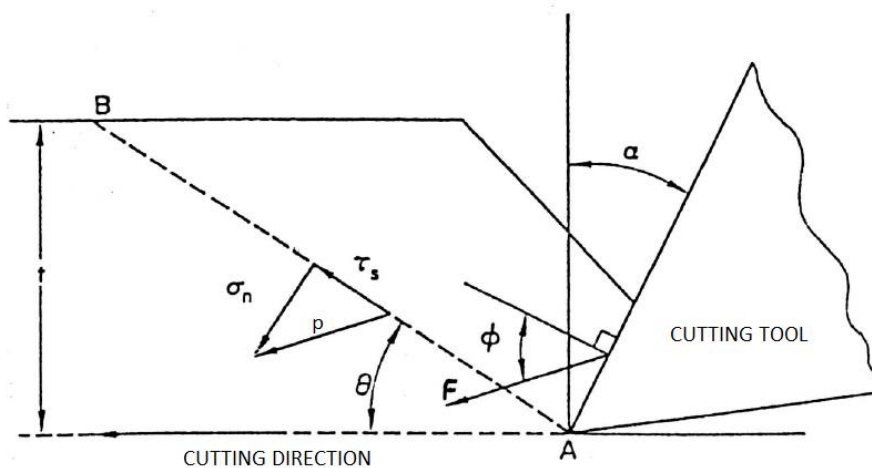


Figure 2.12 - Nishimatsu model: forces and stress scheme (Nishimatsu, 1972)

where  $t$  is the pitch of the tool,  $F$  is the tool's force,  $\vartheta$  is the angle of potential detachment,  $\tau_s$ ,  $\sigma_n$  and  $p$ , respectively, the tangential component, the normal component, and the resultant of the stress in a generic point of A-B.

So, the hypothesized stress distribution equation is:

$$p = p_0 * \left( \frac{t}{\sin \vartheta} - \lambda \right)^n$$

where:

- $\lambda$  is the distance of the considered point from A
- $p_0$  is a constant to be determined
- $n$  is the stress distribution factor

Of course, the expression in brackets is none other than the distance of the considered point on the line A-B starting from point B; therefore, the hypothesis is that the stress  $p$  is zero at point B, reaching the maximum value in A, at the cutting edge.

Subsequently, Nishimatsu derives  $p_0$  imposing the balance between the force  $F$  applied by the tool and the resultant of the stresses along A-B, obtained by integrating the value of  $p$  on the length BA:

$$p_0 = - (n - 1) * \left( \frac{t}{\sin \theta} \right)^{n+1} * F$$

From this expression, obtains the value of  $p$  in correspondence with  $\lambda = 0$ , i.e., in correspondence of the contact with the cutting edge. Subsequently, decomposes the value of the resultant of the stress into the normal and tangential components, obtaining the expressions of the stresses of the rock at the point considered:

$$\sigma_{n_0} = - (n - 1) * \frac{\sin \theta}{t} * F * \sin(\theta - \alpha + \varphi)$$

$$\tau_{s_0} = - (n - 1) * \frac{\sin \theta}{t} * F * \cos(\theta - \alpha + \varphi)$$

Nishimatsu (1972), therefore, assumes that the material is characterized by a linear Mohr circles envelope, expressed by:

$$\pm \tau_s = S_s - \tan(K * \sigma_n)$$

where  $S_s$  is the pure shear strength,  $K$  is the internal friction angle, and the sign of the compressive stresses is assumed to be negative.

By substituting the values of  $\tau$  and  $\sigma$  in this expression, Nishimatsu (1972) obtain  $F$ , which leads to the failure condition of the material, and therefore to the initiation of breakage:

$$F = - \frac{1}{n + 1} * \frac{t}{\sin \theta} * \frac{S_s}{\tan K * \sin(\theta - \alpha + \varphi) - \cos(\theta - \alpha + \varphi)}$$

and finally, Nishimatsu (1972) decompose the force  $F$  in the direction of the tool motion and in the normal direction, obtaining respectively the cutting force and the contact force:

$$F_t = F * \cos(\varphi - \alpha)$$

$$F_a = F * \sin(\varphi - \alpha)$$

As for the stress distribution factor  $n$ , it proposes, on an experimental basis, the expression:

$$n = 11.3 - 0.18 * \alpha^0$$

where  $\alpha^0$  is the angle of attack, in degrees.

For the friction angle of the rock cut  $\varphi$  provides experimental values, oscillating between 22° and 25°, for some materials.

The shear force value obtained by Nishimatsu (1972) is the peak value that should be found in the cycle.

### 2.1.3. Comments on the examined models

In the two models examined, the problem is considered to be flat, which severely limits the possibility of applying these models to real cases.

Another point that deserves reflection is that: all the models examined conclude that the shear force is proportional to the pitch. With reference to the plane problem (but the same considerations also apply to the 3D problem), it is easy to demonstrate that this implies that the specific excavation work is always the same independently on the distance between the tools.

It is known that less work is spent on excavating a specific volume by operating with a large pitch with respect to a small one. This happens due to the greater incidence of dissipations occurring with a small step, which is justified by an interesting reason. The resistance of the excavated material to the shear, tensile or compressive stresses depends on the scale at which the material is considered. To predict the excavation shear force necessary with a small step, it is required to use

the resistance value characteristic of the behaviour of that material on a small scale, which is systematically greater than the values that characterize it on a larger scale.

This aspect greatly reduces the predictive value of these models, but it is helpful to understand the force that influence the chain saw cutting machine's work.

### 3. PCD SEM-EDS analysis

In order to understand the structure and the composition of the polycrystalline diamond tools employed for the cutting operations, some chemical analysis with a Scanning Electron Microscopy (SEM) - Energy Dispersive X-ray Spectrometry (EDS) were carried out.

Scanning Electron Microscopy (SEM) is a test process that scans a sample with an electron beam to produce a magnified image for analysis. Electron microscopy is performed at high magnifications, it generates high-resolution images, and precisely measures very small features and objects. The signals generated during SEM analysis produce a two-dimensional image and reveal information about the sample, including external morphology (texture) and chemical composition when used with the EDS feature.

SEM uses a focused beam of high-energy electrons to generate a variety of signals at the surface of solid specimens. In SEM microscopy applications, data is collected over a selected area of the surface of the sample, and a two-dimensional image is generated that displays spatial variations in properties, including chemical characterization, texture, and orientation of materials. The EDS detector separates the characteristic X-rays of different elements into an energy spectrum. EDS system software is used to analyse the energy spectrum to determine the abundance of specific elements.

At the Politecnico di Torino laboratory, a Scanning Electron Microscope Leo 1450 MP + Energy Dispersive X-ray Spectrometry probe was used. The tests were performed on three tool samples: one new tool, one chipped, and one completely worn (the diamond layer was completely worn out with respect to the widia support structure).

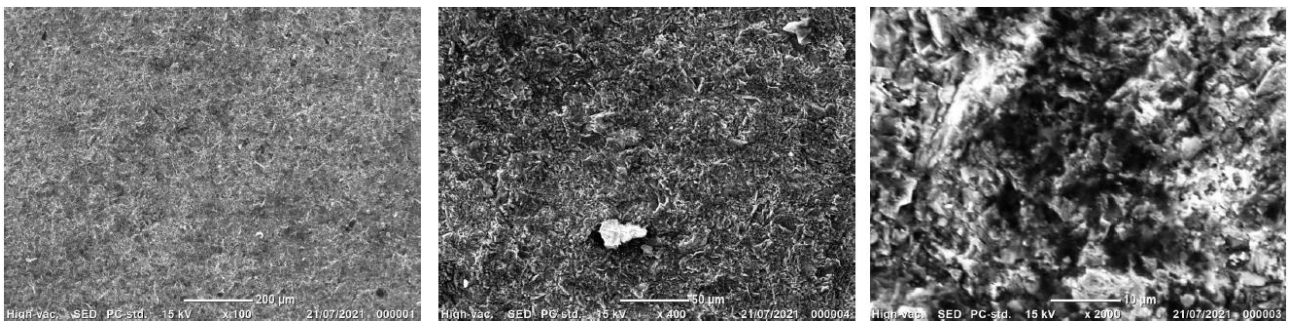
### 3.1.Results

- Sample 1, Figure 3.1

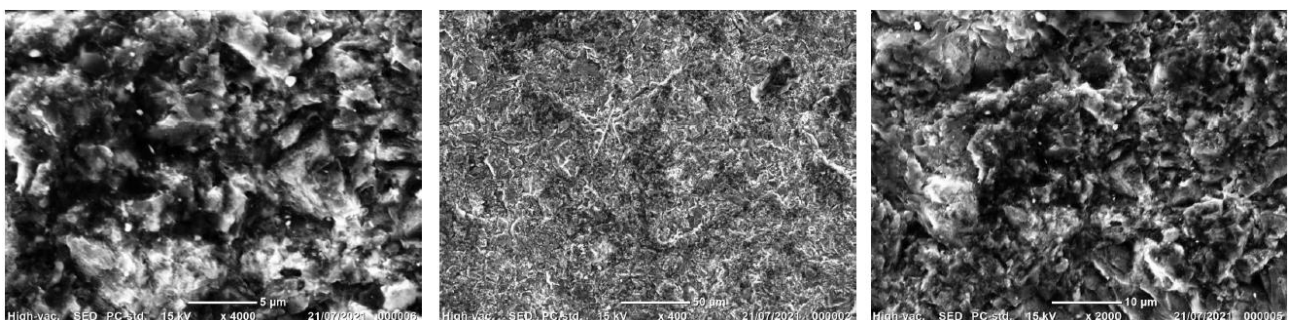


*Figure 3.1 - Sample 1, new tool*

For the new tool, two areas were evaluated and, for each of them, a series of images in secondary electrons at different magnifications are proposed (Figure 3.2 and Figure 3.3).



*Figure 3.2 - SEM analysis: new sample, area 1*

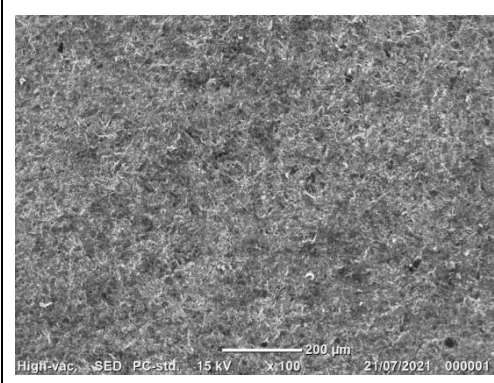


*Figure 3.3 - SEM analysis: new sample, area 2*

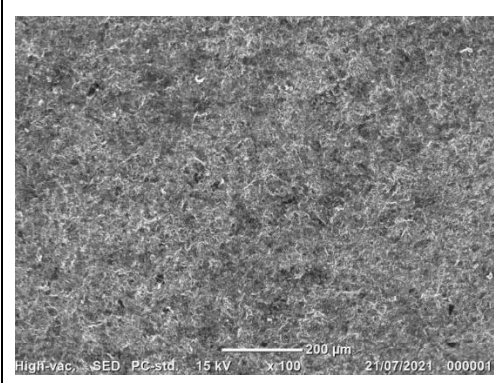


The semi-quantitative chemical results, in atoms %, achieved with the EDS, performed with the image at a magnification of 100x, are proposed in Table 3.1 and Table 3.2.

*Table 3.1 - EDS analysis results: new sample, area 1*

	Element	Area 1
	C	90.99
	O	7.52
	Al	0.28
	Co	1.21
	W	-

*Table 3.2 - EDS analysis results: new sample, area 2*

	Element	Area 2
	C	92.20
	O	6.42
	Al	0.19
	Co	1.10
	W	0.08

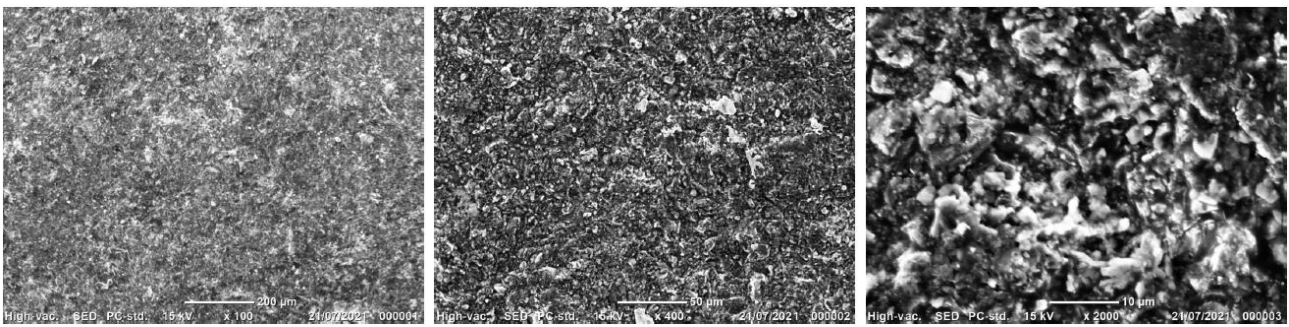
The results showed that the surface is almost completely made of C, and this is completely reasonable for the diamond coating.

- Sample 2, Figure 3.4

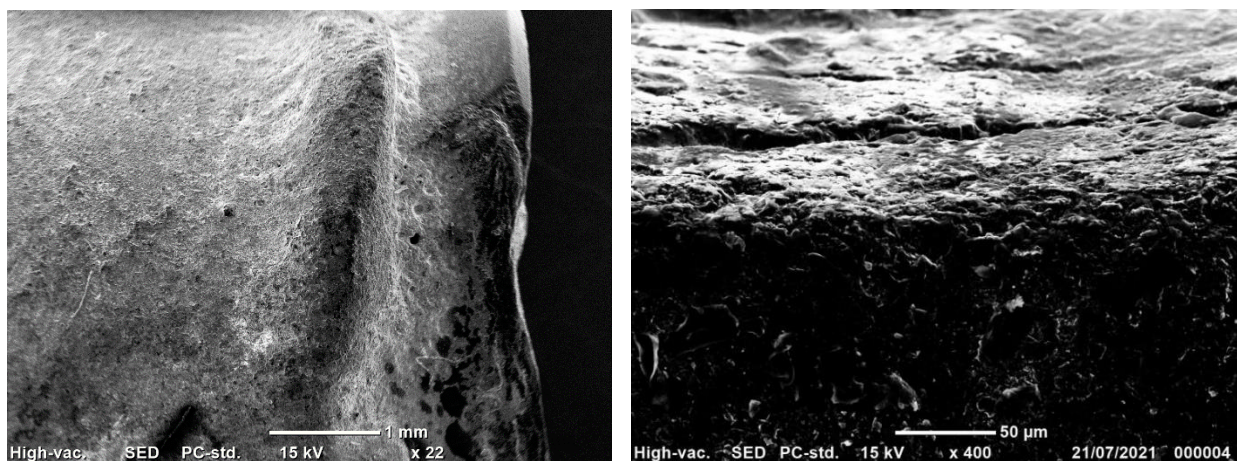


*Figure 3.4 - Sample 2, chipped PCD tool*

For this sample, two areas were evaluated, a series of images in secondary electrons at different magnifications are proposed (Figure 3.5 and Figure 3.6).



*Figure 3.5 - SEM analysis: chipped sample*



*Figure 3.6 - Zoom on the chipped zone*

The EDS analysis was performed in 6 different points, and it revealed different compositions for the six areas. The zone 4 (Figure 3.7) shows a chemical composition very similar to those obtained from the new tools. Instead, in the zone 2 – 3 – 5 (Figure 3.7), the chemical elements are different due to the probable residue of some cutting material or fluorinated precursors of the diamond like carbon not yet completely transformed, but production techniques and reference literature should be deeply investigated in order to obtain detailed information. The zone 1 and 6 (Figure 3.7), instead, correspond to the support structure, however the results achieved refers to the weld surface layer, rich in Ag, Cu, and Zn, and not to the widia support structure.

The results, in terms of atoms percentage, of these analyses are report in Table 3.3.

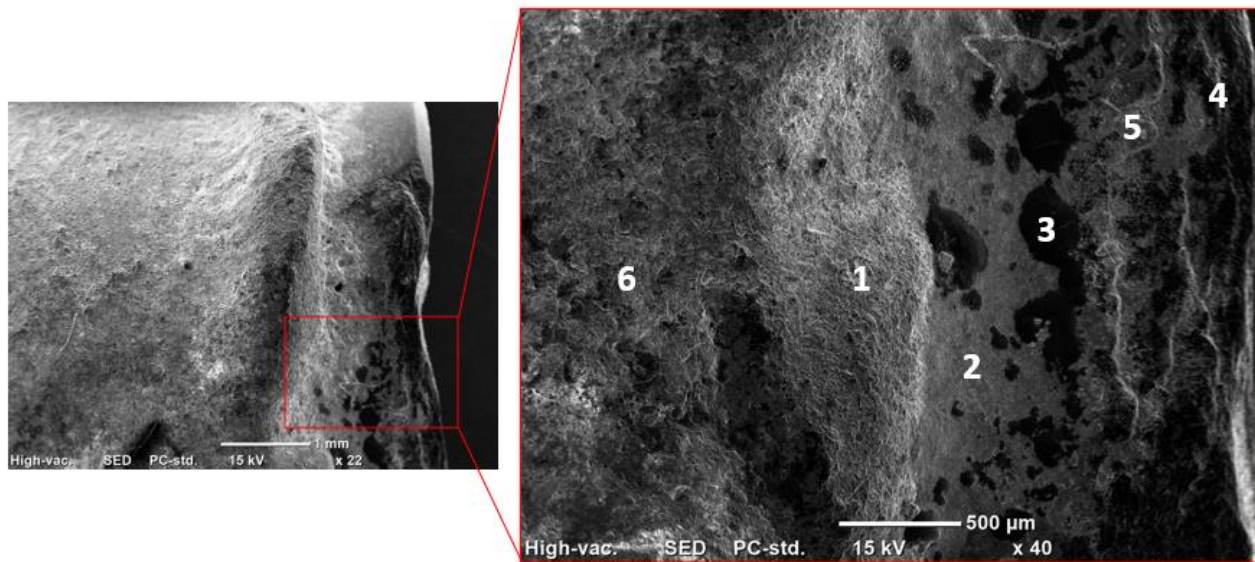


Figure 3.7 - EDS analysis: chipped sample

Table 3.3 - EDS analysis results: chipped sample

Element	6	1	2	3	5	4
C			8.73	3.72	29.53	77.13
O	54.55	59.57	54.54	60.82	45.50	14.97
F	17.60	12.80	28.95	24.15	17.34	4.67
Na			0.74	0.48	0.52	0.53
K	9.82	3.52	7.04	10.83	6.98	2.48
Cu	7.40	10.13				
Zn	6.21	7.70				
Ag	4.42	6.27				
Cl					0.13	0.23

- Sample 3, Figure 3.8



Figure 3.8 - Sample 3, completely worn PCD tool

Also for this sample two areas were evaluated, and a series of images in secondary electrons at different magnifications are proposed (Figure 3.9 and Figure 3.10).

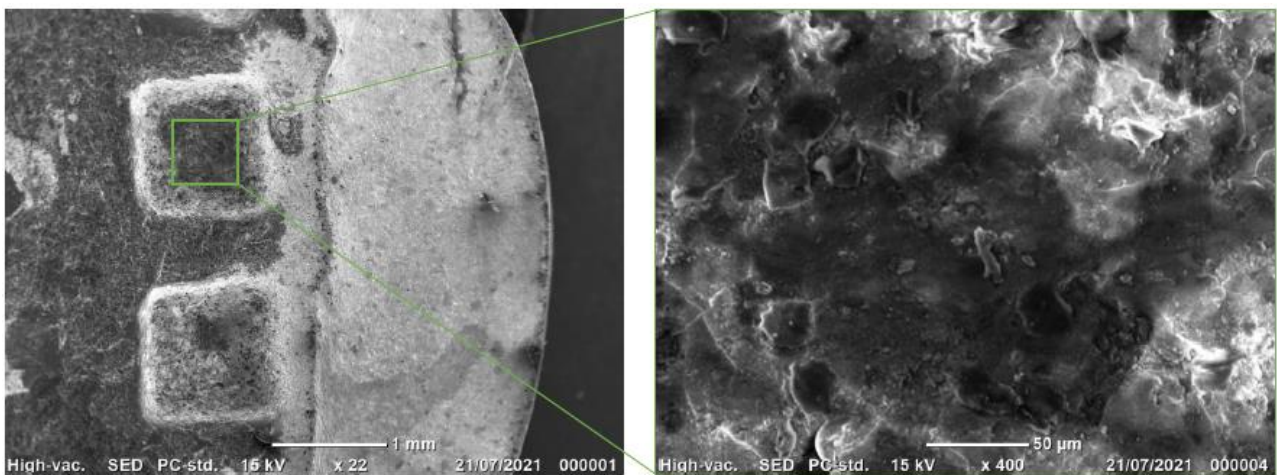


Figure 3.9 - SEM analysis: detached sample, area 1

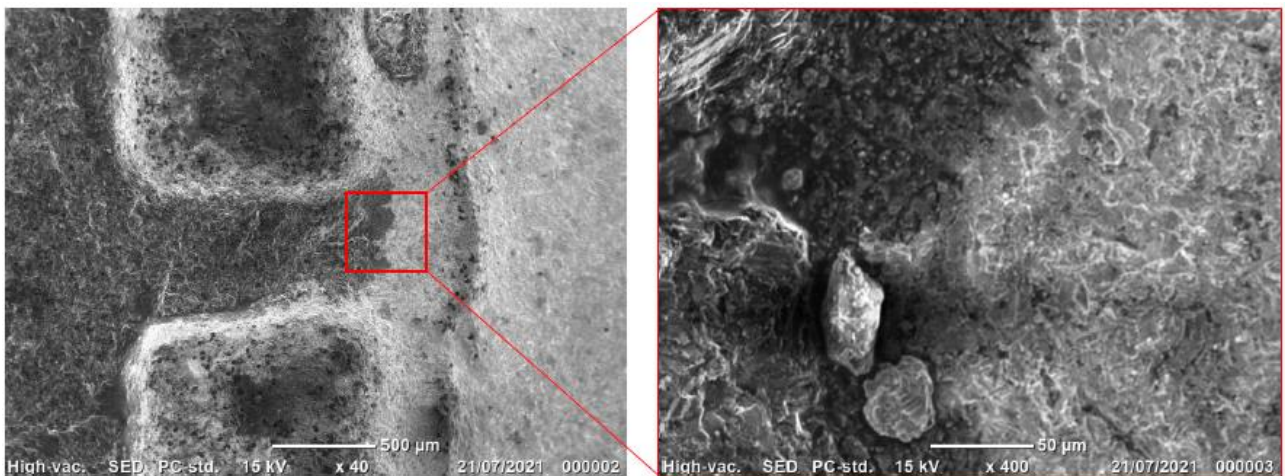


Figure 3.10 - SEM analysis: detached sample, area 2

The EDS analysis was performed in 3 different points, and it revealed different compositions of the investigated areas. In the zone highlighted in blue (Figure 3.11) a chemical composition in which F, K, and O are abundant was noticed. In the red zone, the chemical elements confirm the same composition given by the manufacturer; in fact, it is rich in W and Co. The green zone shows a chemical composition very similar to those obtained from the new tools, i.e., rich in C.

Figure 3.11 shows the results achieved for the three different zones of the tool.

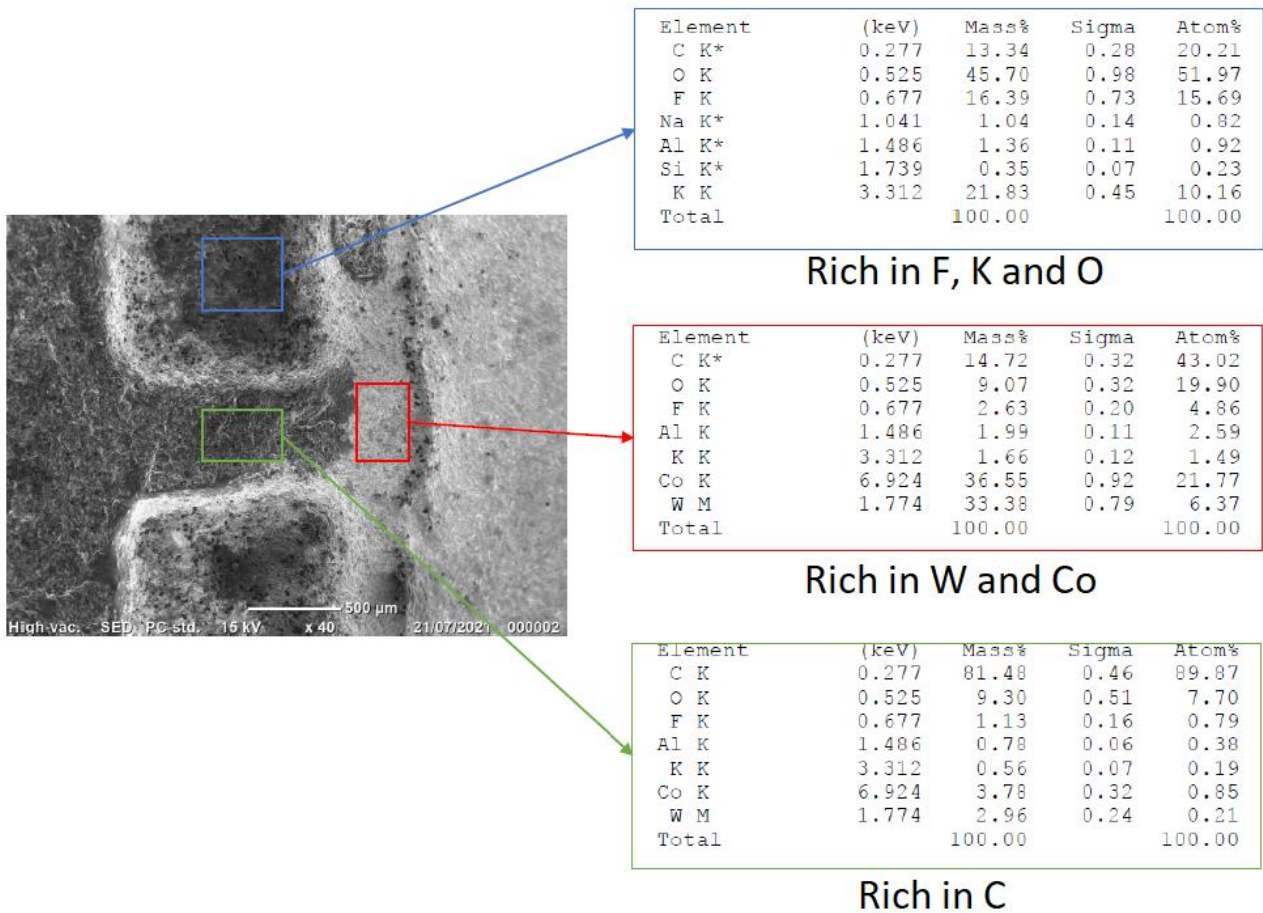


Figure 3.11 - EDS analysis: completely worn sample

## 4. Laboratory analysis

### 4.1. Petrographic analysis

In order to carry out a petrographic exam on the different varieties of marble extracted at the quarry, two red-green Cipollino marble thin sections and two thin sections related to the grey-white marble were prepared. The S.S.\_01 and S.S.\_02 are the two thin sections relative to the Cipollino marble, the S.S.\_03 and S.S.\_04, instead, refers to the grey-white marble.

#### S.S.\_01

**Hand specimen proprieties:** green, red, and white calcschist composed of plurimillimetric black, red, and green more prominent veins. In the slabs, metamorphic folds and structures can be observed.

**Thin section proprieties:** under the microscope, 40x magnification, the specimen is composed of a calcitic microcrystalline mosaic, alternating with laminas where muscovite, chlorite, and quartz are observed. Figure 4.1 are shown the picture of the analysed zone taken directly with the microscope.

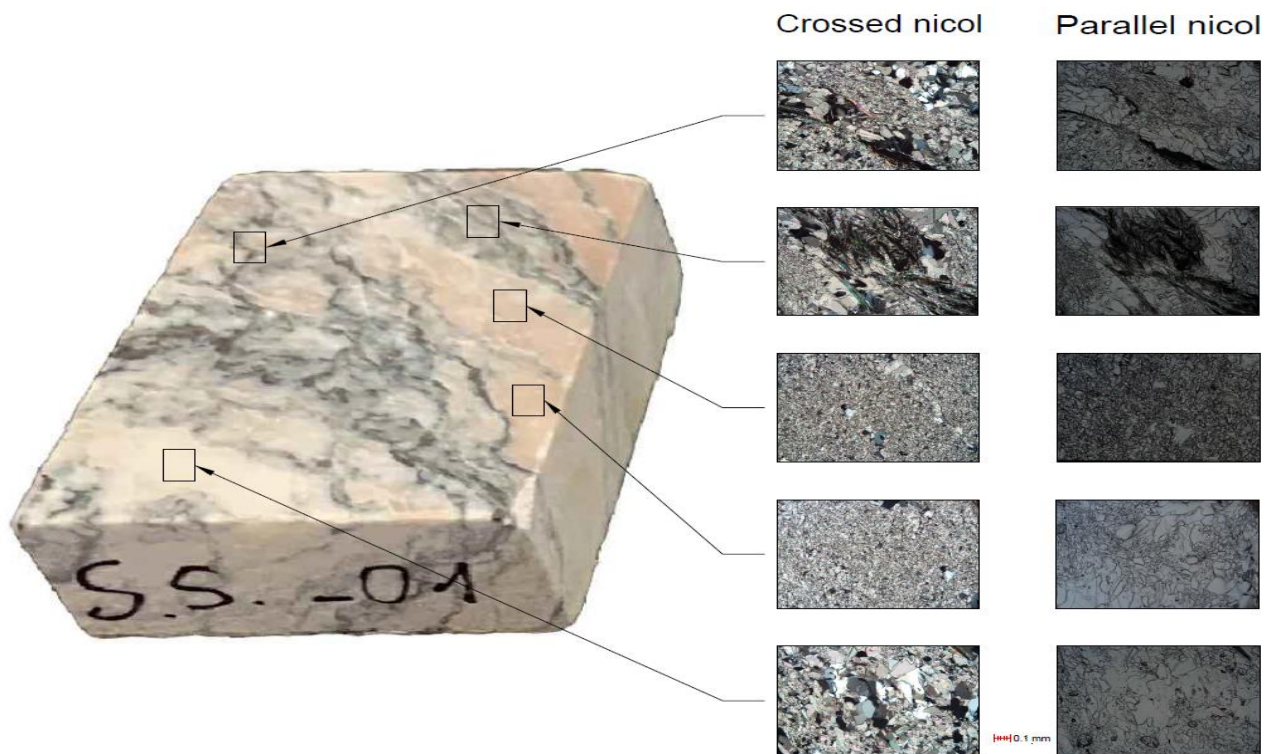


Figure 4.1 - Thin section S.S.\_01

## S.S.\_02

**Hand specimen proprieties:** green and red calcschist composed of plurimillimetric white, black, and green more prominent veins.

**Thin section proprieties:** Under the microscope, 40x magnification, the sample is composed of very fine to medium calcite, alternating with several small veins in which micas, chlorite, and quartz are observed. Figure 4.2 shows the crossed nicol and the parallel nicol picture taken with the petrographic microscope.

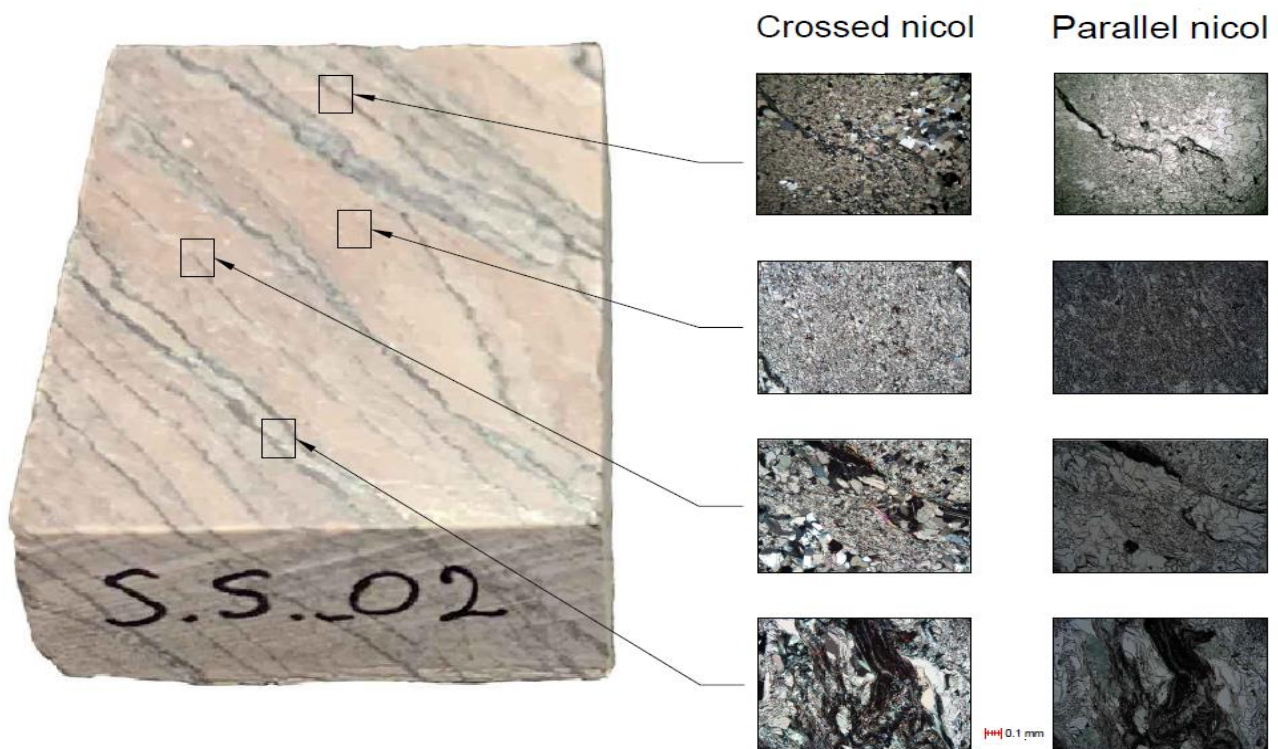


Figure 4.2 - Thin section S.S.\_02

### S.S.\_03

**Hand specimen proprieties:** Metamorphic compact crystalline rock, mainly composed of calcite crystals ranging from very fine to medium. No preferred orientation is detectable on the hand specimen. The rock is almost entirely homogeneous except for the presence of thin, very fine-grained phyllosilicates layers with random orientation.

**Thin section proprieties:** Low-grade metamorphic rock with granoblastic texture mainly composed of calcite crystals, i.e., marble, with dimension from very fine to medium, with subordinate quartz, K-feldspar, white mica, chlorite, and graphite (organic remnants), from very fine to fine dimension. Calcite crystals vary from very fine to medium, where the crystals are medium-sized; they seem to be previous calcite-quartz veins re-deformed. The rock shows no preferred orientation nor foliation.

Figure 4.3 shows the picture of the analysed sample.

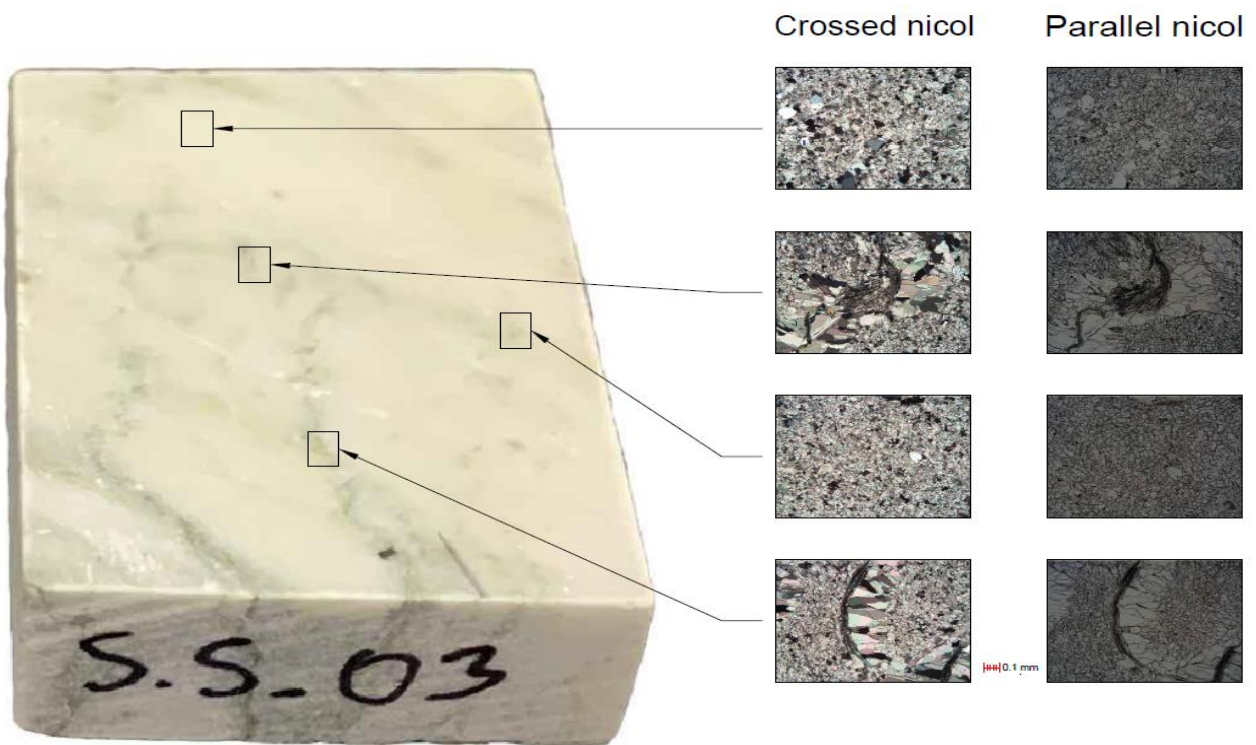


Figure 4.3 - Thin section S.S.\_03



## S.S.\_04

**Hand specimen proprieties:** the sample shows a white portion characterized by greenish veins, due to the phyllosilicates, and a greyish portion, due to the presence of flinty limestone and quartz.

**Thin section proprieties:** Under the microscope, the white part appears to be a fine-grained marble, with an average grain size of about 100  $\mu\text{m}$ , but with a substantial variation in grain; in fact, larger crystals and portions of deformed calcite veins are present. The greenish veins instead are characterized by calcite, quartz, and phyllosilicates. The calcite here has larger dimensions regarding the white part, and they are continuously deformed calcite veins. The phyllosilicates are represented by microcrystalline muscovite, very folded. In the lower part of the thin section, the rock is characterized by this greyish colour. This portion of the rock is derived from the recrystallization of carbonate rock with an important component of quartz; it is estimated that the percentage of quartz is about 12%.

Figure 4.4 shows the analysed sample.

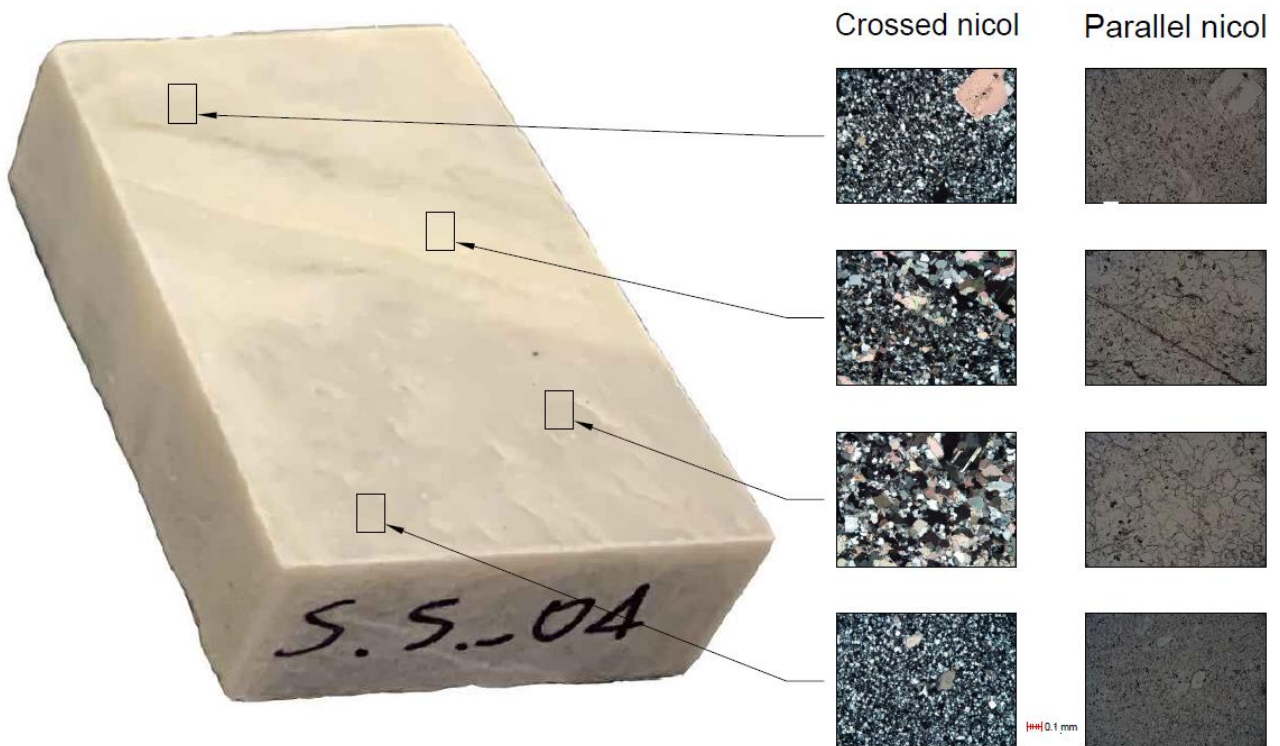


Figure 4.4 - Thin section S.S.\_04

## 4.2. Vickers microhardness test

Hardness is a measure of the resistance to localized plastic deformation induced by either mechanical indentation (Ashby, 1951), and it is determined by measuring the permanent depth of the indentation.

In simpler words, keeping constant the load and the characteristics of the indenter: more minor is the indentation, harder is the material. The hardness value is obtained by measuring the length of the mark left, knowing the applied load.

The Vickers hardness tester uses the hardness test developed by Smith and Sandland (1922) at Vickers Ltd to measure the hardness of materials. The Vickers test is often easier to use than other hardness tests since the required calculations are independent of the size of the indenter, and the indenter can be used for all materials irrespective of hardness.

The Vickers method is based on an optical measurement system (Germak et al., 2006). The microhardness test procedure specifies a range of light loads using a diamond indenter to create a recess measured and converted to a hardness value.

The determinations of Vickers hardness were carried out on samples of white marble and green-red Cipollino, taken at the Penna dei Corvi quarry. The specimens, 50 x 30 x 15 mm in size, have a perfectly polished upper surface, which is required for this type of test.

A Leitz Wetzlar Durimet, Figure 4.5, equipped with the Vickers indenter was used to carry out the tests. The microdurimeter is an instrument intended for measuring the hardness of materials. It penetrates the material's surface, leaving an imprint on the tested point. Depending on the size of the mark and the load used, the microhardness value can be calculated.

The Vickers indenter consists of a square pyramid-cut diamond with an opening of  $136^\circ$ , as show Figure 4.6. The hardness value is obtained as the ratio between the force exerted and the length of the indenter impression. Therefore, the units of measurement of the Vickers scale are those of pressure, that is, a load on a surface.



Figure 4.5 - Leitz Wetzlar Durimet

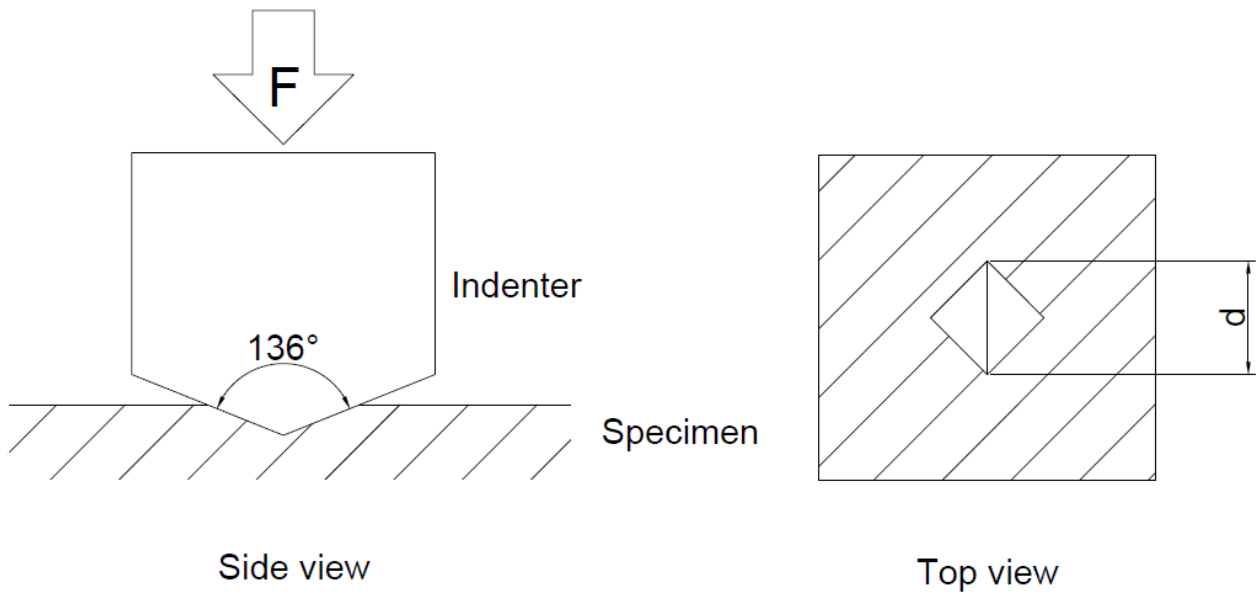


Figure 4.6 - Schematic of indentation (Smallman & Ngan, 2014)

The tests were carried out respectively on four specimens of white marble and four specimens of green-red Cipollino.

The tests were performed according to the following steps:

1. The specimens were first polished and mounted on a glass slide with interposition of plastic material. By pressing with a small press, parallelism was achieved between the section's polished surface and the instrument's support base.
2. The sample was taken to the microdurimeter, clamped, and placed under the 10x lens. Looking through this lens, the operator put the image on focus thanks to a macro-metric knob.
3. A weight of 200 g (1.96 N) was positioned in its hub. After that, the indenter was placed on the sample by rotating the platform that held both the lenses and the indenter.
4. By activating an oil press, the weight-indenter system starts its pushing action against the material's surface. It remains there for approximately 45 s, also known as dwell time, in which the indenter leaves its imprint on the material's surface.
5. After the dwell time, the indenter was lifted from the surface, and the operator moves the 50x lens on top of the sample to detect the mark left. The mark was seen and measured with a scale having a 20  $\mu\text{m}$  resolution impressed on the lens by moving it until the lower apex of the mark touched the 0-line placed at the bottom of the lens. The value to be noted was the last score crossed by the prismatic shape of the indentation. This first measuring scale has a 200  $\mu\text{m}$  range. A second scale, having a 0.5  $\mu\text{m}$  resolution and a 20  $\mu\text{m}$  range, could be seen in the ocular under the image. The more accurate measurement was done by rotating a small wheel placed on the left of the ocular until the upper apex of the indentation touched the same score recorded during the first measurement. The final value of the indentation length is the sum of the first value and the value that is read on the high-resolution scale.
6. The Vickers hardness value is calculated with the formula proposed below, which related the load to the imprint dimension.
7. The indentation spot will move to 100  $\mu\text{m}$  before starting the following test to ensure that the footprints do not interfere with each other.

The Vickers microhardness, in MPa, is expressed by the following formula (Mott, 1956):

$$HV = \frac{1854 * P}{d^2}$$

where:

HV: Vickers microhardness [MPa]

P: load on the indenter [N]

d: length of the indenter diagonal left by the indenter [ $\mu\text{m}$ ]

80 microhardness measurements were done for each specimen. The microhardness values for each sample are sorted in ascending order, and subsequently, the values can be displayed in terms of cumulative frequency, yielding a characteristic curve.

#### 4.2.1. Results

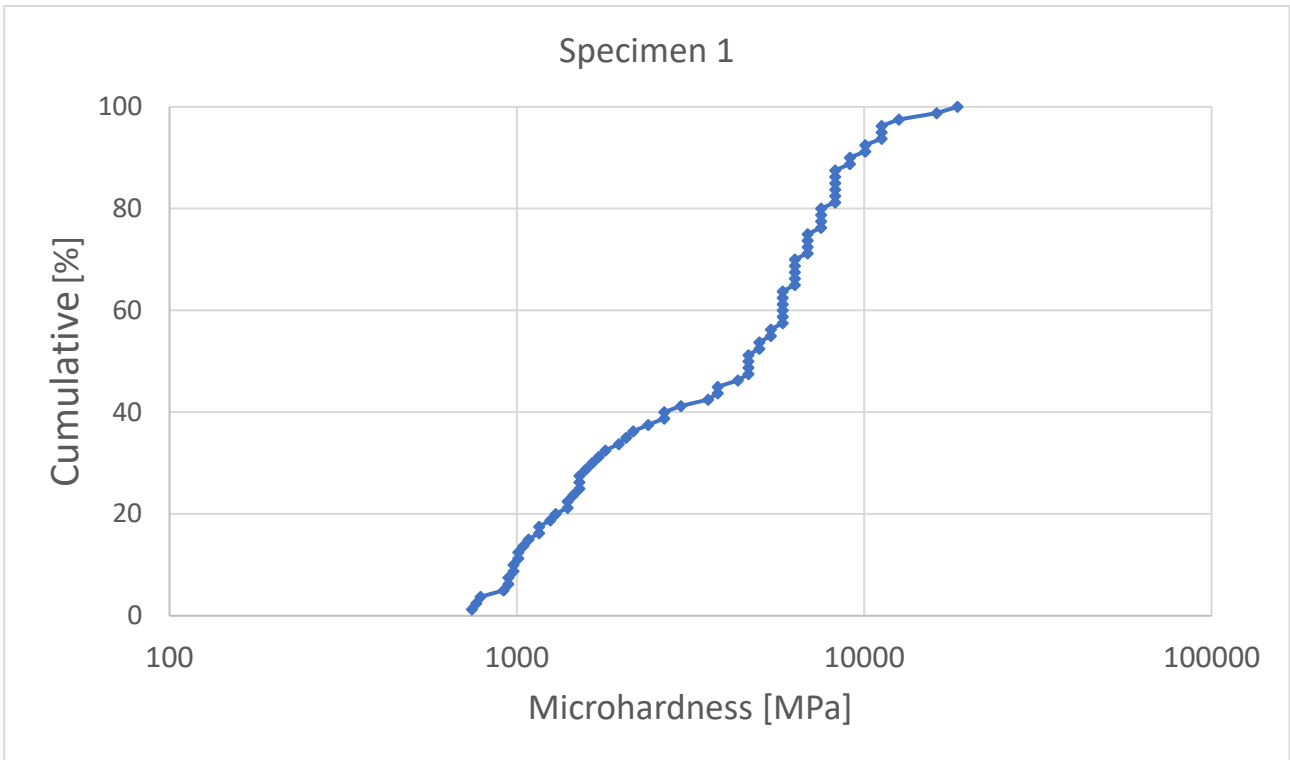
In this section are proposed the results achieved for all the specimens. They are for each specimen: a summarising table includes the test number, the dimension of the mark left and the relative Vickers hardness measurement, a graph with the representative distribution of the hardness values and a specimen picture.

Below are reported the results obtained for the Specimen 1, summarised in the Table 4.1, Graph 4.1, and Figure 4.7.

Table 4.1 - Microhardness measurements specimen 1

Specimen n. 1		
Test n°	d [ $\mu\text{m}$ ]	HV [MPa]
1	37	2654.38
2	50	1453.54
3	31	3781.31
4	69	763.25
5	68	785.87
6	51	1397.09
7	70	741.60
8	62	945.33
9	46	1717.32
10	61	976.58
11	45	1794.49
12	27	4984.69
13	28	4635.00
14	18	11215.56
15	51	1397.09
16	23	6869.26
17	26	5375.50
18	25	5814.14
19	22	7507.93
20	26	5375.50
21	28	4635.00
22	29	4320.86
23	54	1246.17
24	25	5814.14
25	21	8240.00
26	22	7507.93
27	18	11215.56
28	23	6869.26
29	19	10066.04
30	23	6869.26
31	24	6308.75
32	25	5814.14
33	23	6869.26
34	28	4635.00
35	31	3781.31
36	22	7507.93
37	24	6308.75
38	17	12573.84
39	22	7507.93
40	21	8240.00

Specimen n. 1		
Test n°	d [ $\mu\text{m}$ ]	HV [MPa]
41	20	9084.60
42	21	8240.00
43	39	2389.11
44	15	16150.40
45	25	5814.14
46	37	2654.38
47	24	6308.75
48	25	5814.14
49	28	4635.00
50	35	2966.40
51	24	6308.75
52	21	8240.00
53	21	8240.00
54	14	18540.00
55	25	5814.14
56	56	1158.75
57	32	3548.67
58	19	10066.04
59	18	11215.56
60	42	2060.00
61	21	8240.00
62	20	9084.60
63	41	2161.71
64	62	945.33
65	43	1965.30
66	53	1293.64
67	27	4984.69
68	49	1513.47
69	60	1009.40
70	24	6308.75
71	63	915.56
72	56	1158.75
73	58	1080.21
74	49	1513.47
75	61	976.58
76	47	1645.02
77	49	1513.47
78	59	1043.91
79	60	1009.40
80	48	1577.19



Graph 4.1 - Distribution of the hardness values specimen 1



Figure 4.7 - Specimen 1

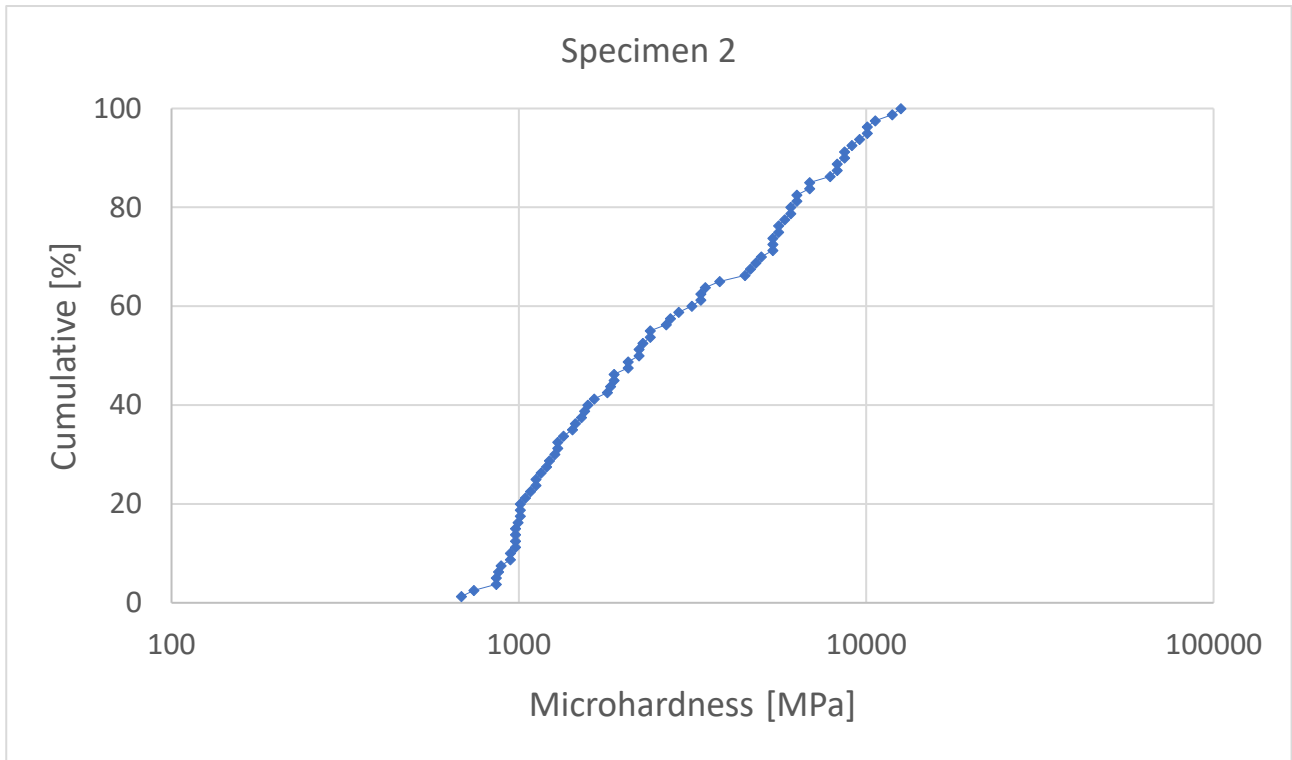
Below are reported the results obtained for the Specimen 2, summarised in the Table 4.2, Graph 4.2, and Figure 4.8.

Table 4.2 - Microhardness measurements specimen 2

Specimen n. 2		
Test n°	d [ $\mu\text{m}$ ]	HV [MPa]
1	31	3781.31
2	26	5375.50
3	20.5	8646.85
4	19	10066.04
5	28.5	4473.80
6	26	5375.50
7	18.5	10617.50
8	28	4635.00
9	27.5	4805.08
10	35.5	2883.43
11	24	6308.75
12	34	3143.46
13	24.5	6053.88
14	56	1158.75
15	57	1118.45
16	47	1645.02
17	64	887.17
18	65	860.08
19	73	681.90
20	61	976.58
21	61	976.58
22	59	1043.91
23	65	860.08
24	36.5	2727.60
25	54.5	1223.41
26	60.5	992.78
27	58	1080.21
28	62	945.33
29	40.5	2215.42
30	44.5	1835.04
31	52	1343.88
32	48.5	1544.84
33	49	1513.47
34	23	6869.26
35	26	5375.50
36	24.5	6053.88
37	21	8240.00
38	23	6869.26
39	24	6308.75
40	25.5	5588.37

Specimen n. 2		
Test n°	d [ $\mu\text{m}$ ]	HV [MPa]
41	53	1293.64
42	21.5	7861.20
43	33	3336.86
44	32.5	3440.32
45	42	2060.00
46	37	2654.38
47	44	1876.98
48	40	2271.15
49	60	1009.40
50	21	8240.00
51	17	12573.84
52	60	1009.40
53	17.5	11865.60
54	62	945.33
55	70	741.60
56	53	1293.64
57	20	9084.60
58	20.5	8646.85
59	27	4984.69
60	25.5	5588.37
61	19.5	9556.45
62	40.5	2215.42
63	19	10066.04
64	42	2060.00
65	25	5814.14
66	60	1009.40
67	57	1118.45
68	48	1577.19
69	53.5	1269.57
70	33	3336.86
71	44	1876.98
72	50.5	1424.90
73	55	1201.27
74	61	976.58
75	39	2389.11
76	64.5	873.47
77	39	2389.11
78	45	1794.49
79	50	1453.54
80	61	976.58





Graph 4.2 - Distribution of the hardness values specimen 2

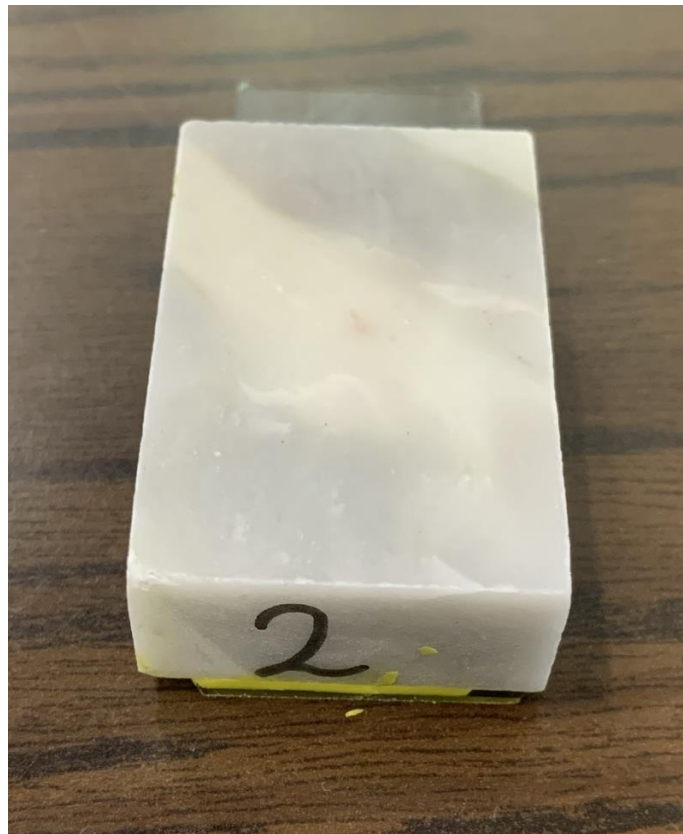


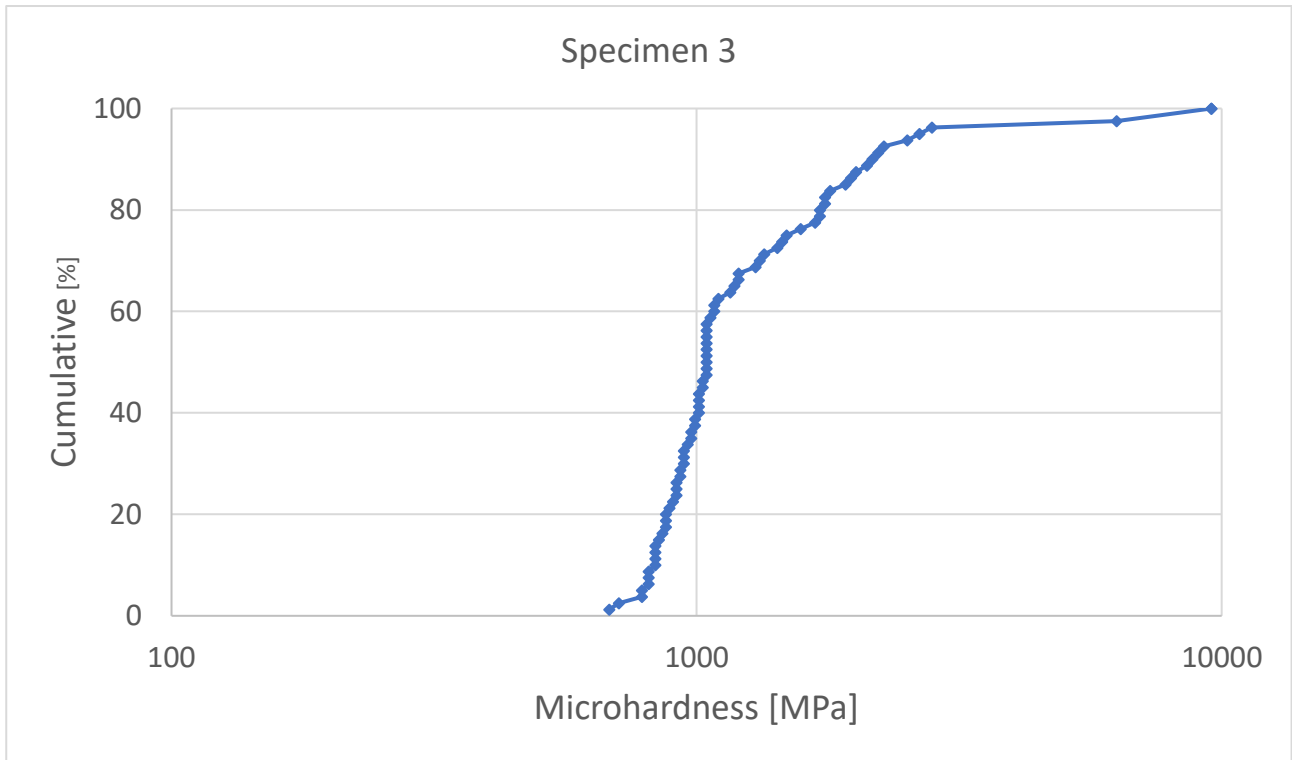
Figure 4.8 - Specimen 2

Below are reported the results obtained for the Specimen 3, summarised in the Table 4.3, Graph 4.3, and Figure 4.9.

Table 4.3 - Microhardness measurements specimen 3

Specimen n. 3		
Test n°	d [ $\mu\text{m}$ ]	HV [MPa]
1	59	1043.91
2	64	887.17
3	63	915.56
4	58	1080.21
5	63	915.56
6	37	2654.38
7	59	1043.91
8	52.5	1318.40
9	68	785.87
10	59	1043.91
11	65.5	847.00
12	59	1043.91
13	19.5	9556.45
14	71.5	710.81
15	60	1009.40
16	46	1717.32
17	46.5	1680.58
18	67	809.50
19	58.5	1061.83
20	59	1043.91
21	41	2161.71
22	62	945.33
23	42.5	2011.81
24	63	915.56
25	62.5	930.26
26	66	834.21
27	19.5	9556.45
28	24	6308.75
29	62	945.33
30	55	1201.27
31	48	1577.19
32	45	1794.49
33	43	1965.30
34	52	1343.88
35	61	976.58
36	59	1043.91
37	58	1080.21
38	53	1293.64
39	67	809.50
40	64.5	873.47

Specimen n. 3		
Test n°	d [ $\mu\text{m}$ ]	HV [MPa]
41	60.5	992.78
42	62.5	930.26
43	59	1043.91
44	43.5	1920.38
45	57.5	1099.08
46	60.5	992.78
47	64.5	873.47
48	64.5	873.47
49	50.5	1424.90
50	68	785.87
51	59	1043.91
52	50	1453.54
53	61.5	960.76
54	56	1158.75
55	73	681.90
56	61	976.58
57	40.5	2215.42
58	59.5	1026.44
59	38	2516.51
60	66	834.21
61	60	1009.40
62	59.5	1026.44
63	65	860.08
64	62	945.33
65	67	809.50
66	41.5	2109.94
67	66	834.21
68	59	1043.91
69	55	1201.27
70	60	1009.40
71	40	2271.15
72	55.5	1179.72
73	36	2803.89
74	45.5	1755.27
75	60	1009.40
76	66	834.21
77	49.5	1483.05
78	63.5	901.19
79	45.5	1755.27
80	46	1717.32



Graph 4.3 - Distribution of the hardness values specimen 3

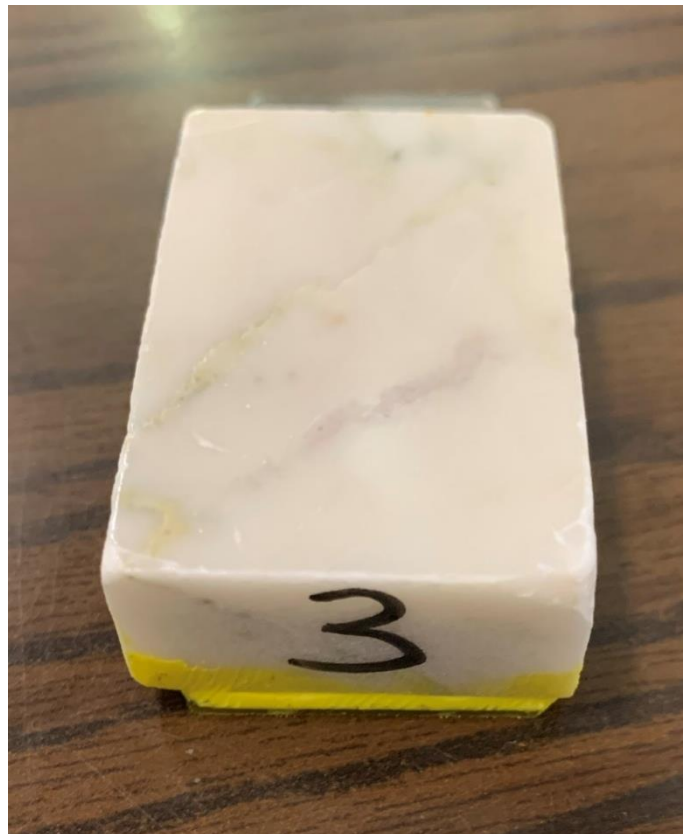


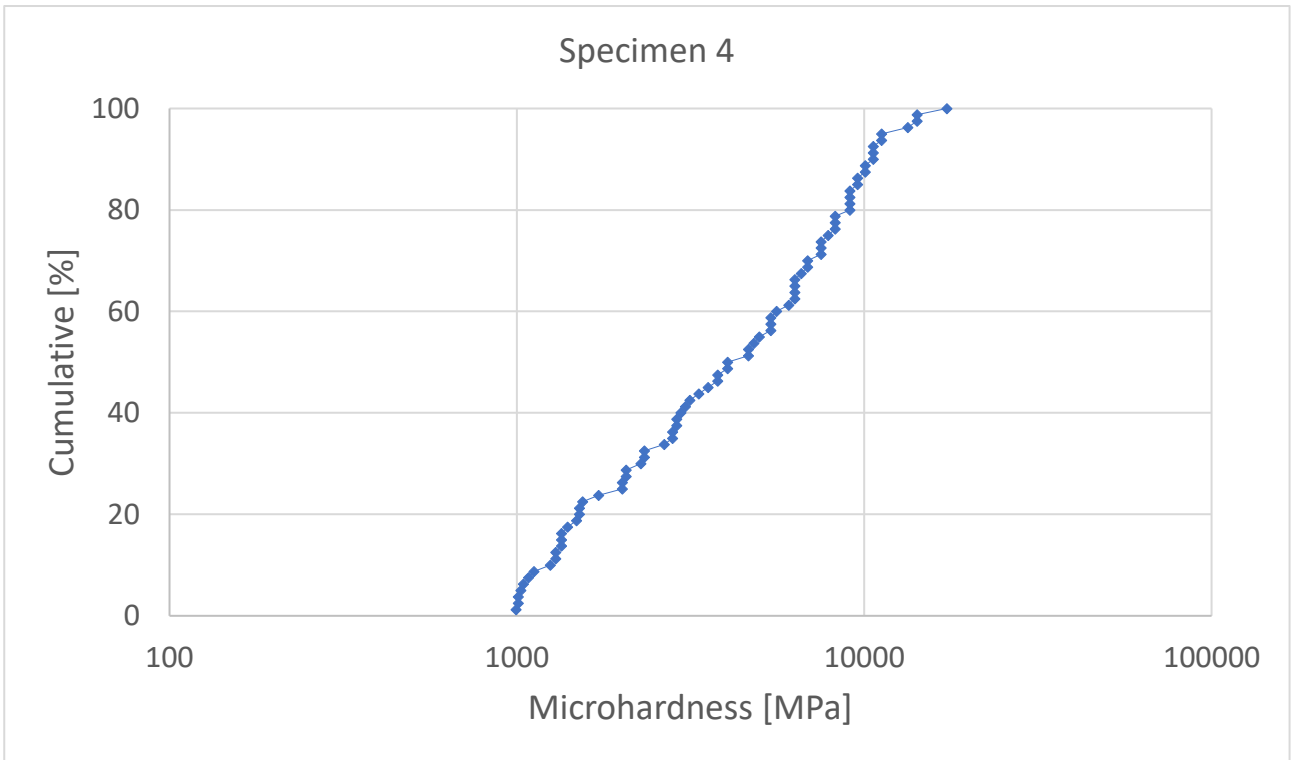
Figure 4.9 - Specimen 3

Below are reported the results obtained for the Specimen 4, summarised in the Table 4.4, Graph 4.4, and Figure 4.10.

Table 4.4 - Microhardness measurements specimen 4

Specimen n. 4		
Test n°	d [ $\mu\text{m}$ ]	HV [MPa]
1	18.5	10617.50
2	24	6308.75
3	34	3143.46
4	18.5	10617.50
5	18	11215.56
6	19.5	9556.45
7	31	3781.31
8	31	3781.31
9	28	4635.00
10	39.5	2329.01
11	21	8240.00
12	19	10066.04
13	24	6308.75
14	27.5	4805.08
15	22	7507.93
16	49	1513.47
17	58	1080.21
18	30	4037.60
19	46	1717.32
20	36	2803.89
21	35.5	2883.43
22	25.5	5588.37
23	16	14194.69
24	40	2271.15
25	26	5375.50
26	24	6308.75
27	37	2654.38
28	21	8240.00
29	59.5	1026.44
30	32	3548.67
31	60	1009.40
32	52	1343.88
33	22	7507.93
34	33	3336.86
35	52	1343.88
36	51	1397.09
37	49.5	1483.05
38	20	9084.60
39	19	10066.04
40	60.5	992.78

Specimen n. 4		
Test n°	d [ $\mu\text{m}$ ]	HV [MPa]
41	42	2060.00
42	20	9084.60
43	27	4984.69
44	59	1043.91
45	53	1293.64
46	24.5	6053.88
47	42	2060.00
48	60	1009.40
49	49	1513.47
50	57	1118.45
51	21	8240.00
52	20	9084.60
53	26	5375.50
54	23	6869.26
55	42.5	2011.81
56	30	4037.60
57	34.5	3053.01
58	19.5	9556.45
59	22	7507.93
60	14.5	17283.42
61	24	6308.75
62	23.5	6580.06
63	16	14194.69
64	16.5	13347.44
65	35.5	2883.43
66	18	11215.56
67	26	5375.50
68	20	9084.60
69	18.5	10617.50
70	28	4635.00
71	21.5	7861.20
72	42.5	2011.81
73	52	1343.88
74	54	1246.17
75	35	2966.40
76	23	6869.26
77	36	2803.89
78	39.5	2329.01
79	48.5	1544.84
80	53	1293.64



Graph 4.4 - Distribution of the hardness values specimen 4



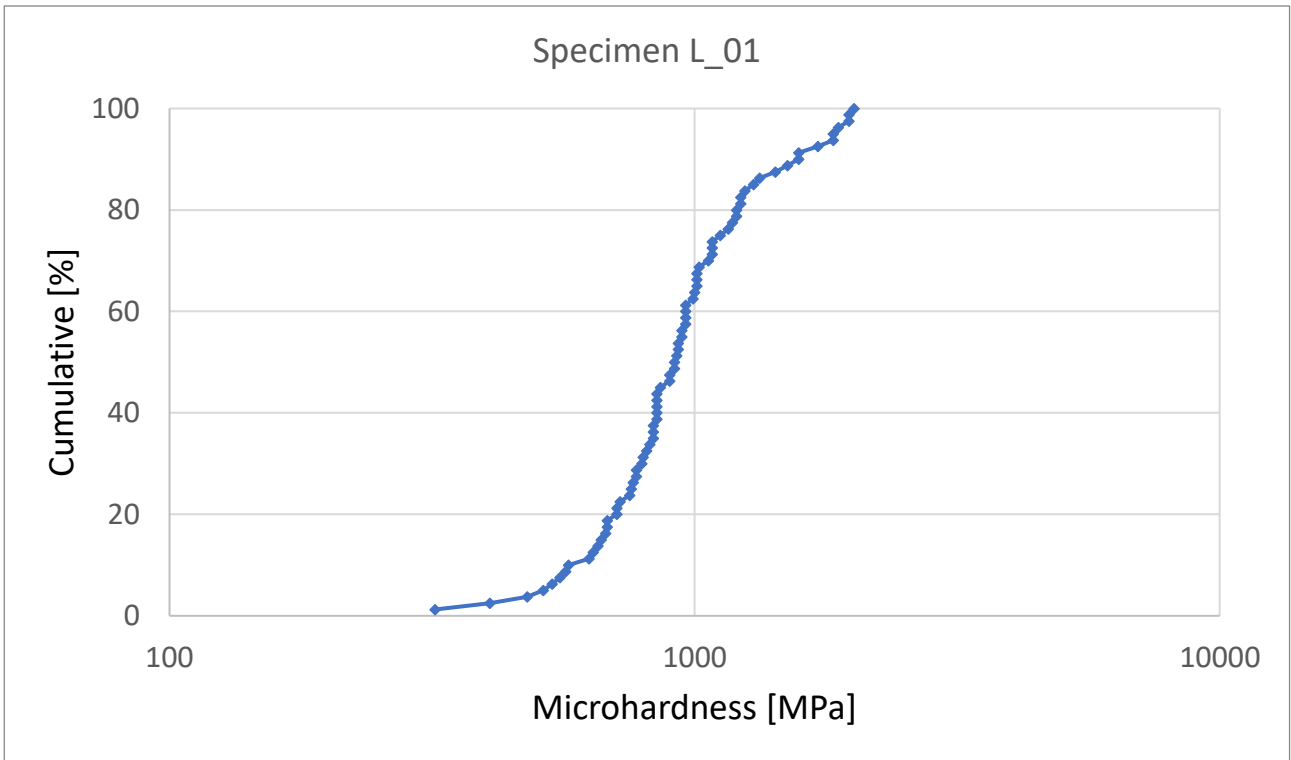
Figure 4.10 - Specimen 4

Below are reported the results obtained for the Specimen L\_01, summarised in the Table 4.5, Graph 4.5, and Figure 4.11.

Table 4.5 - Microhardness measurements specimen L\_01

Specimen n. L_01		
Test n°	d [ $\mu$ m]	HV [MPa]
1	48	1577.19
2	43	1965.30
3	60	1009.40
4	58	1080.21
5	73	681.90
6	63	915.56
7	68.5	774.44
8	61.5	960.76
9	50.5	1424.90
10	49.2	1501.19
11	71.5	710.81
12	44.5	1835.04
13	55.5	1179.72
14	57	1118.45
15	53	1293.64
16	55	1201.27
17	58	1080.21
18	68.5	774.43
19	54	1246.17
20	44	1876.98
21	54.5	1223.41
22	66	834.21
23	67.7	792.85
24	69.5	752.31
25	60	1009.4
26	52.3	1328.50
27	69.3	756.66
28	67.5	797.55
29	75.3	640.88
30	66	834.21
31	46	1717.32
32	59.7	1019.57
33	56	1158.75
34	61.5	960.76
35	62.5	930.26
36	63.7	895.54
37	62	945.33
38	48	1577.19
39	65.5	847.00
40	58	1080.21

Specimen n. L_01		
Test n°	d [ $\mu$ m]	HV [MPa]
41	65	860.08
42	60.3	999.38
43	66	834.21
44	55	1201.27
45	65.5	847.00
46	66.5	821.72
47	71	720.86
48	106.5	320.30
49	62.7	924.34
50	73.3	676.33
51	76	629.13
52	65.5	847.00
53	69	763.25
54	54.5	1223.41
55	65.5	847.00
56	61.5	960.76
57	62	945.33
58	58.5	1061.83
59	74.5	654.72
60	67	809.50
61	63	915.56
62	62.5	930.26
63	43	1965.30
64	81	553.85
65	60.5	992.78
66	80	567.79
67	71.5	710.81
68	73	681.90
69	82.4	535.19
70	79.5	574.95
71	84	515.00
72	94.5	406.91
73	42.5	2011.81
74	44.5	1835.04
75	60	1009.40
76	65.5	847.00
77	63.7	895.54
78	74	663.59
79	61.5	960.76
80	87	480.10



Graph 4.5 - Distribution of the hardness values specimen L\_01



Figure 4.11 - Specimen L\_01

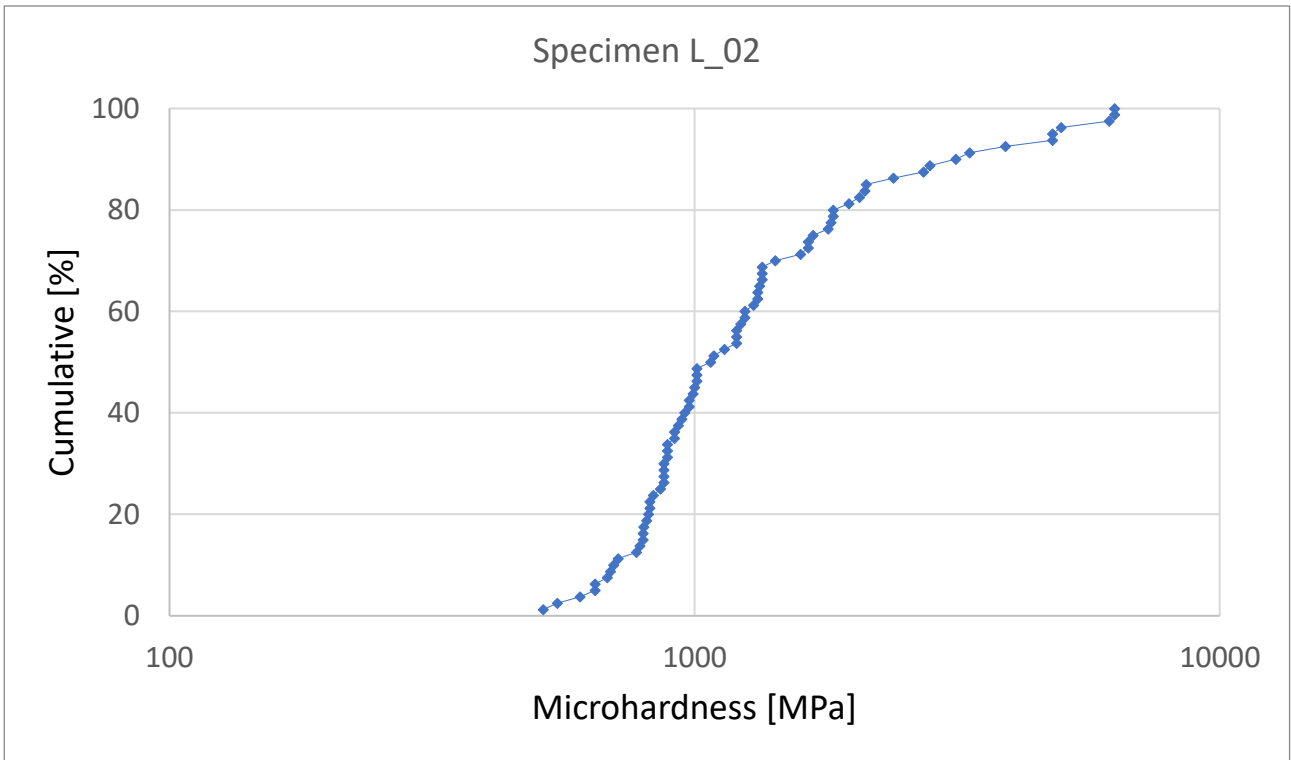
Below are reported the results obtained for the Specimen L\_02, summarised in the Table 4.6, Graph 4.6, and Figure 4.12.

Table 4.6 - Microhardness measurements specimen L\_02

Specimen n. L_02		
Test n°	d [ $\mu$ m]	HV [MPa]
1	47	1645.02
2	60	1009.40
3	44.7	1818.66
4	60	1009.40
5	62	945.33
6	41.5	2109.934
7	39	2389.112
8	58.2	1072.803
9	64.5	873.4667
10	24	6308.75
11	61	976.58
12	75	646.02
13	71.3	714.80
14	27.5	4805.08
15	60.3	999.38
16	77.5	605.01
17	44.5	1835.04
18	72	700.97
19	52.3	1328.50
20	34	3143.46
21	44.5	1835.04
22	52	1343.88
23	64.5	873.47
24	62.5	930.26
25	50.5	1424.90
26	60.5	992.78
27	68.5	774.43
28	66.5	821.72
29	43	1965.30
30	63	915.56
31	60	1009.40
32	66.7	816.80
33	47.8	1590.41
34	63	915.56
35	67.4	799.92
36	47	1645.01
37	56.5	1138.33
38	72.5	691.34
39	52.5	1318.40
40	61	976.58

Specimen n. L_02		
Test n°	d [ $\mu$ m]	HV [MPa]
41	67.5	797.55
42	55	1201.27
43	66	834.21
44	84	515.00
45	64.5	873.47
46	61.6	957.65
47	65	860.08
48	64	887.17
49	73	681.90
50	55	1201.27
51	30.5	3906.31
52	55	1201.27
53	36	2803.90
54	27.5	4805.08
55	36.5	2727.60
56	41.4	2120.14
57	52	1343.88
58	46.5	1680.58
59	75	646.02
60	57.8	1087.70
61	52.5	1318.40
62	64	887.17
63	67	809.50
64	27	4984.69
65	54.5	1223.41
66	53	1293.64
67	54	1246.17
68	24.3	6153.94
69	52	1343.88
70	64.5	873.47
71	33	3336.86
72	66.5	821.72
73	54	1246.17
74	81.5	547.08
75	45	1794.50
76	42	2060.00
77	64	887.17
78	24	6308.75
79	67.5	797.56
80	68	785.87





Graph 4.6 - Distribution of the hardness values specimen L\_02



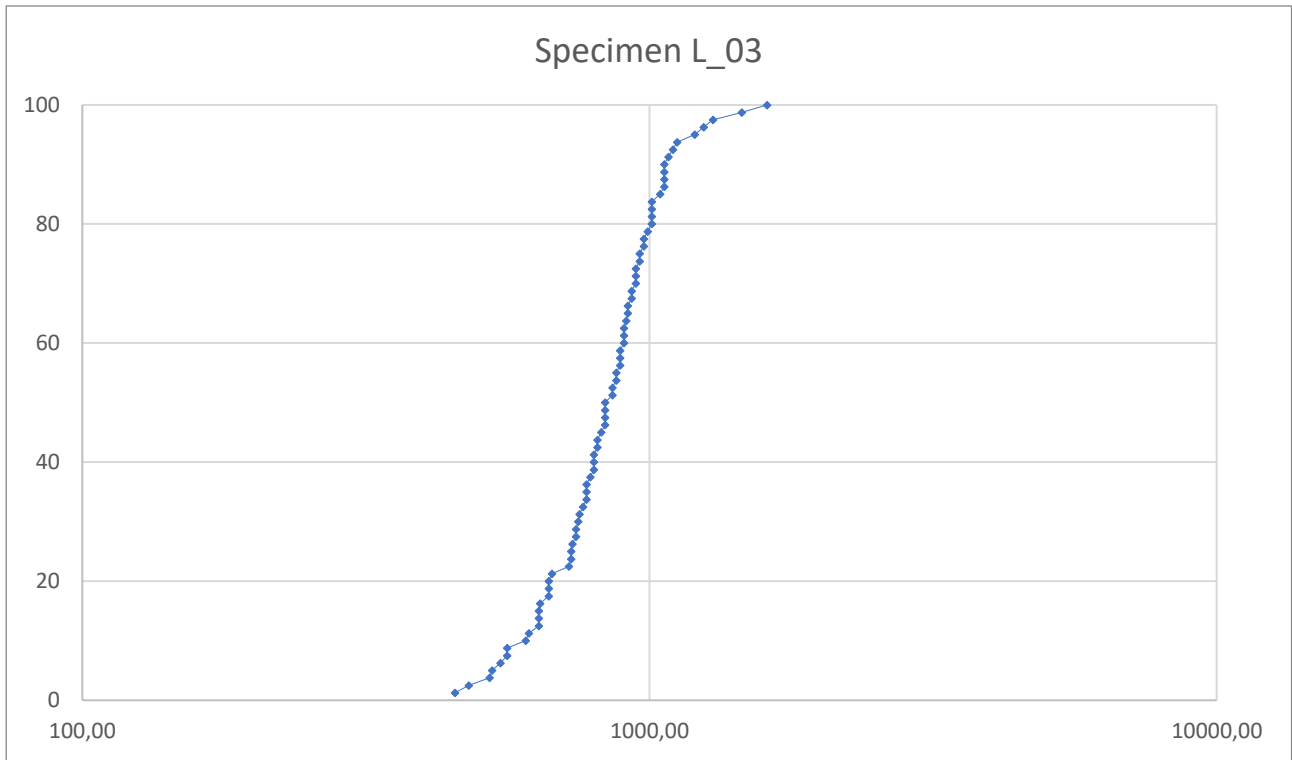
Figure 4.12 - Specimen L\_02

Below are reported the results obtained for the Specimen L\_03, summarised in the Table 4.7, Graph 4.7, and Figure 4.13.

Table 4.7 - Microhardness measurements specimen L\_03

Specimen n. L_03		
Test n°	d [ $\mu$ m]	HV [MPa]
1	47	1645.02
2	60	1009.40
3	44.7	1818.66
4	60	1009.40
5	62	945.33
6	41.5	2109.94
7	39	2389.11
8	58.2	1072.80
9	64.5	873.47
10	24	6308.75
11	61	976.58
12	75	646.02
13	71.3	714.80
14	27.5	4805.08
15	60.3	999.38
16	77.5	605.01
17	44.5	1835.04
18	72	700.97
19	52.3	1328.50
20	34	3143.46
21	44.5	1835.04
22	52	1343.88
23	64.5	873.47
24	62.5	930.26
25	50.5	1424.90
26	60.5	992.78
27	68.5	774.43
28	66.5	821.72
29	43	1965.30
30	63	915.56
31	60	1009.40
32	66.7	816.80
33	47.8	1590.41
34	63	915.56
35	67.4	799.92
36	47	1645.01
37	56.5	1138.33
38	72.5	691.34
39	52.5	1318.40
40	61	976.58

Specimen n. L_03		
Test n°	d [ $\mu$ m]	HV [MPa]
41	64.5	873.47
42	65	860.08
43	60.5	992.79
44	67.5	797.55
45	60	1009.40
46	67.5	797.55
47	73.5	672.65
48	68	785.87
49	75.5	637.49
50	66	834.21
51	70	741.60
52	80.5	560.76
53	66	834.21
54	63	915.56
55	83	527.48
56	64	887.17
57	58.5	1061.83
58	70.7	726.99
59	67	809.50
60	80.5	560.76
61	47.5	1610.57
62	77	612.89
63	68.5	774.43
64	75.3	640.88
65	65	860.08
66	58.5	1061.83
67	63.5	901.19
68	81.6	545.74
69	60	1009.40
70	50	1453.54
71	58.5	1061.83
72	64.5	873.47
73	62	945.33
74	61	976.58
75	54	1246.17
76	64	887.17
77	68.5	774.43
78	66.5	821.72
79	63.2	909.71
80	87	480.10



Graph 4.7 - Distribution of the hardness values specimen L\_03



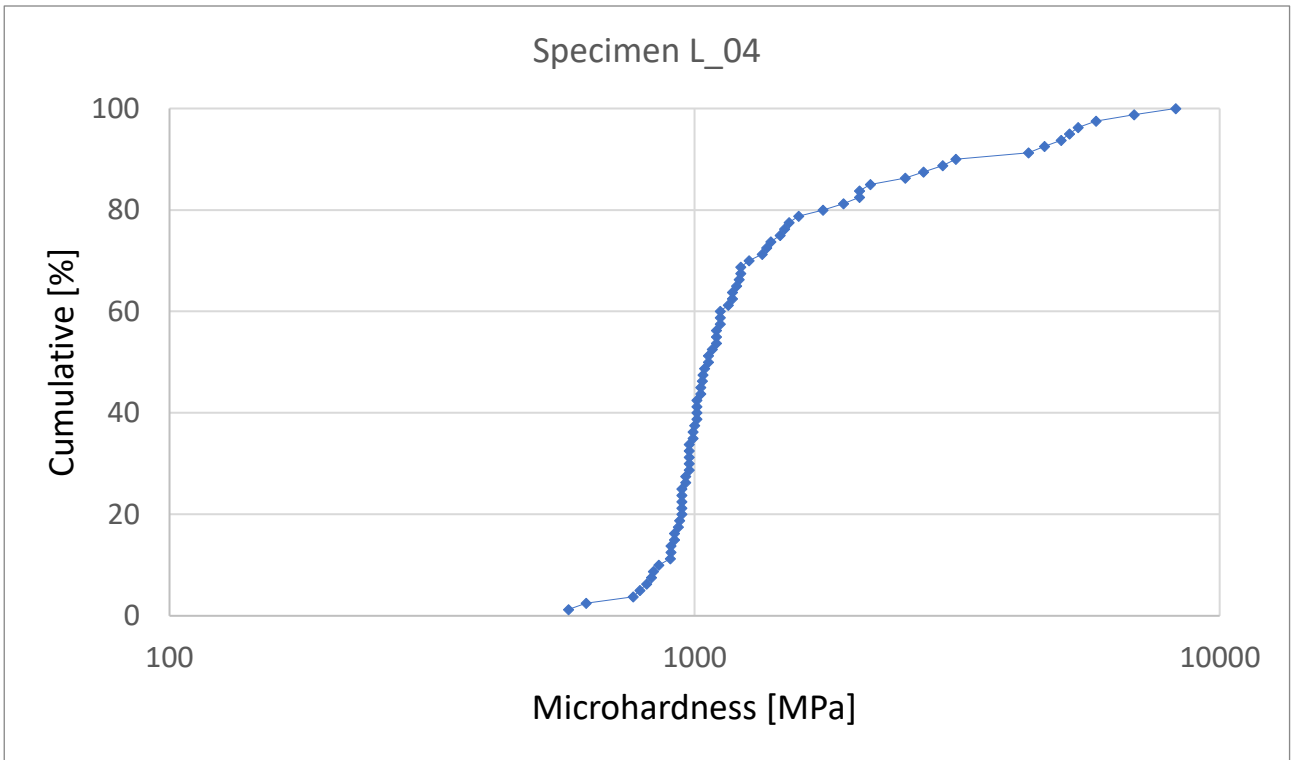
Figure 4.13 - Specimen L\_03

Below are reported the results obtained for the Specimen L\_04, summarised in the Table 4.8, Graph 4.8, and Figure 4.14.

Table 4.8 - Microhardness measurements specimen L\_04

Specimen n. L_04		
Test n°	d [ $\mu\text{m}$ ]	HV [MPa]
1	62	945.33
2	60	1009.40
3	54.5	1223.41
4	62	945.33
5	62	945.33
6	41	2161.71
7	76.5	620.93
8	67	809.50
9	79.5	574.95
10	43.5	1920.38
11	61.5	960.76
12	27	4984.69
13	28	4635.00
14	69	763.25
15	62.5	930.26
16	58.5	1061.83
17	62	945.33
18	60.5	992.78
19	57.5	1099.08
20	51	1397.09
21	61	976.58
22	57	1118.50
23	42	2060.00
24	48	1577.19
25	58	1080.21
26	59.5	1026.44
27	68	785.87
28	57.5	1099.08
29	66.3	826.68
30	63.6	898.36
31	50	1453.54
32	55	1201.27
33	60.5	992.78
34	35	2966.40
35	63.5	901.19
36	38	2516.51
37	53.5	1269.58
38	58.5	1061.83
39	63	915.56
40	26.5	5174.57

Specimen n. L_04		
Test n°	d [ $\mu\text{m}$ ]	HV [MPa]
41	25	5814.14
42	42	2060.00
43	56	1158.75
44	60	1009.40
45	63.5	901.19
46	60	1009.40
47	66	834.22
48	34	3143.46
49	61	976.58
50	60.3	999.38
51	49	1513.47
52	61	976.58
53	59	1043.91
54	55.5	1179.72
55	61.5	960.76
56	62.3	936.25
57	62	945.33
58	54.7	1214.48
59	57	1118.45
60	29	4320.86
61	23	6869.26
62	49.5	1483.05
63	54.5	1223.41
64	21	8240.00
65	26	5375.50
66	59.5	1026.44
67	51.5	1370.10
68	55.5	1179.72
69	36.5	2727.60
70	57	1118.45
71	45.5	1755.27
72	59.3	1033.37
73	61	976.58
74	60	1009.40
75	59.2	1036.87
76	63	915.56
77	65.2	854.81
78	52	1343.88
79	61	976.58
80	57.5	1099.08



Graph 4.8 - Distribution of the hardness values specimen L\_04

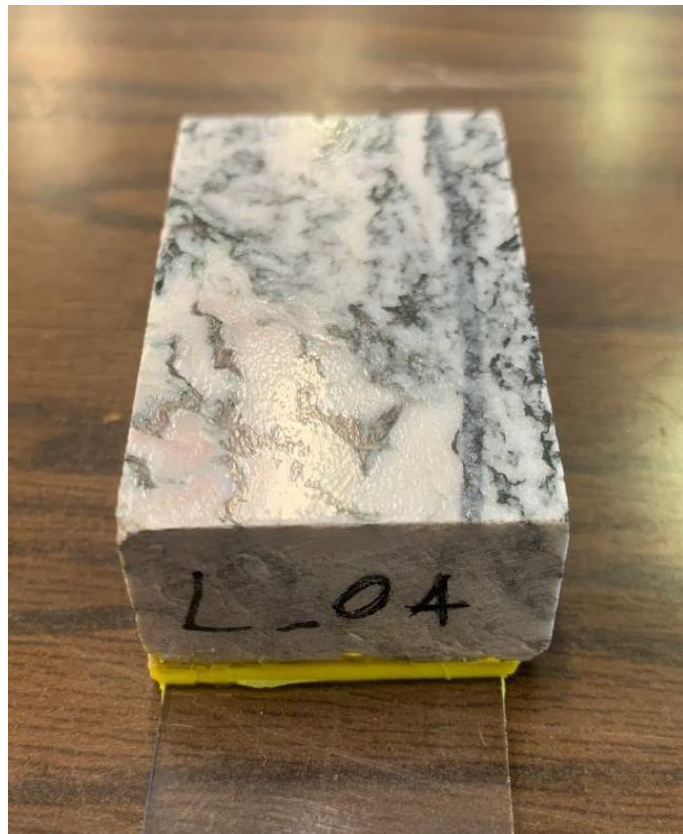


Figure 4.14 - Specimen L\_04

The results achieved for the four white marble specimens, i.e., specimen 1, 2, 3, and 4, confirm the expected results: in fact, they exhibit relatively high micro-hardness values if compared to those characteristics of marble, which vary from 1200 MPa to 1600 MPa (Kaklis et al., 2007). This behaviour is due to high impurities such as quartz, mica, and other components. As it can be seen, instead, in specimen 3, only 22% has hardness greater than 1600MPa because the specimen analysed, Figure 4.9, has only a tiny vein with the inclusion of quartz and other impurities. In this area, the indenter has left a minor mark than those left in calcium carbonate.

However, the results obtained justify the company's choice not to use tungsten carbide tools in the chain saw machine since the Vickers micro-hardness of this chemical compound is between 10000 MPa and 14000 MPa, and in various tests carried out, this value was overcome. Then, the company's choice went on the use of polycrystalline diamond tools. In Politecnico's laboratory, various tests were carried out to evaluate the micro-hardness of the polycrystalline diamond tools, but the surface to be studied is made up of synthetic diamonds, and the Vickers indenter is unable to leave a visible imprint, or if it leaves a mark, with the x50 optics installed in the microdurimeter, it was impossible to detect. For this reason, Akaishi et al. (1991) suggests a Vickers hardness of the polycrystalline diamond that reach  $55000 \pm 500$  MPa with 2 kg of load.

Specimen 1: 71% > 1600 MPa, 10% > 10000 MPa

Specimen 2: 60% > 1600 MPa, 5% > 10000 MPa

Specimen 3: 23% > 1600 MPa, 0% > 10000 MPa

Specimen 4: 77% > 1600 MPa, 12% > 10000 MPa

The results obtained for the green-red marble confirm those that were achieved from a petrographic analysis. Two specimens, L\_01 and L\_03, show a typical range of micro-hardness values comparable to marble. In the L\_02 and L\_04 specimens, on the other hand, more than 20% of the micro-hardness values are greater than 1600 MPa, and this is due, as can be seen from the thin sections previously described, to the impurities of quartz, mica, and chlorite.

L\_01 and L\_03 behave like the marble; they are softer than the other sample analysed. A similar thin section was studied in Sample 2, proposed on page 45.

Specimen L\_01: 7% > 1600 MPa

Specimen L\_03: 1% > 1600 MPa

L\_02 and L\_04 instead are harder due to the inclusions of quartz, and other minerals. A similar thin section was studied on page 44.

Specimen L\_02: 27% > 1600 MPa

Specimen L\_04: 20% > 1600 MPa

### 4.3.CERCHAR abrasivity test

The CERCHAR abrasivity test is one of the most common procedures for laboratory measurement of the abrasiveness of rocks (Hamzaban et al., 2018). The method was first developed in the 1980s by the Laboratoire du Center d'Etude et Recherches des Charbonnages (CERCHAR) de France for coal mining purposes (Cerchar, 1986).

Abrasion can be defined as the wear of particles and material from the solid surface. The test allows determining an index called the CERCHAR Abrasiveness Index (CAI), which evaluate the wear of a given equipment in various applications such as mines, tunnels, and drilling.

Two types of test devices are in use today: the original "Cerchar apparatus", according to the layout presented by the Cerchar's recommendations (1986), and the "West apparatus", according to the test device illustrated by West (1989). The original design includes a vice that holds the rock sample and a test lever directly connected to the steel pin. The steel pin must be manufactured of a standard chrome vanadium alloy cold work tool steel, tempered to a steel graded 55 Rock-well hardness scale (HRC). The steel pin is loaded with a static force of 70 N and scratched on the rock surface by moving the lever at 10 mm/s of speed. The "West apparatus" also has a vice and a steel pin loaded with 70 N, but the test speed is slower compared to the "Cerchar apparatus", taking 10 s for the scratch path of 10 mm (Alber et al., 2013). The different speed of execution of the two tests is due to the further movement control that moves the rock sample under the pin.

In both configurations, the wear surface of the steel pin is measured under a microscope with an accuracy of 0.01 mm (Alber et al., 2013).

For each measurement of the wear flat,  $d$ , the CAI is calculated by the following formula (Alber et al., 2013):

$$CAI = d * 10$$

where  $d$  is the wear tip surface.

It is evident that the steel hardness directly influences the results of the test. However, this aspect can be exceeded by using the formula proposed by Jacobs and Hagan (2009), which allows converting the CAI calculated with steel hardness different to  $HRC_{(55 \pm 1)}$  into the standard CAI:

$$CAI_{(55)} = \frac{0.415 * CAI_{(x)}}{1 - 0.0107 * x}$$

where  $x$  is the value of the hardness in units of Rock-well hardness, and  $CAI_{(x)}$  is measured as the value of CAI using a stylus having a hardness of  $HRC_{(x)}$ .



The tests at Politecnico di Torino were performed with the West apparatus, a schematic representation is proposed in the Figure 4.15, and with HRC<sub>(64.5)</sub> steel pins.

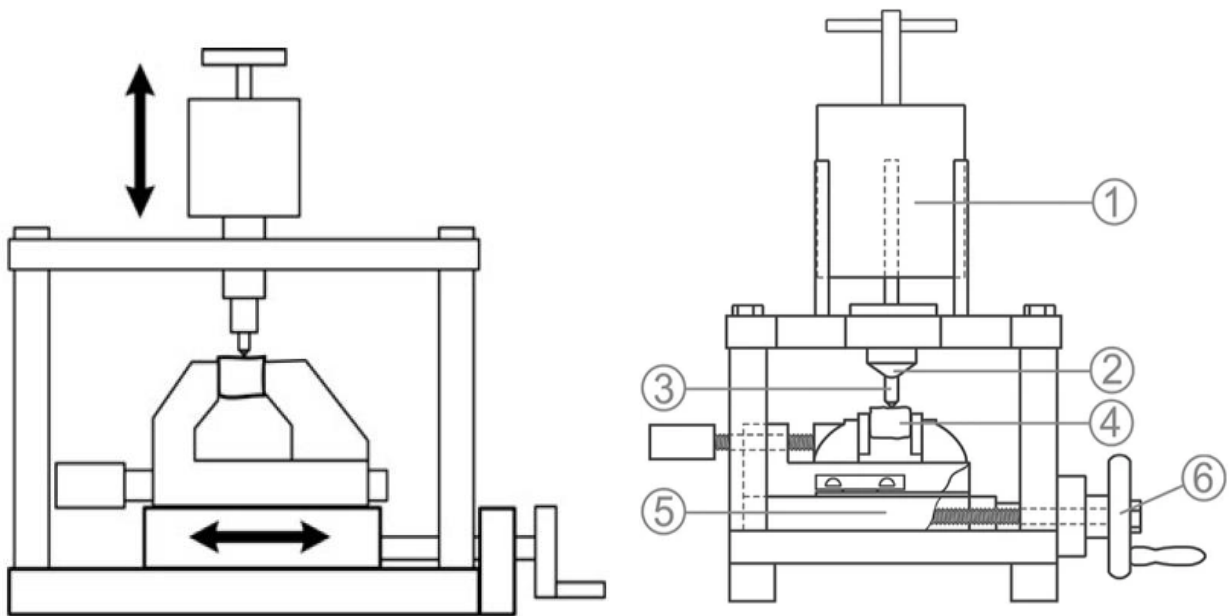


Figure 4.15 - Testing device setup according to West apparatus (Rostami et al., 2013)  
 1 mass, 2 pin guide, 3 steel pin, 4 specimen, 5 vice, 6 hand lever

The testing procedure is quite simple:

1. Before starting the tests, the steel pin should be inspected under a microscope to control that the stylus is sharpened with a 90-degree angle tip.
2. The sample should be firmly clamped, to avoid any lateral movement in the vice while observing the desired scratching direction. The rock surface should be horizontal.
3. The stylus should be vertical and perpendicular to the rock surface.
4. Once the pin has been placed, the dead load of 70N is arranged on the top of the pin and carefully lowered.
5. The scratching test is ready to begin, and five times the crank has to be turned, in the wanted direction, to move the rock sample of exactly 10.0 mm.
6. After the test, the pin is carefully lifted from the rock surface; the stylus is removed and positioned on the optic microscope to measure the tip flat wear. The camera embedded in the microscope took a photograph of the pin's point so that the tip flat wear could be compared to the original length of the pin. Every pin was photographed two times so that the flat wear could be measured in two perpendiculars directions, yielding an average value.

7. These photographs were then moved on a computer, and, thanks to the AutoCAD software, the flat wear was measured, comparing the length of the segments representing the flat wear with the micrometric scale.

Figure 4.16 shows on the left the correct width measurement of the flat wear suffered by the stylus for the evaluation of the CAI; instead, on the right is presented a wrong measure because it is also included the length of a burr.

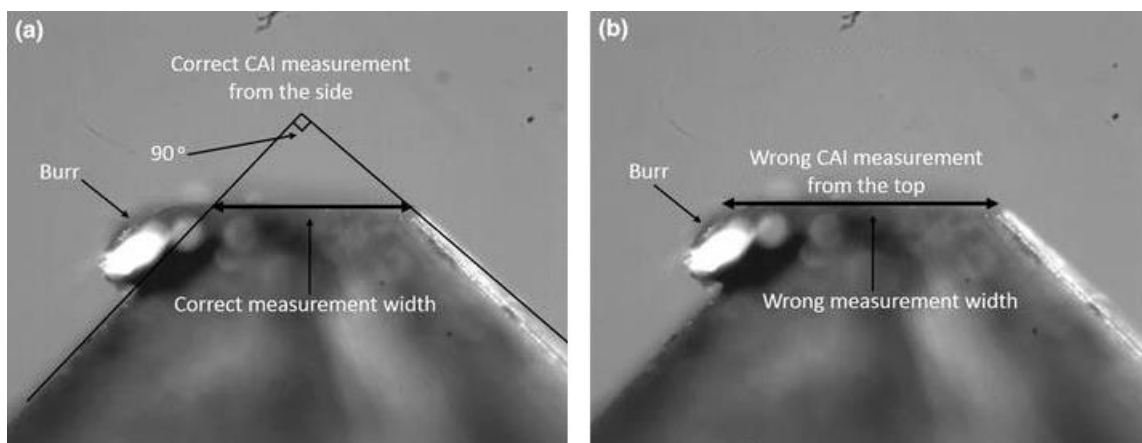


Figure 4.16 - Flat wear measuring (Rostami et al., 2005)

#### 4.3.1. Results

The data achieved during the evaluation of the CERCHAR Abrasivity Index can be observed in the following tables. In particular, from Table 4.9 to Table 4.15, for Specimen A, and from Table 4.26 to Table 4.32, for Specimen B, the results of the tests are shown. Those results are presented starting from the measurement of the flat wear of the stylus, passing through the calculation of the  $CAI_{(64.5)}$  and converting it into the  $CAI_{(55)}$  classification. In Figure 4.15 and Figure 4.16 are proposed a picture where Specimen A and Specimen B are shown before and after the scratches. For each stylus employed to characterise the two specimens, from Table 4.16 to Table 4.25 for Specimen A and from Table 4.33 to Table 4.42 for Specimen B, a representative table is presented.

Table 4.9 - Specimen A,  $CAI_{(64.5)}$  [0°]

Specimen A	Test	d1 [0°]	d2 [0°]	Average CAD unit	Average [mm]	$CAI_{(64.5)}$
	1	9.93	12.71	11.32	0.24	2.38
	2	10.83	12.73	11.78	0.25	2.47
	3	8.75	8.75	8.75	0.18	1.84
	4	10.77	10.77	10.77	0.23	2.26
	5	8.88	10.86	9.87	0.21	2.07
	6	8.42	11.37	9.90	0.21	2.08
	7	11.33	11.33	11.33	0.24	2.38
	8	6.81	6.81	6.81	0.14	1.43
	9	10.35	10.35	10.35	0.22	2.17
	10	7.76	7.76	7.76	0.16	1.63

Table 4.10 - Specimen A,  $CAI_{(64.5)}$  [90°]

Specimen A	Test	d1 [90°]	d2 [90°]	Average CAD unit	Average [mm]	$CAI_{(64.5)}$
	1	10.19	10.19	10.19	0.21	2.14
	2	12.96	12.96	12.96	0.27	2.72
	3	6.89	6.89	6.89	0.15	1.45
	4	10.97	10.97	10.97	0.23	2.30
	5	9.25	11.79	10.52	0.22	2.21
	6	8.31	8.31	8.31	0.18	1.75
	7	12.29	12.29	12.29	0.26	2.58
	8	7.98	7.98	7.98	0.17	1.68
	9	10.59	10.59	10.59	0.22	2.22
	10	7.52	7.52	7.52	0.16	1.58

Table 4.11 -  $CAI_{(64.5)}$  average Specimen A

Specimen A	Test	$CAI_{(64.5)}$ Average	Stand. Dev.
	1	2.26	0.17
	2	2.60	0.18
	3	1.64	0.28
	4	2.28	0.03
	5	2.14	0.10
	6	1.91	0.24
	7	2.48	0.14
	8	1.55	0.17
	9	2.20	0.04
	10	1.60	0.04

Table 4.12 -  $CAI_{(55)}$  Specimen A

$CAI_{(55)}$	CAI Classification
3.03	High
3.48	High
2.20	Medium
3.06	High
2.87	Medium
2.56	Medium
3.32	High
2.08	Medium
2.94	Medium
2.15	Medium

Table 4.13 -  $CAI_{(64.5)}$  average Specimen A

$CAI_{(64.5)}$ Average	Stand. Dev.
2.07	0.37

Table 4.14 -  $CAI_{(55)}$  average Specimen A

$CAI_{(55)}$ Average	Stand. Dev.	CAI Classification
2.77	0.50	Medium

Table 4.15 -  $CAI_{(55)}$  classification

$CAI_{(55)}$	Abrasivity scale
< 0.5	Extremely low
0.5 – 0.99	Very low
1.0 – 1.99	Low
<b>2.0 – 2.99</b>	<b>Medium</b>
3.0 – 3.99	High
4.0 – 4.9	Very high
$\geq 5$	Extremely high

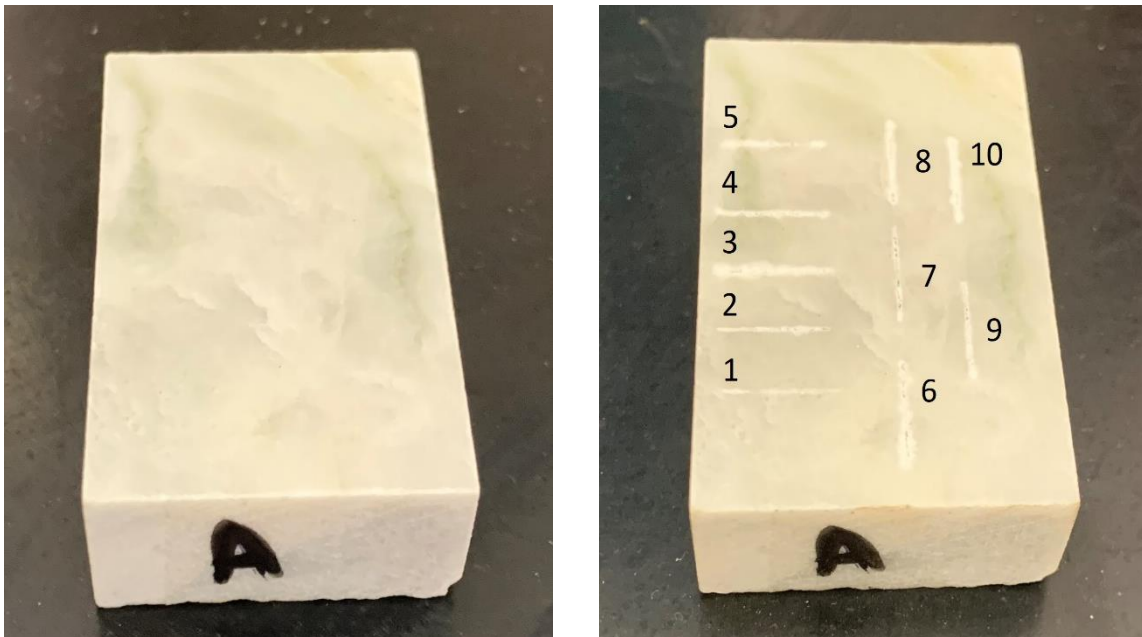


Figure 4.17 - Specimen A before and after the scratches

Table 4.16 - Specimen A, Test 1

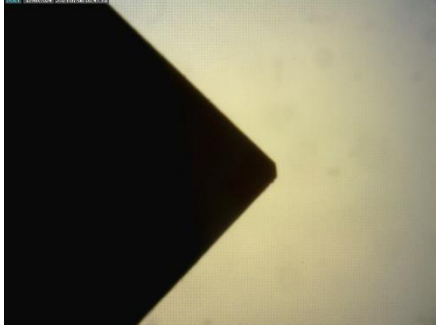

<p>Test 1</p> <p><math>d [0^\circ] = 0.238 \text{ mm}</math> <math>d [90^\circ] = 0.214 \text{ mm}</math></p> <p><math>CAI_{(64.5)} = 2.26</math> <b><math>CAI_{(55)} = 3.03</math></b></p>		
---	---	--

Table 4.17 - Specimen A, Test 2

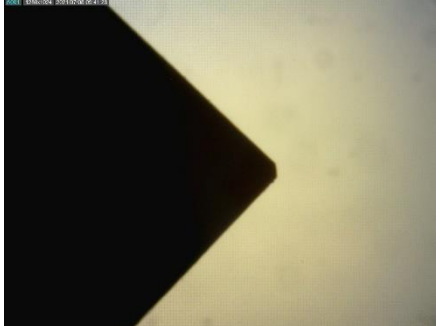

<p>Test 2</p> <p><math>d [0^\circ] = 0.247 \text{ mm}</math> <math>d [90^\circ] = 0.272 \text{ mm}</math></p> <p><math>CAI_{(64.5)} = 2.60</math> <b><math>CAI_{(55)} = 3.48</math></b></p>		
---	--	---

Table 4.18 - Specimen A, Test 3


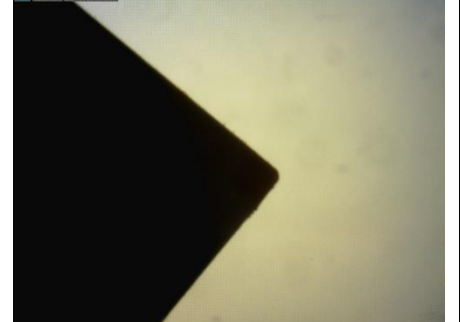
<p>Test 3</p> <p><math>d [0^\circ] = 0.184 \text{ mm}</math> <math>d [90^\circ] = 0.145 \text{ mm}</math></p> <p><math>CAI_{(64.5)} = 1.64</math> <b><math>CAI_{(55)} = 2.20</math></b></p>		
---	---	--

Table 4.19 - Specimen A, Test 4

<p>Test 4</p> <p><math>d [0^\circ] = 0.226 \text{ mm}</math> <math>d [90^\circ] = 0.230 \text{ mm}</math></p> <p><math>CAI_{(64.5)} = 2.28</math> <b><math>CAI_{(55)} = 3.06</math></b></p>		
---	---	--

Table 4.20 - Specimen A, Test 5


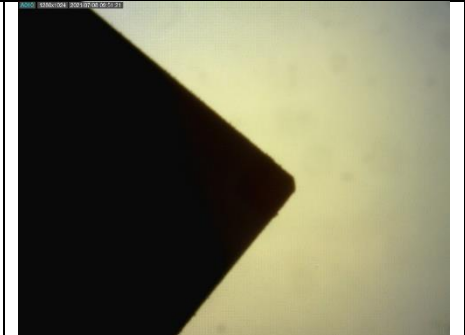
<p>Test 5</p> <p><math>d [0^\circ] = 0.207 \text{ mm}</math> <math>d [90^\circ] = 0.221 \text{ mm}</math></p> <p><math>CAI_{(64.5)} = 2.14</math> <b><math>CAI_{(55)} = 2.87</math></b></p>		
---	---	--

Table 4.21 - Specimen A, Test 6

<p>Test 6</p> <p><math>d [0^\circ] = 0.208 \text{ mm}</math> <math>d [90^\circ] = 0.175 \text{ mm}</math></p> <p><math>CAI_{(64.5)} = 1.91</math> <b><math>CAI_{(55)} = 2.56</math></b></p>		
---	--	---

Table 4.22 - Specimen A, Test 7

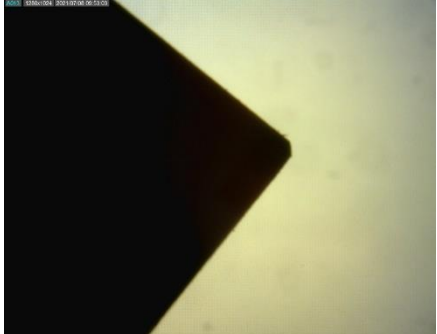

<p>Test 7</p> <p><math>d [0^\circ] = 0.238 \text{ mm}</math> <math>d [90^\circ] = 0.258 \text{ mm}</math></p> <p><math>CAI_{(64.5)} = 2.48</math> <b><math>CAI_{(55)} = 3.32</math></b></p>		
---	---	--

Table 4.23 - Specimen A, Test 8

<p>Test 8</p> <p><math>d [0^\circ] = 0.143 \text{ mm}</math> <math>d [90^\circ] = 0.168 \text{ mm}</math></p> <p><math>CAI_{(64.5)} = 1.55</math> <b><math>CAI_{(55)} = 2.08</math></b></p>		
---	---	--

Table 4.24 - Specimen A, Test 9



<p>Test 9</p> <p><math>d [0^\circ] = 0.217 \text{ mm}</math> <math>d [90^\circ] = 0.222 \text{ mm}</math></p> <p><math>CAI_{(64.5)} = 2.20</math> <b><math>CAI_{(55)} = 2.94</math></b></p>		
---	---	--

Table 4.25 - Specimen A, Test 10

<p>Test 10</p> <p><math>d [0^\circ] = 0.163 \text{ mm}</math> <math>d [90^\circ] = 0.158 \text{ mm}</math></p> <p><math>CAI_{(64.5)} = 1.60</math> <b><math>CAI_{(55)} = 2.15</math></b></p>		
--	--	---

The results about Specimen B are presented below.

Table 4.26 - Specimen B,  $CAI_{(64.5)} [0^\circ]$

Specimen B	Test	d1 [0°]	d2 [0°]	Average CAD unit	Average [mm]	$CAI_{(64.5)}$
	1	2.16	2.16	2.16	0.045	0.45
	2	4.35	4.35	4.35	0.091	0.91
	3	4.80	4.80	4.80	0.101	1.01
	4	2.00	2.00	2.00	0.042	0.42
	5	3.94	3.94	3.94	0.083	0.83
	6	3.38	3.38	3.38	0.071	0.71
	7	3.16	3.16	3.16	0.066	0.66
	8	1.52	1.52	1.52	0.032	0.32
	9	1.85	1.85	1.85	0.039	0.39
	10	1.82	1.82	1.82	0.038	0.38

Table 4.27 - Specimen B,  $CAI_{(64.5)} [90^\circ]$

Specimen B	Test	d1 [90°]	d2 [90°]	Average CAD unit	Average [mm]	$CAI_{(64.5)}$
	1	2.74	2.74	2.74	0.058	0.58
	2	4.51	4.51	4.51	0.095	0.95
	3	5.07	5.07	5.07	0.106	1.06
	4	2.30	2.30	2.30	0.048	0.48
	5	4.20	4.20	4.20	0.088	0.88
	6	3.20	3.20	3.20	0.067	0.67
	7	3.73	3.73	3.73	0.078	0.78
	8	1.48	1.48	1.48	0.031	0.31
	9	1.53	1.53	1.53	0.032	0.32
	10	2.12	2.12	2.12	0.045	0.45

Table 4.28 -  $CAI_{(64.5)}$  average Specimen B

Specimen B	Test	$CAI_{(64.5)}$ Average	Stand. Dev.
	1	0.51	0.09
	2	0.93	0.02
	3	1.04	0.04
	4	0.45	0.04
	5	0.85	0.04
	6	0.69	0.03
	7	0.72	0.08
	8	0.32	0.01
	9	0.35	0.05
	10	0.41	0.04

Table 4.29 -  $CAI_{(55)}$  Specimen B

$CAI_{(55)}$	CAI Classification
0.69	Very low
1.25	Low
1.39	Low
0.60	Very low
1.14	Low
0.93	Very low
0.97	Very low
0.42	Extremely low
0.48	Extremely low
0.55	Very low



Table 4.30 -  $CAI_{(64.5)}$  average Specimen B

$CAI_{(64.5)}$ Average	Stand. Dev.
0.63	0.25

Table 4.31 -  $CAI_{(55)}$  average Specimen B

$CAI_{(55)}$ Average	Stand. Dev.	CAI Classification
0.84	0.34	Very low

Table 4.32 -  $CAI_{(55)}$  classification

$CAI_{(55)}$	Abrasivity scale
< 0.5	Extremely low
<b>0.5 - 0.99</b>	<b>Very low</b>
1.0 - 1.99	Low
2.0 - 2.99	Medium
3.0 - 3.99	High
4.0 - 4.9	Very high
$\geq 5$	Extremely high

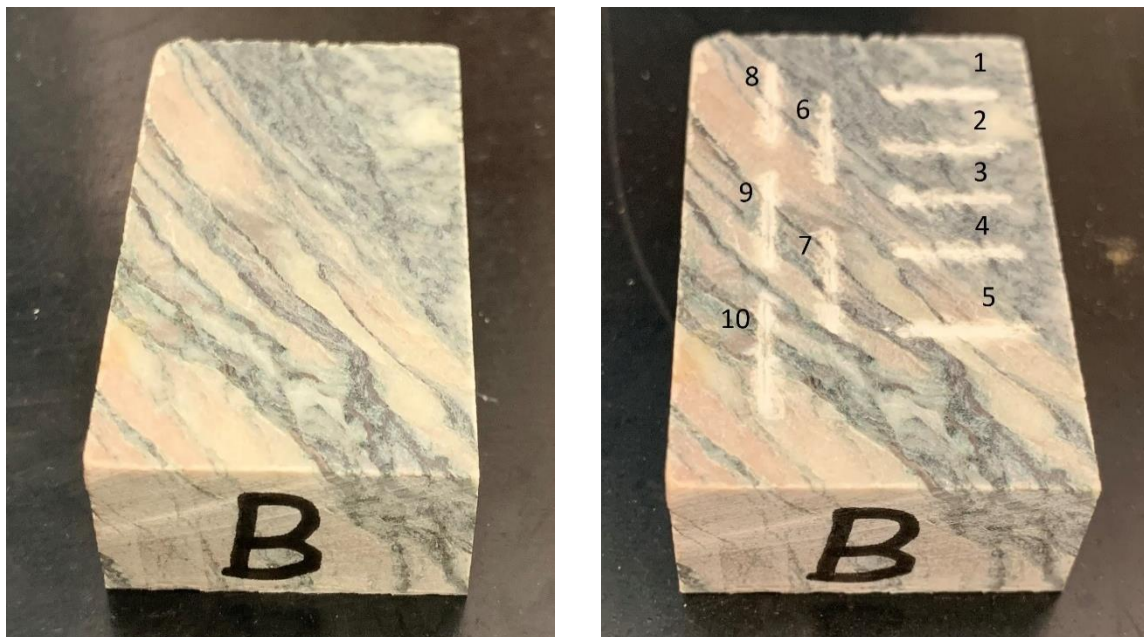


Figure 4.18 - Specimen B before and after the scratches

Table 4.33 - Specimen B, Test 1



<p>Test 1</p> <p><math>d [0^\circ] = 0.045 \text{ mm}</math>  <math>d [90^\circ] = 0.058 \text{ mm}</math></p> <p><math>CAI_{(64.5)} = 0.51</math>  <b><math>CAI_{(55)} = 0.69</math></b></p>		
---	---	--

Table 4.34 - Specimen B, Test 2

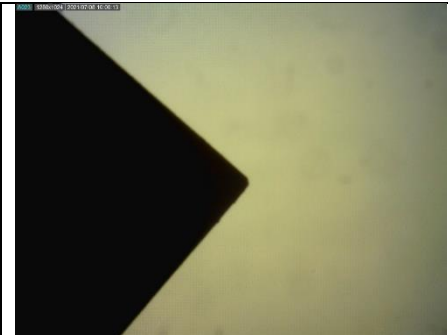
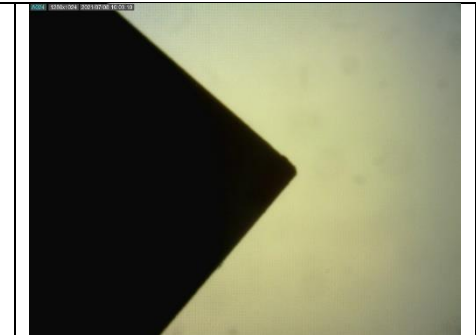
<p>Test 2</p> <p><math>d [0^\circ] = 0.091 \text{ mm}</math>  <math>d [90^\circ] = 0.095 \text{ mm}</math></p> <p><math>CAI_{(64.5)} = 0.93</math>  <b><math>CAI_{(55)} = 1.25</math></b></p>		
---	--	---

Table 4.35 - Specimen B, Test 3



<p>Test 3</p> <p><math>d [0^\circ] = 0.101 \text{ mm}</math>  <math>d [90^\circ] = 0.106 \text{ mm}</math></p> <p><math>CAI_{(64.5)} = 1.04</math>  <b><math>CAI_{(55)} = 1.39</math></b></p>		
---	---	--

Table 4.36 - Specimen B, Test 4

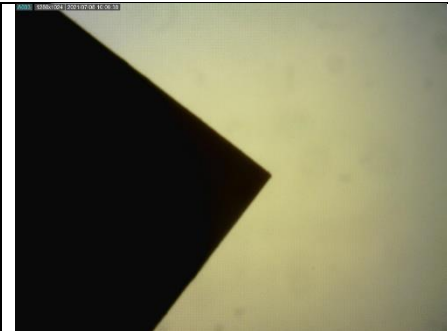
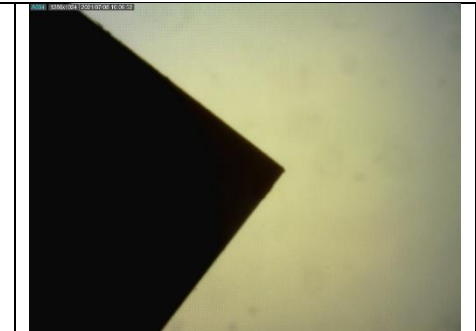
<p>Test 4</p> <p><math>d [0^\circ] = 0.042 \text{ mm}</math>  <math>d [90^\circ] = 0.048 \text{ mm}</math></p> <p><math>CAI_{(64.5)} = 0.45</math>  <b><math>CAI_{(55)} = 0.60</math></b></p>		
---	---	--

Table 4.37 - Specimen B, Test 5


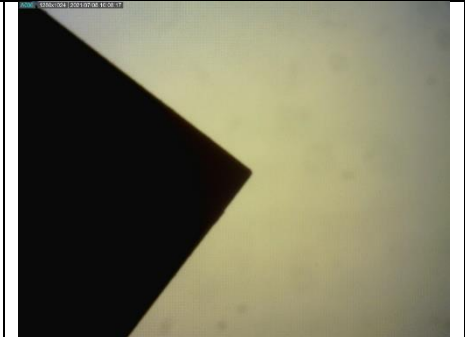
<p>Test 5</p> <p><math>d [0^\circ] = 0.083 \text{ mm}</math> <math>d [90^\circ] = 0.088 \text{ mm}</math></p> <p><math>CAI_{(64.5)} = 0.85</math> <b><math>CAI_{(55)} = 1.14</math></b></p>		
---	---	--

Table 4.38 - Specimen B, Test 6


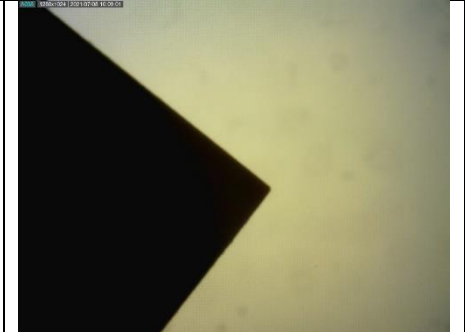
<p>Test 6</p> <p><math>d [0^\circ] = 0.071 \text{ mm}</math> <math>d [90^\circ] = 0.067 \text{ mm}</math></p> <p><math>CAI_{(64.5)} = 0.69</math> <b><math>CAI_{(55)} = 0.93</math></b></p>		
---	--	---

Table 4.39 - Specimen B, Test 7

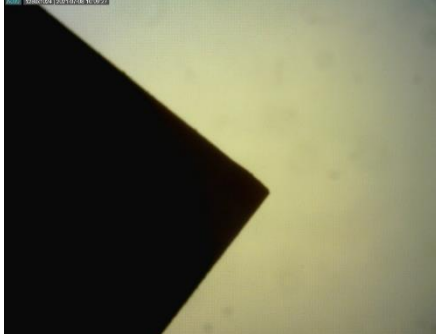

<p>Test 7</p> <p><math>d [0^\circ] = 0.066 \text{ mm}</math> <math>d [90^\circ] = 0.078 \text{ mm}</math></p> <p><math>CAI_{(64.5)} = 0.72</math> <b><math>CAI_{(55)} = 0.97</math></b></p>		
---	---	--

Table 4.40 - Specimen B, Test 8

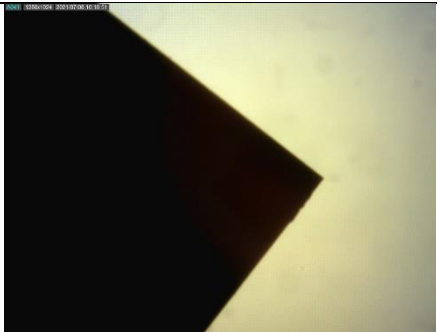
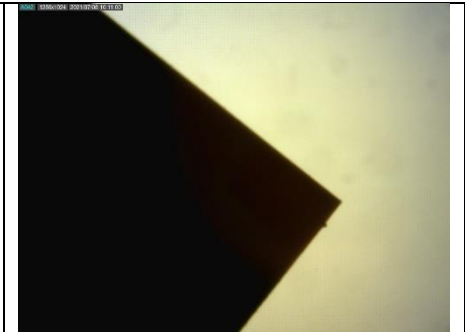
<p>Test 8</p> <p><math>d [0^\circ] = 0.032 \text{ mm}</math> <math>d [90^\circ] = 0.031 \text{ mm}</math></p> <p><math>CAI_{(64.5)} = 0.32</math> <b><math>CAI_{(55)} = 0.42</math></b></p>		
---	---	--

Table 4.41 - Specimen B, Test 9

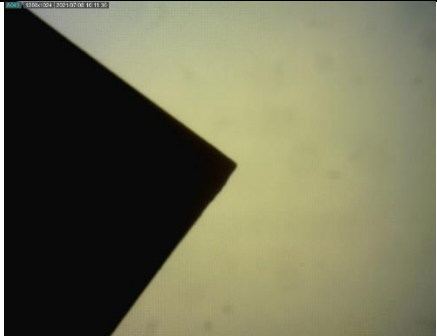

<p>Test 9</p> <p><math>d [0^\circ] = 0.039 \text{ mm}</math>  <math>d [90^\circ] = 0.032 \text{ mm}</math></p> <p><math>CAI_{(64.5)} = 0.35</math>  <b><math>CAI_{(55)} = 0.48</math></b></p>		
---	---	--

Table 4.42 - Specimen B, Test 10

<p>Test 10</p> <p><math>d [0^\circ] = 0.038 \text{ mm}</math>  <math>d [90^\circ] = 0.045 \text{ mm}</math></p> <p><math>CAI_{(64.5)} = 0.41</math>  <b><math>CAI_{(55)} = 0.55</math></b></p>		
--	--	---

For both Specimen A and Specimen B, 10 different determinations were made: as it is possible to see in Figure 4.15 and Figure 4.16, the first 5 test replications were done following a horizontal trajectory, instead, in the other 5 tests the movement of the steel pin was parallel to the long sides of the specimen.

From the results obtained, Specimen A can be classified as a medium abrasive material, on average  $CAI_{(55)}=2.77$ , with an abrasion index higher than that of pure marble, that is  $CAI_{(55)}= 0.60 \div 1.00$  as suggested by the Colorado School of Mines. Specifically, the specimen present area in which  $CAI_{(55)}$  is higher than 3 due to the presence of the selciferous marble, that means highly abrasive material, and areas in which it has medium abrasive characteristics,  $CAI_{(55)}=2.47$  on average.

On the other hand, sample B has a typical behaviour of marble, with a very low abrasion class that corresponds to a slightly abrasive behaviour with a  $CAI_{(55)}= 0.84$ , that is in the middle of the range relative to the marble. However, are noticed in 3 test an index higher than 1, this is justified due to the presence of impurities such as quartz and phyllosilicates.

The results obtained on sample A, therefore, confirm the high abrasiveness found in quarry during the excavation with the chain saw machine.

#### 4.4.DRX analysis

In order to characterize the white-grey marble, with the main goal of knowing the effective percentage of quartz, an X-ray diffraction (XRD) analysis was performed. The XRD is a versatile, non-destructive, and efficient analytical technique that reveals information about materials' crystallographic structure, chemical composition, and physical properties. This technique is based on the observation of the scattered intensity of an X-ray beam, hitting a sample as a function of incident and scattered angle, polarization, and wavelength or energy (Milinovic, 2020). The analysis was carried out at the Politecnico di Torino laboratory, with an XRD - Rigaku SmartLab SE, Figure 4.19. In this device, the sample is fixed, while the tube and the detector move in a circular arc, usually vertically, to measure diffraction intensities for  $2\theta$  values.



Figure 4.19 - XRD - Rigaku SmartLab SE

The Bragg equation,  $n\lambda = 2d\sin\theta$  is one of the keystones in understanding X-ray diffraction. In this equation,  $n$  is the order of diffraction,  $\lambda$  is the characteristic wavelength of the X-rays impinging on the crystallized sample,  $d$  is the interplanar spacing between the rows of atoms, and  $\theta$  is the angle of the X-ray beam with respect to these planes. When this equation is satisfied, X-rays scattered by the atoms in the plane of a periodic structure are in phase, and the diffraction occurs in the direction defined by the angle  $\theta$ .

The samples were previously ground to a fine powder and then analysed in metal slide holders after being uniformly pressed, to assure a perfect distribution of the marble powder. The goal is to obtain a near-infinite number of fine crystallites in random orientations. The  $2\theta$  incidence angles span from  $4^\circ$  (start angle) to  $84^\circ$  (stop angle), with a scan speed of  $0.1^\circ/\text{s}$  thanks to the continuous scan mode. The total runtime for the analysis was 12 min/sample.

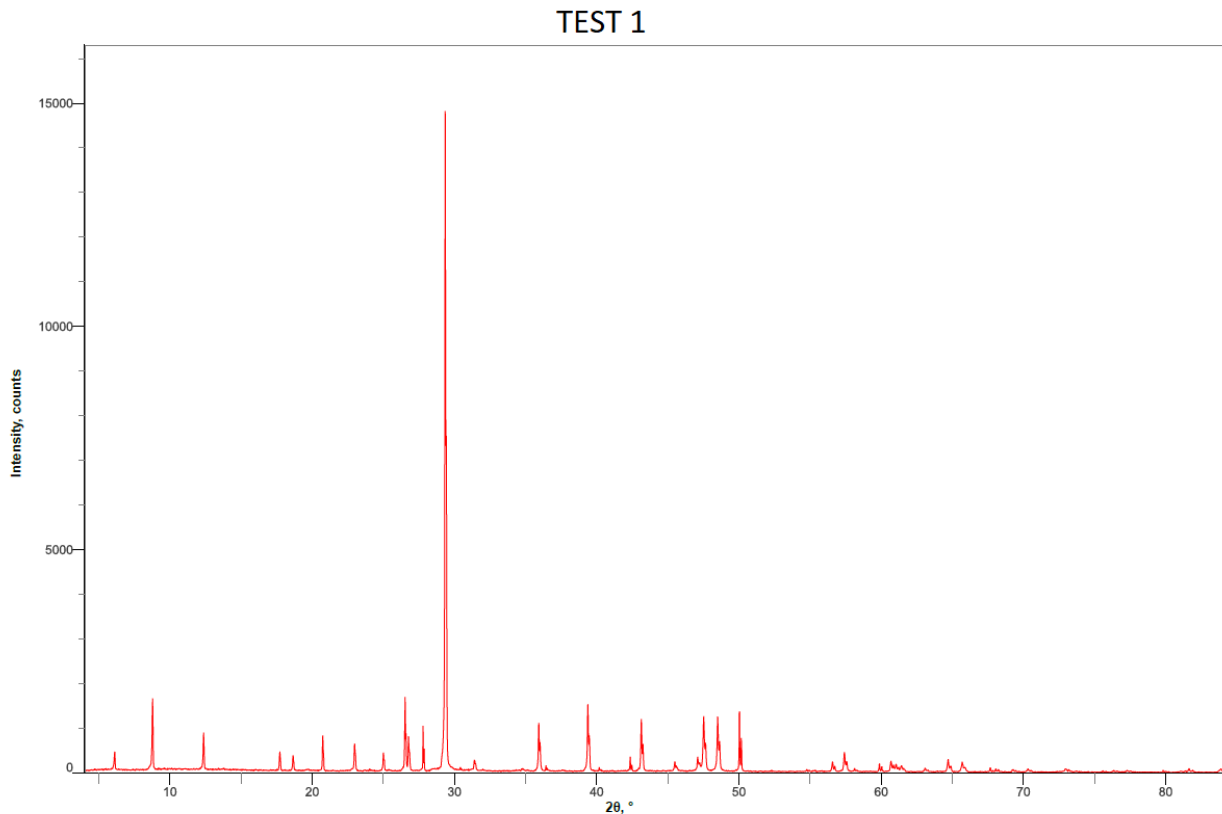
#### 4.4.1. Results

The XRD was used to identify different phases associated with the grey-white marble. The output of the analysis is an intensity versus  $\theta$  angle graph, where the minerals and their abundance can be identified.

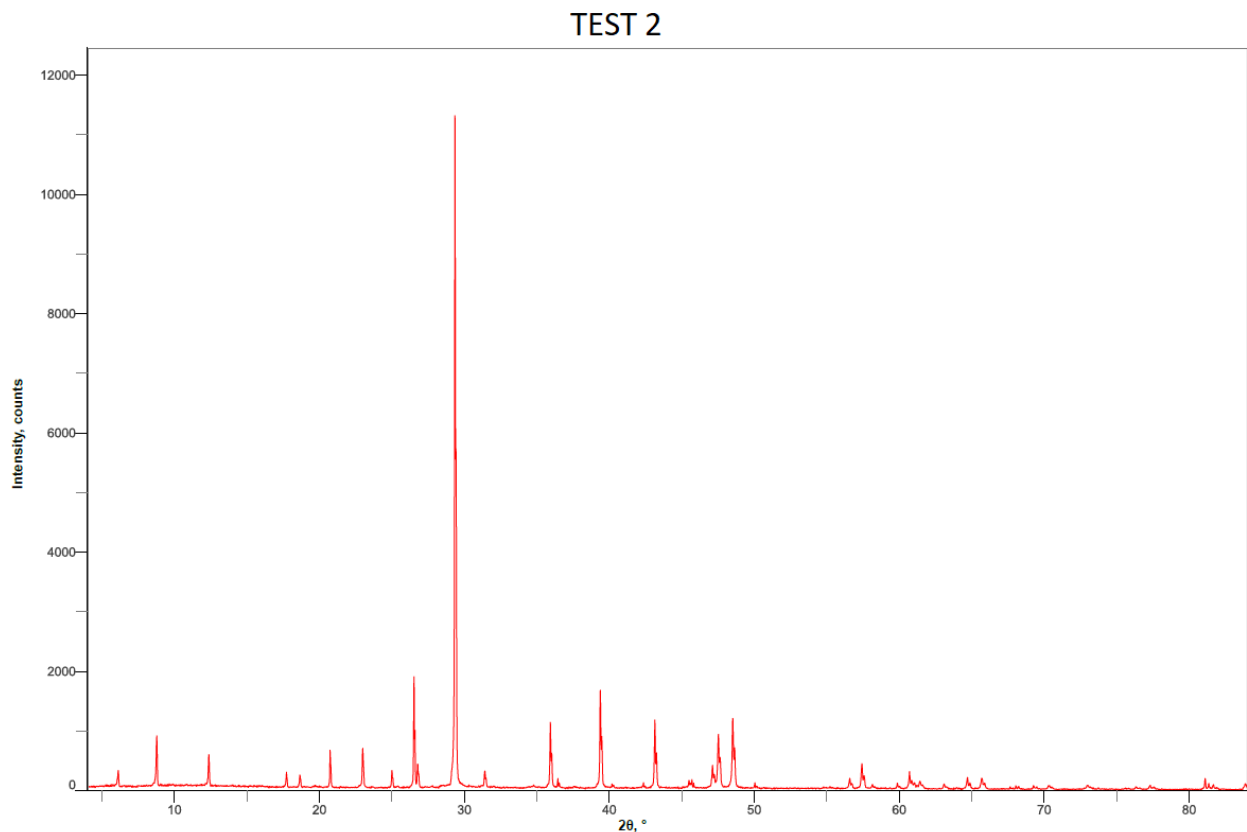
In the graph, the position and the intensity of the peaks are fundamental. The first parameter is indicative of the crystal structure and of the symmetry of the phases; in fact, each mineral is characterized by a given incidence angle. Instead, the intensity of the peaks reflects the total scattering of each plane of the crystal structure, thus returning the abundance of the phases in the analysed sample.

Once the phases have been qualitatively identified, the test proceeds with a quantitative analysis of the individual phases, to reach their abundances in percentage by weight (wt. %) by processing the spectral data using the appropriate Rietveld methodology (Gualtieri et al., 2000). The quantitative analysis of the X-ray diffraction profiles takes place through a complex comparison of the peaks relating to the acquired spectrum and those of the theoretical spectrum, as required by the Rietveld method.

The results of the two tests are given in Figures 4.20 and 4.21.



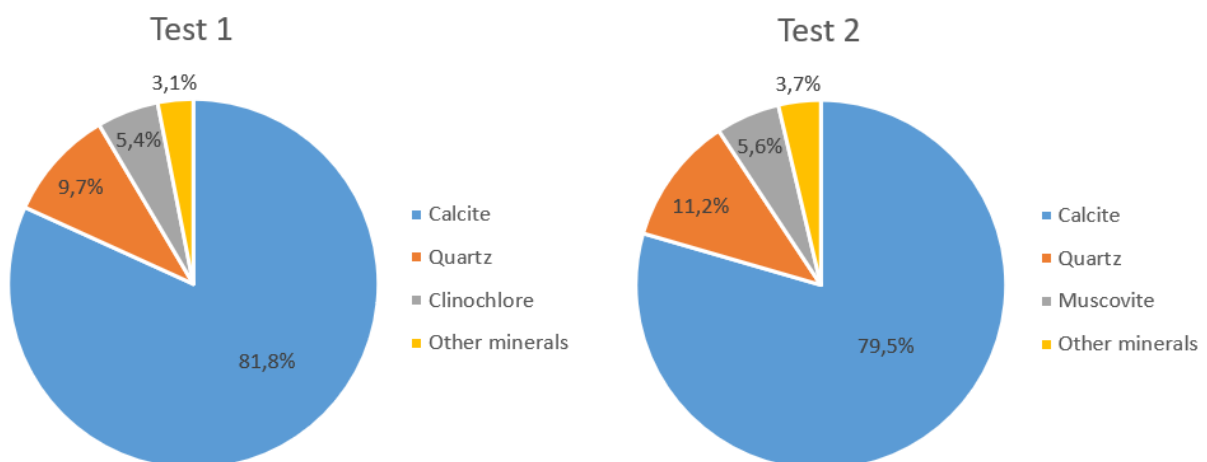
*Figure 4.20 - Test 1 spectral data*



*Figure 4.21 - Test 2 spectral data*

The associated minerals identified in the first test are mainly Calcite, Quartz, and Clinochlore. Instead, in the second test Calcite, Quartz, and Muscovite can be recognized.

The results obtained confirm those achieved from the petrographic analysis; in fact, the material is characterized on average by 80% of Calcite, 10% of Quartz, and the remaining 10% is related to other secondary minerals. Figure 4.22 shows the results of the two analyses.



*Figure 4.22 - Cake graph expressing the results obtained by the test*

## 4.5. Wear test

A test campaign was conducted at the Politecnico di Torino laboratory to study the wear phenomenon using a coarse marble sand coming from the Penna dei Corvi quarry. The test was performed on the white-grey marble, as it is the material that causes problems with the advancement in the underground exploitation.

The wear test device allows the evaluation of wear phenomenon and its reduction with soil conditioning (Barbero et al., 2012). The wear test determines the weight loss of a metal disk rotating around its axis at a constant speed of 180 rpm inside a cylindrical container filled with the granular material for a total time of 8'53". During the test, the torque provided by an electrical motor, required for the rotation of the disc, is recorded (Oñate Salazar et al., 2016).

Test campaigns have been carried out using aluminium discs characterized by Vickers hardness values of 116 MPa. A normal confinement pressure of about 2 kPa is applied to ensure continuous contact between the disc and the ground. At the end of the test, the wear of the disc can be quantified by evaluating the weight loss due to the friction with the soil and thus correlating this value to the average torque applied during the execution of the test. Figures 4.23 and 4.24 show the scheme of the test.

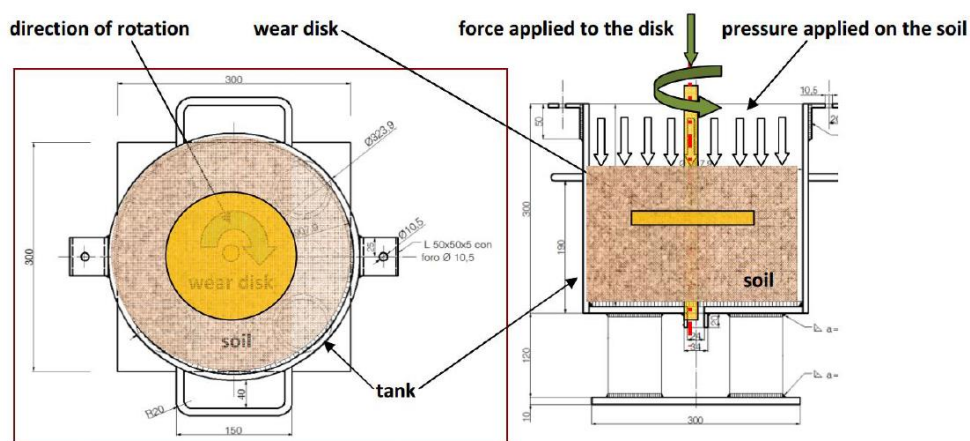


Figure 4.23 - Scheme of the test (Oñate Salazar et al., 2018)



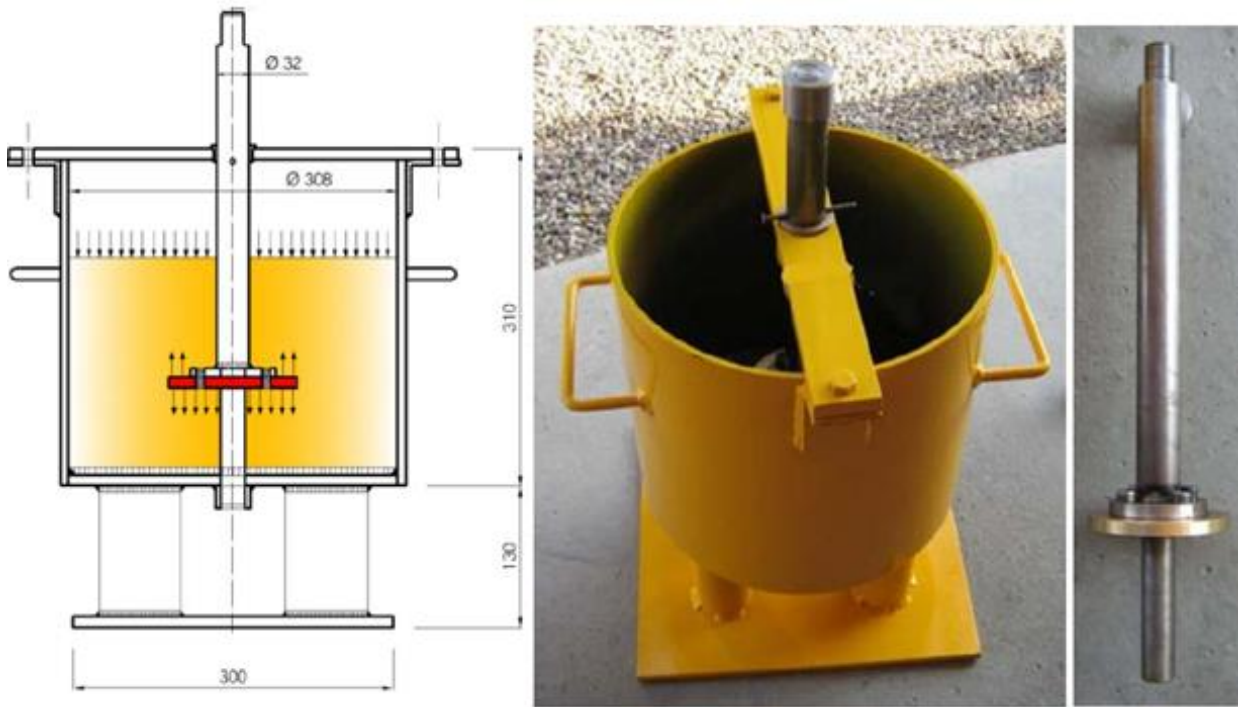


Figure 4.24 - Cross section and pictures of the test device (Oñate Salazar et al., 2018)

The developed wear test procedure can be summarized in the following steps:

- Sample preparation: 20-25 kg of granular soil are mixed with water, foam, and/or eventually with other chemical additives depending on the set of conditioning to be tested
- Weighing of the disc: calculation of  $w_1$ , which is the initial weight of the disc
- Assembly of the disc on a drive shaft: the shaft is inserted assembled with the disc inside the tank, and the removable bushing is locked on the tank by mean of two bolts
- Filling of the first layer of material: the tank is filled from the bottom up to the height of the disc, to ensure a correct contact between the soil particles and the lower surface of the disc
- Completion of filling of the chamber: the whole sample is placed inside the tank, and the confinement pressure of 2 kPa is applied
- Start of the test with real-time torque measurement
- Disc weighing: measure of  $w_2$  (final weight) and calculation of the weight loss ( $\Delta w$ ).

The material to be tested was previously crushed, to guarantee dimensions of the fragments lower than 20 mm and, in order to determine the grain size distribution curve, it was first separated by a splitter so that a representative material sample could be analysed. A picture showing a representative sample of the material is given in Figure 4.25.



*Figure 4.25 - Representative sample of the material*

The grain size curve of the soil allows to derive the grain size distribution and to determine the suitable conditioner to be used during the tests.

In order to avoid sampling problems and differences between the tests carried out, the whole material was sieved by choosing square mesh sieves to know the percentages of the different fractions on the total sample and the results are proposed in Table 4.43; the corresponding granulometric curve is shown in Figure 4.26.

Table 4.43 - Grain size distribution of the sample analyzed

Opening diameter [mm]	Soil retained [g]	Soil passing [g]	Percent passing [%]
31.5	0.00	7431.10	100.00
16.0	14.70	7416.40	99.80
8.0	2606.70	4809.70	64.72
6.3	938.80	3870.90	52.09
4.0	1070.90	2800.00	37.68
2.0	835.90	1964.10	26.43
1.0	466.00	1498.10	20.16
0.5	236.20	1261.90	16.98
0.250	141.10	1120.80	15.08
0.125	112.50	1008.30	13.57
0.075	115.80	892.50	12.01
Pan	892.50	0.00	0.00
Total weight	7431.10		

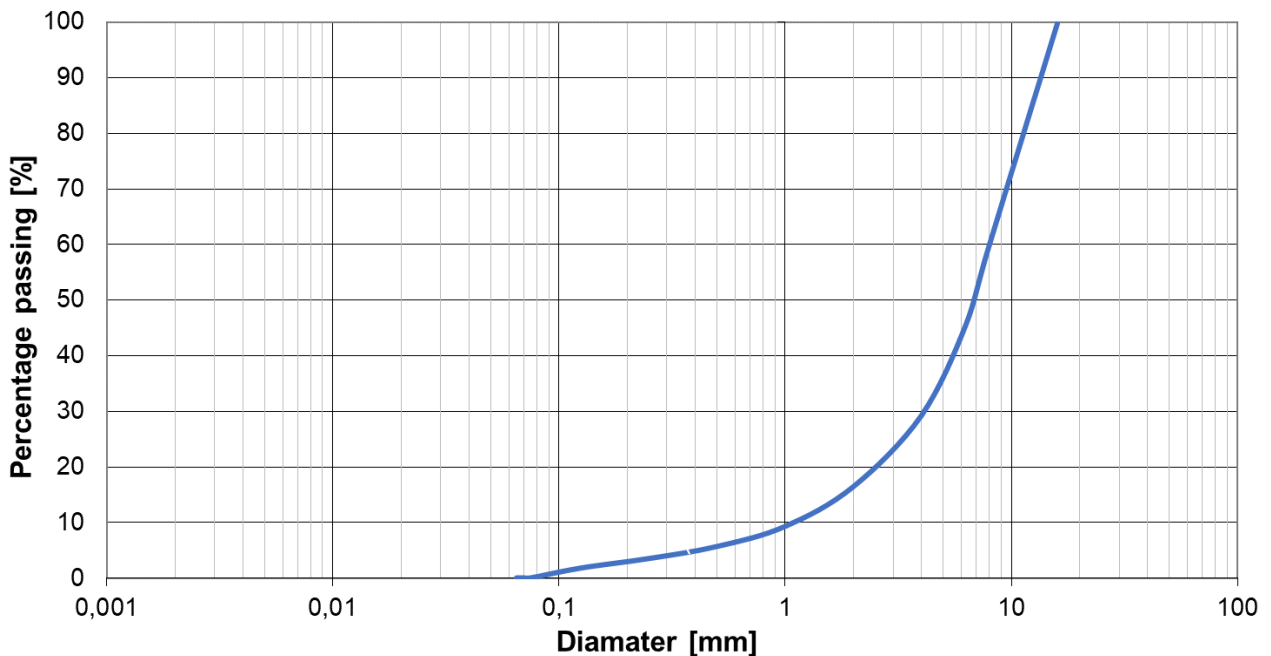


Figure 4.26 - Granulometric curve of the crushed marble

In order to evaluate the maximum amount of water that the marble can absorb, with the aim to design an optimal configuration in terms of percentage of water content for each test, a sample of 500g representative of the whole crushed marble was taken. 5g of water were added to the material, from time to time, until the saturation condition was reached. After each addition, the material was mixed to achieve its homogenization and allow it to absorb water. Once 35 g of water were supplied, equal to 7% by weight, the marble was saturated, and it no longer absorbed water.

As a first step, the wear phenomenon was studied by using aluminium discs in rotation inside the marble conditioned with different percentages of water; the range was between 1% and 9%. Outcomes of the test campaign are shown in Figure 4.27: the curve obtained is then called “wear bell curve”.

In the second phase of the study, the percentage of water corresponding to 4% (the medium value of the investigated ones) and 9% (the highest analysed water content) have been considered in order to test two different chemical agents: un high-performance liquid foaming agent (Product A) and a natural polymer in powder (Product B). These products have been developed expressly with the goal of wear reduction.

#### 4.5.1. Conditioning with water

For each of the chosen percentages of water content, three tests were performed, and the data associated with the test were calculated as the average of the three lost weight values of the disc. The results of all the tests performed are given below; for each test, the average torque value and the average weight loss of the disc were determined.

The results obtained in this first campaign are shown below: Tables 4.44 - 4.49 summarize the results achieved from each test by varying the percentage of water content; Figures 4.27 shows the trend related to the weight lost as a function of the water content, and these results are compared with the data, taken from the study of Oñate Salazar et al. (2018), obtained from an experimental test carried out on quartzite soil.

*Table 4.44 - Test with 1% of water content in weight*

Test n.	Water content [%]	Weight lost [g]	Medium torque [Nm]	Average $\Delta w$ [g]	Average torque [Nm]
1	1	0.08	0.691	0.083	0.631
2	1	0.07	0.500		
3	1	0.10	0.704		

*Table 4.45 - Test with 2% of water content in weight*

Test n.	Water content [%]	Weight lost [g]	Medium torque [Nm]	Average $\Delta w$ [g]	Average torque [Nm]
1	2	0.28	0.974	0.260	0.987
2	2	0.24	0.996		
3	2	0.26	0.990		

Table 4.46 - Test with 3% of water content in weight

Test n.	Water content [%]	Weight lost [g]	Medium torque [Nm]	Average $\Delta w$ [g]	Average torque [Nm]
1	3	0.47	1.404	0.447	1.219
2	3	0.38	1.099		
3	3	0.49	1.154		

Table 4.47 - Test with 5% of water content in weight

Test n.	Water content [%]	Weight lost [g]	Medium torque [Nm]	Average $\Delta w$ [g]	Average torque [Nm]
1	5	0.65	0.960	0.607	1.004
2	5	0.70	1.137		
3	5	0.47	0.714		

Table 4.48 - Test with 7% of water content in weight

Test n.	Water content [%]	Weight lost [g]	Medium torque [Nm]	Average $\Delta w$ [g]	Average torque [Nm]
1	7	0.75	1.055	0.560	0.863
2	7	0.52	0.731		
3	7	0.42	0.803		

Table 4.49 - Test with 9% of water content in weight

Test n.	Water content [%]	Weight lost [g]	Medium torque [Nm]	Average $\Delta w$ [g]	Average torque [Nm]
1	9	0.57	0.304	0.493	0.478
2	9	0.45	0.750		
3	9	0.42	0.380		

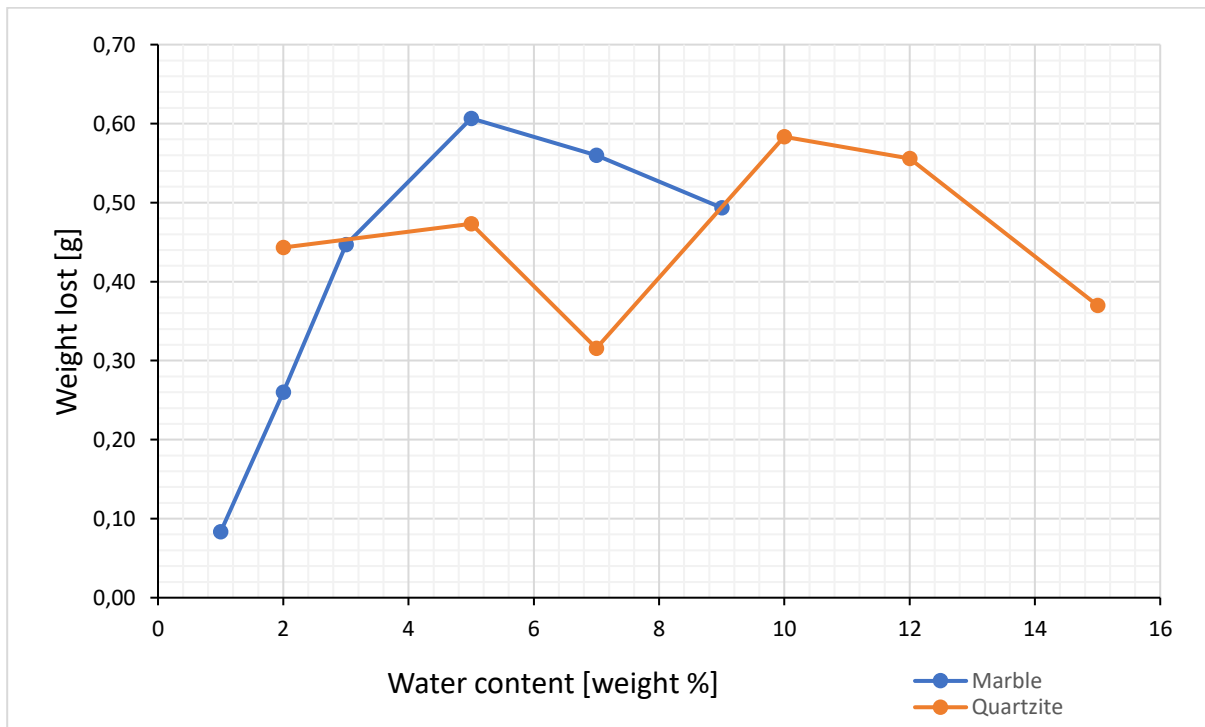


Figure 4.27 – Weight lost – Water content graph: wear bell curve

As shown in Figure 4.27, the trend of the weight lost associated with the marble has a bell shape, with a peak in correspondence with the 5% of water content. It is clear from the results obtained that the water content deeply affects the weight loss of the test discs. Starting from a percentage of humidity in the soil equal to the natural condition, the increase in water does not to have a beneficial effect until reaching a percentage of 5%. In fact, for this value, the curve shows a peak, after which a further increase in the water content results in a sharp decrease in the weight loss of the test tool itself.

As it can be seen in the graph, despite the quartzite has, naturally, a higher percentage of quartz with respect to those of the marble studied (98% versus 10% on average), the two trends follow a wear bell curve reaching more or less the same peak, even if the peak of the quartzite is obtained for higher percentages of water.

This phenomenon occurs because even if the rock appears homogeneous on the visual scale, it is inhomogeneous on the microscopic scale, as it is made up of different minerals or of the same mineral but with different crystallographic orientations from point to point, and therefore it is inhomogeneous in terms of mechanical strength, that is, if subjected to load in different points, it reacts differently: the same load can cause local failure when it is applied in one point, and be well supported when it is applied in another point. Small-scale inhomogeneity can create problems when it is necessary to calculate the force that a tool must apply to cut the marble or to predict the service life of the tool itself: it does not act on an average material, but subsequently acts on small volumes of individual components; if it finds a mineral that is too hard, it jams or becomes damaged, and it is not comforting for it to know that, statistically, it would later find a much less strong mineral that would have readjusted the average; therefore, for this reason, even if the percentage of quartz is lower, the marble shows a trend comparable to quartzite.

However, this study is beneficial on a real scale. Simply by injecting water into the marble to be cut, if the natural moisture in the ground is around the maximum value of the wear bell curve, it is possible to move away from this peak and avoid premature wear of the tools.

#### 4.5.2. Conditioning with chemical agents

In the second step of the study, in agreement with the manufacturer of the chemical agents, it was decided to perform both the tests with the 4% in water content. It corresponds to an average water content value (compared to the studied wear bell curve) and represents a non-advantageous condition in terms of disc wear.

For the liquid foaming agent (Product A), it was decided to condition the granular material by adding a solution consisting of 96 parts of water and 4 parts of the chemical compound, and, after a manual homogenization, the quantity of solution corresponding to the percentage to be analysed was taken.

Regarding the natural polymer in powder (Product B), a slurry at 1% by weight was produced, i.e., 1 g of polymer per 100 g of water. The additive was activated through a mixing process in water for 5', performed with a cement mixer. Once the appropriate water had been prepared, the correct amount of Product B was added within the first minute of mixing.

The results obtained in this first campaign are shown below: Tables 4.50 and Table 4.51 summarize the results achieved from each test; Figures 4.28 shows the trend related to the weight lost as a function of the water content, including the wear bell curve before evaluated.

*Table 4.50 – Product A, test with 4% of solution content in weight*

Test n.	Water content [%]	Weight lost [g]	Medium torque [Nm]	Average $\Delta w$ [g]	Average torque [Nm]
1	4	0.62	1.360	0.62	1.360

*Table 4.51 - Product B, test with 4% of solution content in weight*

Test n.	Water content [%]	Weight lost [g]	Medium torque [Nm]	Average $\Delta w$ [g]	Average torque [Nm]
2	4	0.61	1.745	0.61	1.745

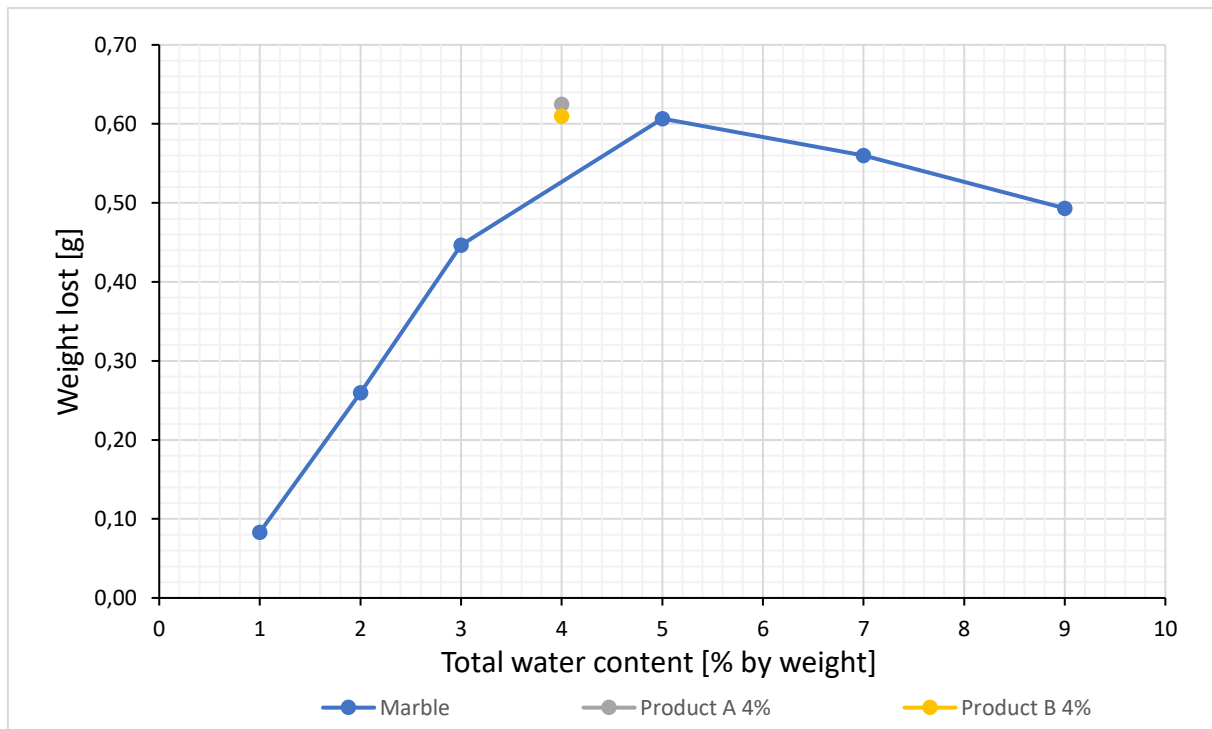


Figure 4.28 - Weight lost – Water content graph: wear bell curve and conditioned test

The results achieved shows that: the tests carried out with the solution content equal to 4% did not show a reduction in terms of weight lost by the disc compared to the water conditioned material. For this reason, it was therefore decided to increase the dosage of the conditioning solution by evaluating the efficiency of Product B, as the technical data sheets show a lower environmental impact and a shorter biodegradation time.

The results achieved with this configuration are proposed in Table 4.52 and in Figure 4.29.

Table 4.52 - Product B, test with 9% of solution content in weight

Test n.	Water content [%]	Weight lost [g]	Medium torque [Nm]	Average $\Delta w$ [g]	Average torque [Nm]
3	9	0.25	1.044	0.25	1.044



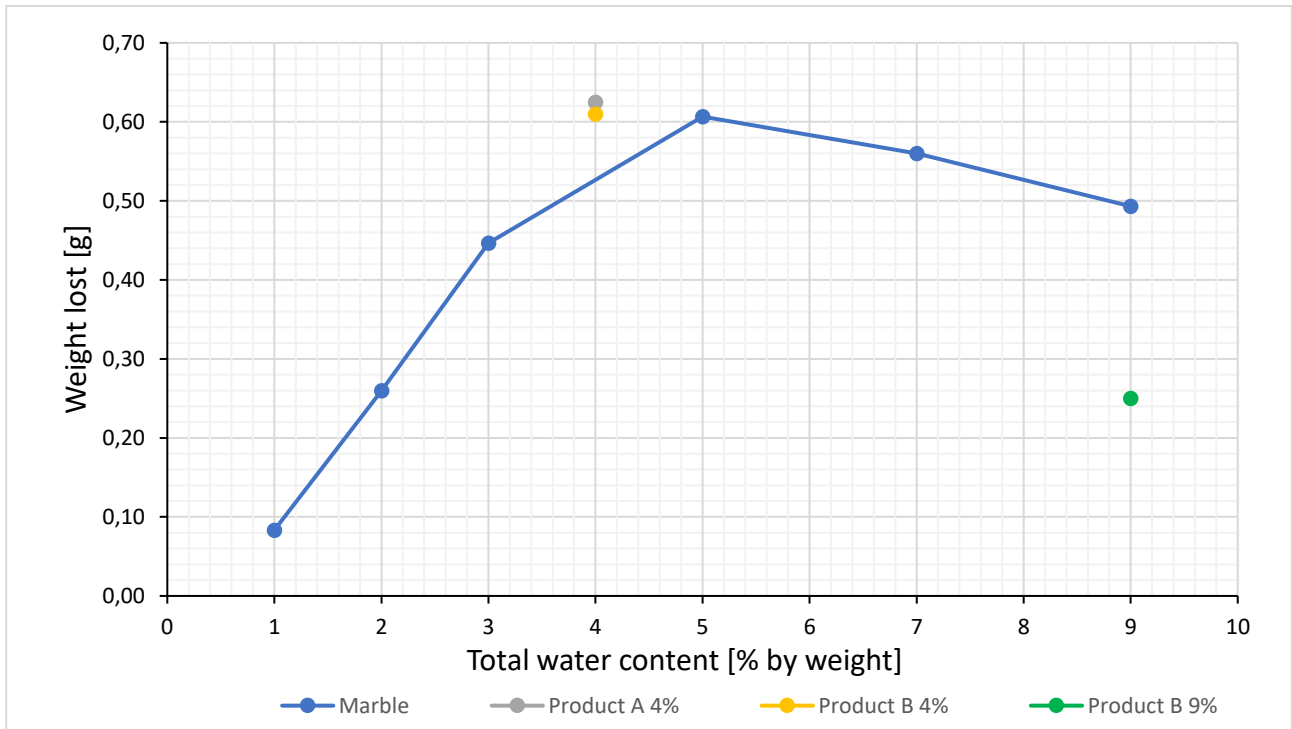


Figure 4.29 - Weight lost – Water content graph: Conditioning test

For the second water content, 9%, the results showed a 50% reduction of the weight lost by the disc compared to those achieved with the water conditioned material.

The operation of the Product A is not excluded a priori. Based on the experience of the Tunnelling & Underground Space Research Center, some foaming agents express their aptitude to reduce wear when the adequate water content, softness, and homogeneity of the granular material are satisfied. Consequently, for both chemical agents, exist a critical minimum water content, keeping the quantity of conditioning agents constant, below which no reduction of the disc wear can be observed.

## 5. Conclusion

This thesis aimed to investigate the performance of a chain saw cutting machine used to exploit the marble at the Penna dei Corvi quarry. Due to the inability of the chain saw cutting machine to advance in the exploitation of a portion of the quarry, it was decided to carry out various laboratory tests in order to characterize the marble in terms of hardness and abrasiveness. At the current state of work, the quarry managers have decided to stop the works regarding the tunnel entrance for the underground exploitation and to move it about sixteen m away, due to the presence of quartz nodules, in order to avoid it. As for the open-pit mining activity, the works follow the approved project, albeit with some difficulty because, as assessed in the tests carried out, inclusions of quartz, feldspar, and other impurities involve a premature wear of the cutting tools.

The results obtained from the petrographic analysis of the thin sections show the presence of quartz veins in the carbonate matrix, which become more evident and predominant, in percentage, in the material extracted from the underground exploitation. This consideration is also validated by the micro-hardness analysis: in fact, the marble shows high Vickers values; on the contrary, the values found in the Cipollino marble are comparable with the typical ranges of marble, albeit with some harder areas caused by the presence of impurities. Also, in relation to this reason, as for the CAI classification, white marble can be classified as a medium abrasive material, with an abrasion index higher than the other marble. Specifically, this marble contains high percentages of siliceous components, which are rich in quartz.

For this reason, wear tests accompanied by an XRD analysis were carried out only for the grey-white marble; this latter analysis was fundamental for obtaining the mineralogical composition of the material, and its results shows that the marble is composed by more or less 80% of calcite, 10% of quartz and 10% by other minerals. Regarding the wear test, the obtained results highlight that the peak value, correspondent to 0,607g loss by the disc, is obtained for a water content of 5% and have confirmed what it was assumed; in fact, the material is very abrasive and shows the same trend obtained by the study of Oñate Salazar et al. (Oñate Salazar et al., 2016), on a material with more than 98% quartz and, although the percentage of quartz is drastically lower, the useful life of the tool is drastically reduced due to its interaction with the quartz. The results obtained can be justified as the tool acts on very small volumes of individual components, and therefore, when

it finds the quartz, it can jam or damage, and it is not comforting for it to know that after a few instants it would have found, along its path, a softer mineral, such as calcite.

The wear test in conditioning granular material with foaming agents or aggregating polymers shows that Product B reduces by 50% the amount of weight lost by the disc in conditions in which the material is conditioned with a quantity of solution equal to 9%. Instead, there is no reduction of the analysed parameter for the tests with a solution percentage equal to 4%.

Overall, it is clear that the preliminary study of the wear phenomena related to the link between the type of rock, water content, pressure applied, conditioning and cutting tools is fundamental for optimizing the economic and productive resources of the mining site.

In conclusion, the results obtained with Product B provide a preliminary contribution as a possible and feasible strategy for extracting marble from the underground quarry; however, an on-site test campaign can certainly confirm the results' goodness; considering that the scale factor, the cut execution mode, and the composition of the disk are different to those analysed in the laboratory.

For this reason, this study will undoubtedly be the subject of future investigations.

## Bibliography

Alber M., Yarali O., Dahl F., Bruland A., Kasling H., Michalakopoulos T.N., Cardu M., Hagan P., Aydin H., 2013. ISRM suggested method for determining the abrasivity of rock by the CERCHAR abrasivity test. *Rock Mech Rock Eng.* 47: 261-266

Akaishi M., Ohsawa T., Yamaoka S., 1991. *Synthesis of Fine-Grained Polycrystalline Diamond Compact and Its Microstructure*

Ashby N. A., 1951. The factor of hardness in metals, in *New Zealand Engineering*

Barbero M., Peila D., Picchio A., Chierigato A., Bozza F., Mignelli C., 2012. Procedura sperimentale per la valutazione dell'effetto del condizionamento del terreno sull'abrasione degli utensili nello scavo con EPB. *GEAM*, Anno XLIX, n.1, aprile, pp 13-19

Bieniawski Z.T., 1989. *Engineering rock mass classifications: a complete manual for engineers and geologists in mining, civil, and petroleum engineering.* Wiley, New York, p. 250-253

Centro di GeoTecnologie (CGT), 2007. *Carta giacimentologica dei marmi delle Alpi Apuane a scala 1:10.000 e sua informatizzazione*

Cerchar—Centre d'Études et des Recherches des Charbonnages de France, 1986. *The Cerchar abrasivity index.* Verneuil

Forfori B., 2020. *Relazione tecnica integrativa regione Toscana - L.R. n°35/2015 e DPGR n°72/R/2015 Art. 2. (Personal translation)*

Germak A., Herrmann K., Dai G., Li Z., 2006. *Development of calibration methods for hardness indenters*

Gualtieri A., 2000. *Accuracy of XRPD QPA using the combined Rietveld-RIR method*

Hamzaban M. T., Memarian H., Rostami J., 2018. Determination of scratching energy index for Cerchar abrasion test. *Journal of Mining & Environment*, Vol. 9, p. 73-89

Hoek E., Kaiser P.K., Bawden W.F., 1995. *Support of Underground Excavation in Hard Rock*

Hoek E. & Brown E.T., 1997. Practical estimates of rock mass strength. *International Journal of Rock Mechanics and Mining Sciences*, vol. 34, p. 1165–1186

Hoek E., Marinos P., 2000. GSI: A Geologically Friendly Tool for Rock Mass Strength Estimation Proc. GeoEng2000 Conference, Melbourne. p. 1422-1442

Jacobs N., Hagan P., 2009. The effect of stylus hardness and some test parameters on the Cerchar Abrasivity Index

Kaklis K., Agioutantis Z., Alevizos G., Maurigiannakis S., 2007. Microhardness testing of marbles and correlation with mechanical properties. 8<sup>th</sup> HSTAM International Congress on Mechanics, Patras

Mancini R., Cardu M., 2001. Ingegneria degli Scavi. Politeko Ed., Torino, Italy

Milinic J., Alveirinho Dias A., Janeiro A.I., Pereira M.F.C., Martins S., 2020. XRD Identification of Ore Minerals during Cruises: Refinement of Extraction Procedure with Sodium Acetate Buffer

Mordor Intelligence, 2021. Marble Market - Growth, Trends, COVID-19 Impact, and Forecasts

Mott B. W., 1956. Micro-Indentation Hardness Testing, Butterworths Scientific Publications

Nishimatsu Y., (1972). The mechanics of rock cutting. International Journal of Rock Mechanics and Mining Science & Geomechanics. Abstract: 9(2), 261–270

Oñate Salazar C.G., Martinelli D., Todaro C., Peila D., Boscaro A., 2016. Preliminary study of wear induced by granular soil on metallic parts of EPB tunnelling machines

Oñate Salazar C.G., Martinelli D., Todaro C., Peila D., Boscaro A., 2018. Study of Wear in Conditioned Granular Soil by Using a New Test Device. In Tunnelling and Underground Space Technology

Palmström A., 1974. Characterization of jointing density and the quality of rock masses

Palmström A., 1995. A rock mass characterization system for rock engineering purposes, p. 400-401

Rostami J., Ozdemir L., Bruland A. and Dahl F., 2005. Review of Issues Related to Cerchar Abrasivity Testing and Their Implications on Geotechnical Investigations and Cutter Cost Estimates

Rostami J., Ghasemi A., Gharahbagh E. A., Dogruoz C., Dahl F., 2013. Study of Dominant Factors Affecting Cerchar Abrasivity Index

Schede Rete Natura 2000, 2017. Sito di importanza regionale SIR-pSIC 17 “Monte Sumbra”, Atti legislativi di riferimento per l’istituzione e la perimetrazione: Del CR 06/0

Smallman R.E. & Ngan A.H.W., 2014. Characterization and Analysis, in Modern Physical Metallurgy

Smith R.L. & Sandland G.E., 1922. An Accurate Method of Determining the Hardness of Metals, with Particular Reference to Those of a High Degree of Hardness, Proceedings of the Institution of Mechanical Engineers, Vol. I, p. 623–641

West G., 1989. Rock abrasiveness testing for tunnelling. International journal of rock mechanics and mining sciences, Vol. 26, p. 151–160